universität wien

MASTERARBEIT / MASTER'S THESIS

Titel der Masterarbeit / Title of the Master's Thesis

„Examination of two calorimeter prototypes: liquid scintillator with wavelength shifted fiber readout and plastic scintillator lead modules“

verfasst von / submitted by

Patrick Riegler BSc

angestrebter akademischer Grad / in partial fulfilment of the requirements for the degree of

Master of Science (MSc)

Wien, 2022 / Vienna, 2022

Studienkennzahl lt. Studienblatt / degree programme code as it appears on the student record sheet:	A 066 876
Studienrichtung lt. Studienblatt / degree programme as it appears on the student record sheet:	Master Physik
Betreut von / Supervisor:	Priv. -Doz. Johann Zmeskal

Contents

Abstract

This thesis is dedicated to the description and testing of two different calorimeter types:
Prototype 1, a large-area detector with liquid scintillator EJ-309 (based on xylene) on the one hand, and Prototype 2, a more compact detector with plastic scintillators on the other.
Their purpose is to detect the energy deposition of charged and neutral particles propagating through the setup. In this process, the energy deposited at a time, t, is first converted into scintillation light and later into a characteristic electrical signal with well-defined amplitude.
Prototype 2 allows, in addition to energy measurement, the determination of the trajectory of individual particles with a resolution of 16 x 16 mm^2 (given by the pixel size).

While Prototype 1 will be used to study kaonic clusters and kaon scattering experiments at J-PARC [12], Prototype 2 will serve the detection of Pontecorvo annihilations (annihilation processes with more than 1 interacting nucleon).
Specifically, the rate of $\bar{p}3N$ Pontecorvo annihilation: $\bar{p}^3He \rightarrow np$ will be determined and compared with the 'rescattering' approach from the particle model or, at the quark level, with the Fireball model (quark annihilation and quark rearrangement as approaches). Thereby, the Fireball model predicts a rate of $\approx 10^{-6}$ and the Rescattering approach predicts a rate of $\approx 10^{-8} - 10^{-7}$. [9]

Detector tests performed with Prototype 1 include among others the recording of cosmic ray amplitude spectra, delay measurements between different signals as well as tests concerning detector efficiency and position dependence. For Prototype 2, on the other hand, the amplitude spectrum and the Time-Over-Threshold spectrum for cosmics were determined. These measurements are preceded by preparatory measurements with plastic scintillators (e.g. efficiency measurements, energy calibrations, voltage characteristic measurements).

Zusammenfassung

Diese Arbeit widmet sich der Beschreibung und Testung zweier verschiedener Kalorimeter Prototypen: Prototyp 1, einem großflächigen Detektor mit Flüssigszintillator EJ-309 (auf Xylol Basis) einerseits und Prototyp 2, einem kompakteren Detektor mit Plastikszintillatoren andererseits.
Ihr Zweck ist die Erfassung der Energieabgabe von geladenen und neutralen Teilchen, die durch den Aufbau propagieren. Dabei wird die zu einem Zeitpunkt, t, deponierte Energie zunächst in Szintillationslicht und später in ein charakteristisches, elektrisches Signal mit wohldefinierter Amplitude umgewandelt. Prototyp 2 ermöglicht zusätzlich zur Energie-Messung auch die Bestimmung der Trajektorie einzelner Teilchen mit einer Auflösung von 16 x 16 mm^2 (gegeben durch die Pixelgröße).

Während Prototyp 1 für die Untersuchung kaonischer Cluster und von Kaon-Streuexperimenten am J-PARC eingesetzt werden soll [12], so soll Prototyp 2 für die Detektierung von Pontecorvo Annihilationen (Annihilationsprozesse mit mehr als 1 interagierenden Nukleon) verwendet werden. Konkret soll die Rate der $\bar{p}3N$ Pontecorvo Annihilation: $\bar{p}^3He \rightarrow np$ bestimmt und mit dem 'Rescattering' Ansatz aus dem Teilchenmodell bzw. auf Quarkebene mit dem Fireball-Modell (Quark Annihilation und Quark Rearrangement als Ansätze) verglichen werden. Dabei sagt das Fireball-Modell eine Rate von $\approx 10^{-6}$ und der Rescattering Ansatz eine Rate von $\approx 10^{-8} - 10^{-7}$ voraus. [9]

Die mit Prototyp 1 durchgeführten Detektortests umfassen u.a. die Aufnahme der Amplituden-Spektren von kosmischer Strahlung ('Cosmics'), Tests zur Effizienz und Positionsabhängigkeit der Detektoren und die zeitlichen Verzögerungen ('Delays') zwischen verschiedenen Signalen. Parallel dazu wurde für Prototyp 2 das Amplitudenspektrum und das Time-Over-Threshold Spektrum für Cosmics bestimmt. Diesen Messungen gehen Vorbereitungsmessungen mit Plastikszintillatoren (z.B. Effizienz-Messungen, Energie-Kalibrierungen, Kennlinien-Messungen) voraus.

1 Introduction

2 Theoretical backgrounds/ Experimental basics

2.1 relevant signal types

In this very first chapter, we will recall relevant information about the signal terminology used in this thesis. This implies the clarification of the terms: analogue signal, digital signal, differential signal and single-ended signal.
Pulse signals and signals in general, carry information in two forms: analogue or digital.
An analogue signal codes continuously-valued information by varying one or more of its characteristics, (e.g. amplitude and/or shape), in some fixed relation to the information value. [14]
For the conducted experiments, the information of interest (e.g. the energy of a charged particle deposited in the detector) is mainly carried in the amplitude, which is proportional to the desired quantity.
In contrast to the continuum of amplitudes or shapes which are possible for the analogue pulse, the digital or logic signal can in practise only take on 2 discrete states - digital '0' and digital '1'.
In our case, a digital signal takes state '1' if the corresponding analogue signal is above a certain threshold. The digital signal then takes a certain, fixed voltage pulse height.
If it is below this threshold, it is in state '0' and thus takes the voltage value 0 V. This digital threshold, however, mustn't be thought of as a definite voltage value but as a narrow band of voltages due to the difficulties to create a signal with exact voltage level. [14]

Beside the type of information transfer, we also need to specify the potential levels to which the signal refers.
A differential signal is floating, meaning that it has no reference to ground. The measurement is taken as the voltage difference between the two wires that transmit it. The main advantage of differential signals is that it minimizes the influence of noise on the measurement, since the noise is added to both wires and can then be filtered out by taking the difference. [2]
On the other hand, a single-ended measurement is taken as the voltage difference between a wire and ground. Unlike for the differential signal, the noise is only on the positive wire and thus reflects in the data. However single-ended results are easier to handle as differential signals and can furthermore be displayed on the oscilloscope. [2]
In order to profit from all advantages, we often measure and amplify differential signals and later convert them to single-ended signals via a differential signal converter.

Devices that process ingoing electronic signals can be allocated to standardized modular systems.
The by far most relevant representative of such a modular system (at least in this thesis) is the NIM (Nuclear Instrument Module) standard which demands certain mechanical and electronic specifications. For example, it governs the size and voltage supply of modules (e.g. converters, discriminators, logic units, shaping amplifiers) and shape of connectors as well as their logic levels.

The NIM logic is based on the current ranges defined in the following table:

	output must deliver	input must accept
Logic 0	-1 mA to +1 mA	-4 mA to +20 mA
Logic 1	-14 mA to -18 mA	-12 mA to -36 mA

Table 1: current-based definition of NIM logic levels

Technical limitations do not permit that digital thresholds are realized as a definite voltage value.
Instead they are implemented as a narrow band of voltages defined in table 1.
Since the input and output impedances of all NIM modules are required to 50 Ω, the logic voltage levels are thus 0 V (for logical '0') and -0.8 V (for logical '1'). [14]
For sake of completion, we mention that there exist also two other logic families that are widely used in nuclear and particle physics electronics: TTL (Transistor-Transistor Logic) or ECL (Emitter-Coupled

logic). These have different ranges for the logical values but we omit to indicate them because we restricted to the use of NIM signals in this thesis.

2.2 structure of SiPMs

Silicon Photomultipliers (SiPMs) are semi-conductor devices that enable the detection of very small doses of light (up to several photons) by conversion to a characteristic voltage signal.
Basically, they consist of lots of p^+ipn^+ diodes operated in Geiger-Mode (operated in reverse bias and above the breakdown voltage), called Single Photon Avalanche Diodes (SPADs). [13]

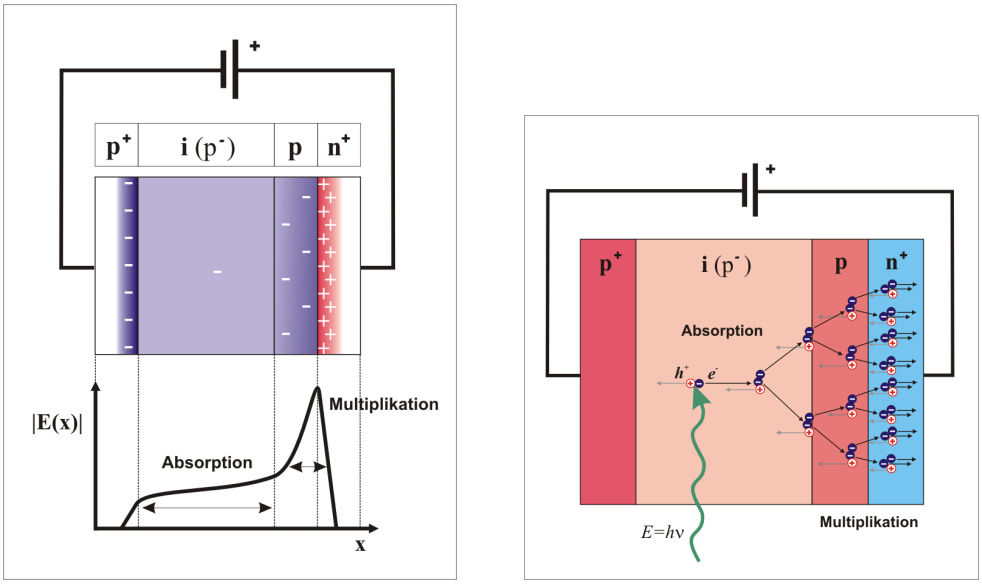

(a) electric field inside an APD and distribution of ions in the semi-conductor lattice if bias voltage is applied.

(b) avalanche effect: e^- created by the inner photoelectric effect performs impact ionizations multiple times generating a great amount of free charges.

Figure 1: structure and working principle of an APD; source: [3]

In principle, those SPADs are similar to Avalanche Photodiodes (APDs), which work in the following way (see figure 1): the Geiger Mode operation leads to a considerable electric field inside the diode (between the p-layer and the n^+-layer to be precise) since the naturally adjusting depletion region in the pn^+ junction gets broadened by the external applied voltage.
Incoming light produces electron-hole pairs in the i-layer via the inner photoelectric effect.
Consequently to their creation, they will be separated: while the holes drift to the p^+ layer to the left and recombine there, the electrons propagate to the right, where the electric field in the pn^+ junction acts on the electrons with an attractive force.
As a result, the thereby accelerated electrons gain enough kinetic energy to generate new electron-hole pairs by impact ionization.
After the impact ionization, the consecutive processes - acceleration and pair production - repeat again and again but with all available charges, leading to an tremendous increase of charge carriers (avalanche effect).
The region, where this takes place is thus called multiplication zone. [13]

A typical gain achieved by the APDs is between 100 and 500, but for SPADs we have a common gain, M, in the order of several millions.
The reason for this is that unlike for the APDs, the electric field inside the SPADs is high enough such that both, electrons and holes, contribute to the avalanche generation via impact ionization.
As a consequence, the SPADs yield an uncontrolled, self-sustaining multiplication process (breakdown) and a large current flow (in order of some μA).
As the breakthrough of the diode has happened, it becomes conductive and a high current flow sets in. However this makes the SPAD insensitive to further incoming photons, so a sustainable, high current

must be prevented.
The time limitation of the breakthrough is achieved by inserting a high ohmic resistor (in the order of a few 100 kΩ) in series.[1]
The voltage decline caused by the resistor then decreases the reverse biased voltage below the breakthrough voltage such that the SPAD returns into its non-conductive state.
So the actual SiPM consists of hundreds of SPADs linked together, where each SPAD has its own resistor operated in series (see figure 2). [13]

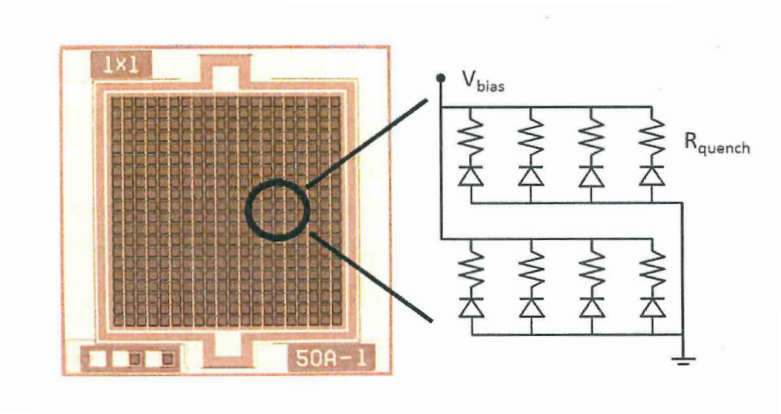

Figure 2: top view (left) and schematic (right) of a SiPM from KETEK with 1 x 1 mm^2 sensitive area and 50 x 50 μm^2 pixel size, thus 20 x 20 pixels connected in parallel. Each pixel works as an individual SPAD with a quenching resistor R_{quench} in series.; source: [13]

2.3 characteristic signal

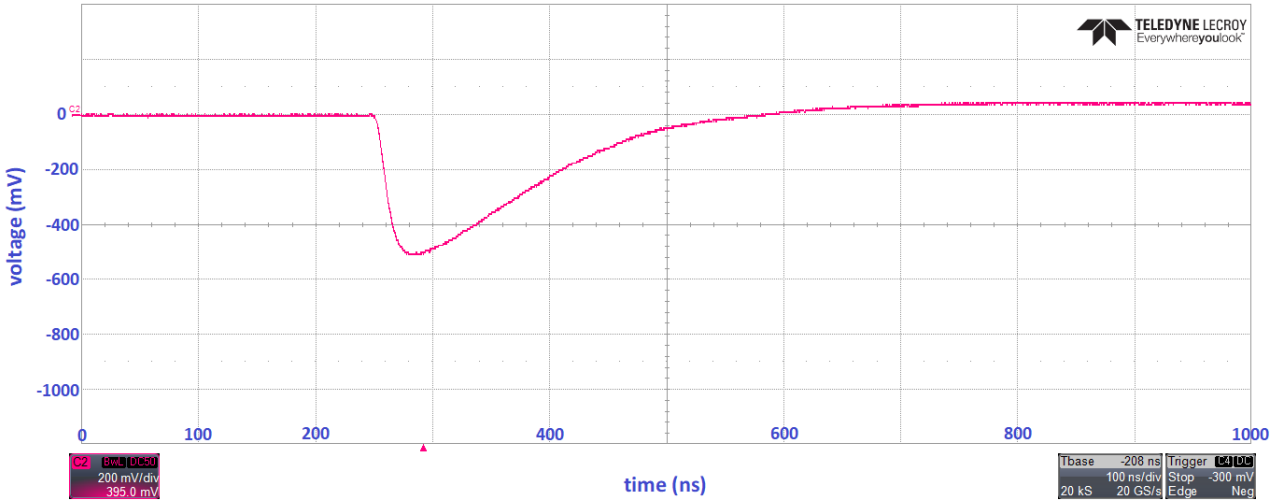

Figure 3: scintillation light created in a plastic scintillator is converted to a characteristic signal via a SiPM + amplifier

In figure 3, a typical voltage signal from a SiPM is presented: at first the SPADs do not conduct because there are no free charge carriers in the depletion region.
From this follows that there is a high reverse voltage between the poles and that there is no voltage decline at the oscilloscope.
The creation of electron-hole pairs in the i-layer through scintillation light and the previously mentioned avalanche effect yield a high number of charge carriers leading to the breakdown of the SPAD and thus to a current flow.
Therefore the voltage decline over the oscilloscope grows up to a culmination point, whereby its height (with respect to the no voltage decline line at the beginning) is called the amplitude of the signal.
Since the resistor of the oscilloscope and the series resistor of the SPAD form a voltage divider, the

[1] for the SiPM this needs to be done for each SPAD!

voltage decline at the oscilloscope decreases beyond the culmination point while the voltage decline at the series resistor grows accordingly.
This trend continues up till the SPAD returns into the reverse blocking state we had in the beginning.
Back in the initial state, the whole process repeats again when the next photon hits the SPAD.
Using an appropriate voltage-energy calibration, one can then associate the measured amplitudes with the energy deposited in the detector.

2.4 gain

Up to now, we have touched the term 'gain' rather superficial.
Although we only observe the total gain of the signal in experiments, it is nevertheless instructive to know that it depends on three parameters. The first is named 'internal gain' (at least in this thesis) and describes the arising differences in gain due to differences in the production of the SiPMs.
In fact, experiments show that two production-equal SiPMs do not always yield the exact same amplitudes although the other two parameters are adjusted equally.

Another parameter is the gain due to the adjusted (reverse) bias voltage, which is applied over the respective SiPM. There will be more details of this so-called 'bias-driven gain' in the next chapter. At this point, we only remark that increasing the reverse bias leads to a rising (bias-driven) gain of the SiPM.

Usually the amplification of the first two parameters does not suffice to obtain a clearly visible signal; it needs to be amplified additionally by an amplifier board.
So the third and last parameter is the amplification due to the amplifier board, which has a fixed gain but it might (also) vary slightly from board channel to board channel.
It will be denoted as 'board gain' since its amplification factor, V, is determined by the components in the electric circuit of the board channel.
Together, these three parameters account for the total gain of the signal.

Talking about signal amplification, it must be mentioned at this point that for some measurements involving Prototype 2, another amplifying component, a so-called shaping amplifier (or spectroscopy amplifier) was used. We will not provide further explanations here, but its purpose and working principle are described in great detail in the section 'shaping amplifier and ADC'.

2.5 trigger and thresholds

In order to restrict the event recording to values of interest, we can impose a trigger condition on an input signal. It then becomes a so-called triggering signal. The value of the trigger level then governs if measurements are recorded or not: if the triggering signal exceeds the trigger level, it is recorded as well as all other adjusted, simultaneously measured values, else there is no recording.

There exist two important kinds of trigger conditions: the oscilloscope trigger condition that is used for triggering analogue signals and the discriminator condition that works with a governing NIM signal created from an analogue signal. The oscilloscope trigger condition demands a minimum signal amplitude, the so-called trigger threshold.
It can be adjusted directly on the oscilloscope as well as the edge on which we want the condition to be examined.
The signals we deal with are negative valued since we choose the positive pole as GND.
Thus we always trigger on the falling/negative edge since it comes first.

The discriminator condition is based on a NIM signal generated by a NIM logic by comparison of the current signal value and the discriminator threshold. In this thesis, this threshold and the threshold of the oscilloscope trigger condition often coexist but the former governs the measurement.[2]
Note, that we deal in this thesis with special NIM logics, producing special digital signals. These are sometimes referred to as Time-Over-Threshold (ToT) signals to better distinguish them from general

[2] this holds unless the discriminator threshold is smaller than the threshold of the oscilloscope trigger condition. In that special case, no measurements are taken.

discriminator signals. A general discriminator signal starts with a jump from the logical '0'-state to the logical '1'-state, when the signal entering the NIM logic exceeds the set threshold value. While a general discriminator signal ends with a jump from '1' to '0' after a fixed, predefined time span (implying fixed signal width), the ToT signals have varying width.
For better imagination, the analogue and digital signal from the same input source were laid over each other in figure 4.

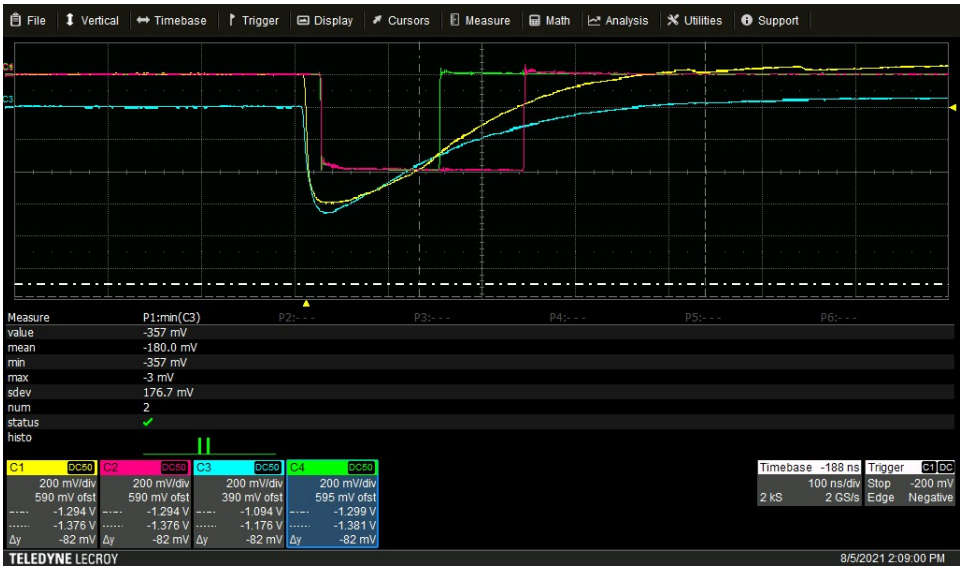

Figure 4: analogue and digital signal overlap

As the analogue signal exceeds the discriminator threshold, a jump from the logical state '0' to the logical state '1' happens and as the analogue signal falls below the discriminator threshold, it falls back from state '1' to '0'. These logical states correspond to characteristic voltage decays predefined by the signal type.
For the experiments of this paper, the digital signals used were mainly NIM signals that assign to the logical state '0' a voltage equivalent to 0 V and to the logical state '1' a voltage equivalent to -800 mV as already mentioned in chapter 'relevant signal types'.

The currently adjusted discriminator threshold can be determined if we display the analogue signal and the digital signal of the corresponding SiPM on the oscilloscope. For that purpose, the digital signal is chosen as triggering signal and we change to 'Persistence mode' in order to keep all signals that occurred since the last refresh on screen.
As the depicted events accumulate, the most analogue signals will intersect at a certain point forming a node (see in figure 5). The height of this node with respect to the 0 V voltage decay level serves as approximated value for the adjusted threshold. Delays between the start of the digital signal and the described node are caused by processing time of electronic devices as well as different cable lengths.
The adjustment of discriminator threshold settings depends on the used amplifier board (see chapter 'amplifier boards').

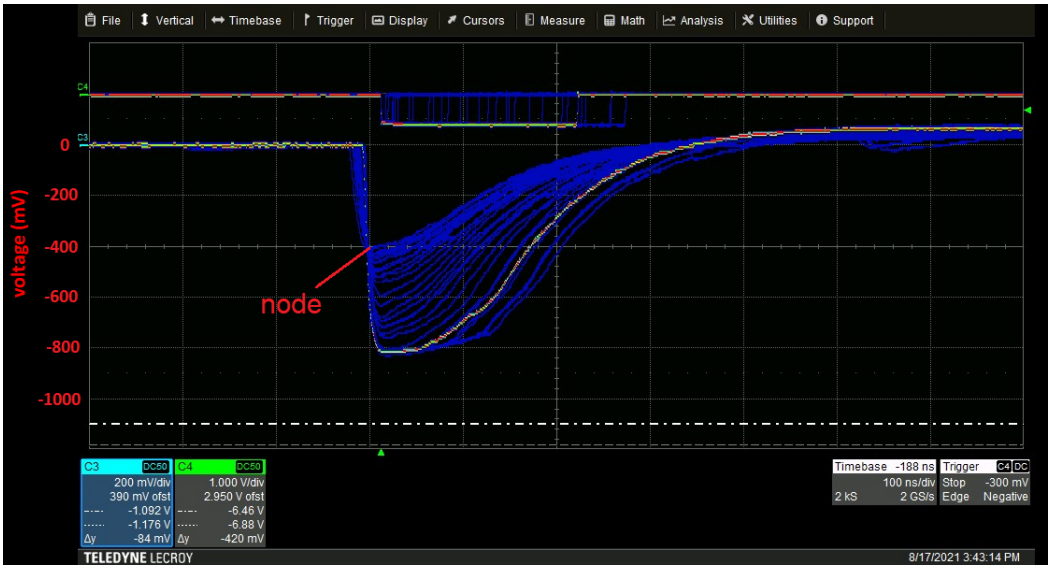

Figure 5: oscilloscope screenshot: the discriminator threshold of a digital signal (CH4) is adjusted. Notice that the corresponding analogue signals of several events layed over each other (CH3), generate a node. This node is approximately 2 boxes below the 0 V voltage line of CH3, thus the discriminator threshold is set to -2 x 200 mV= -400 mV.

Quite often, we use AND signals of two digital signals to make sure that both signals are above a predefined threshold. This makes sure that events with lower amplitudes are excluded from the recorded data sample.
While the digital signal associated with an analogue signal is uniquely defined by a single parameter, the threshold level, the situation is different for AND signals. In this case, instead of a single threshold level, TH3, the threshold levels, TH1 and TH2, of the two underlying digital signals are required.

Keep in mind, that factors such as different cable lengths and electronic processing (especially for AND signals) can lead to a delay of the NIM signal. When it comes to comparisons of trigger thresholds and of signal amplitudes among themselves, we will set up the convention that the we compare the absolute values of them.

2.6 delays and hysteresis

When we talk about the delay between two signals, we mean the time elapsed between two signal levels. In this thesis, the delay measurements on the oscilloscope are conducted via the measurement routine dt@lv(x,y) where x and y are the input sources. The oscilloscope itself associates to x and y the corresponding oscilloscope channels at which these signals enter the oscilloscope. We, on the other hand, will provide the corresponding SiPM names as the parameters x and y in order to simplify the experimental description and discussion.
You may want to think about this routine as an oscilloscope function which outputs values based on the measurement parameters predefined by the user. Beside the 2 inputs, x and y, for which we desire to know the delay, we must specify for both, a level value in percent of the measured amplitude.
So let's say SiPM x outputs a signal with amplitude, A_x, and SiPM y outputs a signal with amplitude, A_y, as a result of a detected particle. Then choosing e.g. a level of 20% for SiPM x and a level of 30% for SiPM y results in measuring the time elapsed between the $0.2 \cdot A_x$ value of x and the $0.3 \cdot A_y$ value of y.

Noise at the trigger point, i.e. above the actual signal, can severely affect delay measurements to the point of unusability. In this case, the oscilloscope interprets the noise on the real signal as additional signals with edges with respect to which it takes additional delay records.
In this way additional unwanted delay values get into the measurement set.
To minimize these effects of noise on the trigger point, one uses the hysteresis control.
Via the Hysteresis setting, one imposes a limit above and below the signal level, which excludes measurements of noise or other perturbations within this band.
The width of this hysteresis band is specified in milli-divisions with 500 mdiv being the default value.

[4]

In any case, the hysteresis must be larger than the maximum noise spike one wants to ignore.
In practice, the default value is a good starting point unless the signals are very noisy. [4]

3 Experimental backgrounds

Two detector setups Prototype 1 and Prototype 2 are tested. They shall detect not only charged particles, but also neutral particles (photons, neutrons etc.) and give information about the amount of energy that was deposited by the transmitting particle.

3.1 description of plastic scintillator detectors

The simplest detector type we worked with is the plastic scintillator detector, which consists in our case of two main components: a plastic scintillator and a SiPM.
For several preparing plastic scintillator experiments as well as Prototype 2 experiments, there is a cuboid plastic scintillator with 2 SiPMs glued to its short side faces respectively.
One has to notice that this detector, however, is read out from two sides and thus gives two signals.
Their measurements must be correlated because they share the same scintillator, which is useful for measuring the particle's trajectory.
Throughout the thesis, we made the convention that we address each detector signal by the name we give its SiPM.
For reasons of reflection reduction to the outside and surface protection, the plastic scintillator is often wrapped in teflon tape.
The SiPMs were attached to the scintillator with optical glue, but for short checks of the SiPMs, teflon tape served as fast alternative to fix the relative position of the SiPM to the scintillator.
The prior application of optical grease to the SiPM reduced scattering effects and total reflections during these checks.

A depiction of such a plastic scintillator detector can be seen in figure 6a, 6b and figure 7.

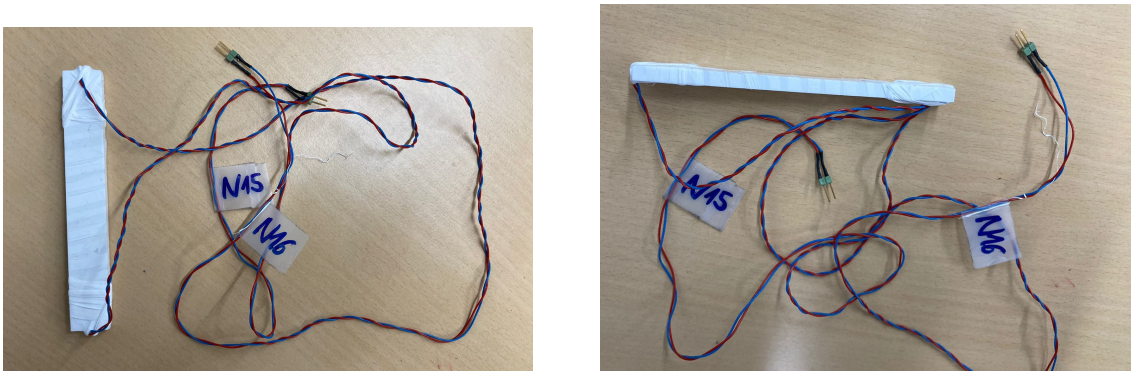

(a) top view of a plastic scintillator detector (b) sideview of a plastic scintillator detector

Figure 6: a typical plastic scintillator detector wrapped in teflon, with 2 SiPMs as readouts. The dimensions of the plastic scintillator from the detector shown here are 110 mm x 16 mm x 5 mm.

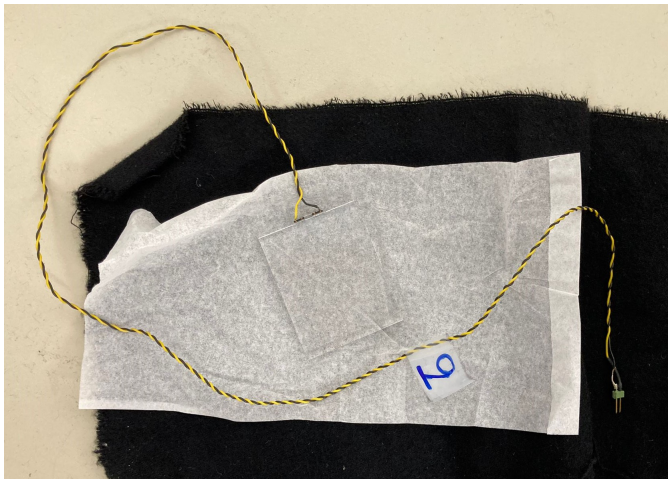

Figure 7: Plastic scintillator detector without teflon wrapping, with 1 readout consisting of two SiPMs connected in series

3.2 description of Prototype 1

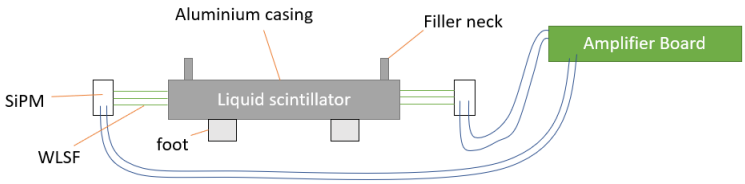

(a) scheme of the Prototype 1 detector connected to the amplifier board

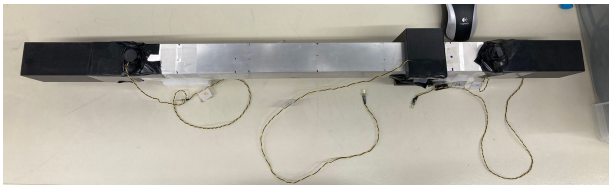

(b) top view of Prototype 1 detector

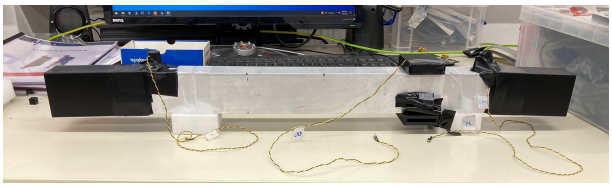

(c) sideview of Prototype 1 detector

Figure 8: Prototype 1 with black caps on the edges
Figure 8b and 8c show the Prototype 1 detector with a black slider attached to it (close to the right black cap). This slider was only used throughout a certain series of measurements.

Figure 8a depicts a scheme how the Prototype 1 detector looks like: it consists of an aluminium casing filled with the liquid scintillator EJ-309 (from company Eljen Technology) and 16 so-called Wavelength Shifting Fibres (WLSFs) Y-11(200) (from company Kuraray Trading Co.) which are crossing through the casing horizontally to the outside.
Each of the two fibre ends is connected to a 6 x 6 mm^2 Hamamatsu S14160-6050HS SiPM.
The SiPM connected to the fibre end on the right hand side of graph 8a lies 8.7 cm outside of the casing and is called SiPM 7. The left fibre end is connected to a SiPM named SiPM 6 which emerges the aluminium casing by 10.7 cm.

Throughout the experiments, Prototype 1 underwent a small adaption: while we used at first black towels to shield the SiPMs from light, we later replaced them by putting black caps over them, yielding a tremendous improvement of light shielding. This change of shielding was namely accompanied by a considerable decline of dark current (from 2 μA to 0.5 μA). Since this new shielding was used for the majority of the Prototype 1 experiments and for a better imagination of the actual Prototype, the black boxes are also shown in the upper graph. In order to fix the black boxes in their respective position to the casing, they were attached to it via a black tape. This served furthermore as prevention from light entering at the edges.

Figures 8b, 8c show the actual Prototype 1 detector from different perspectives.

The lengths and other characteristic properties of the previously mentioned components are listed in the following table:

size of the cuboid casing:	506.0 mm x 40.1 mm x 60.1 mm
thickness of the aluminium walls:	2 mm
size of the black cap over SiPM 7:	120.3 mm x 43.8 mm x 63.3 mm
size of the black cap over SiPM 6:	135.5 mm x 43.7 mm x 63.5 mm

Table 2: size of Prototype 1 components

Even though we will frequently use the term 'the Prototype 1 detector', it is important to note that the just described device has two seperated readout channels (SiPM 7 and SiPM 6), so it does deliver two signals instead of one. This implies furthermore that we can obtain two amplitudes and two efficiencies, which are correlated, though. The reason for this is the same as above: the SiPMs share the same scintillator and apart from that they share the same Wavelength-Shifting-Fibres, as well.

The main motivation for attaching 2 readouts to a scintillator was to assess occassional/potential spikes entering the data set. If such a spike signal occurs on one SiPM, but not on the other SiPM it can be ruled out from the data set as disturbing influence. However, having such a disturbing spike signal at both SiPMs simultaneously is highly unlikely and therefore suggests a real event.

Although it will be mentioned again later, the signal of SiPM 7 enters the amplifier board at board channel 9, while the signal of SiPM 6 enters it at board channel 10. This choice of connection was kept during all experiments performed with Prototype 1.

3.3 description of Prototype 2

Prototype 2 consists of a repeating sequence of components, which we denote as 'modules'.
These modules are arranged on top of each other, such that the readout positions between two neighbouring modules is either turned 90° to each other or such that they all are aligned in one direction.
It is schematically illustrated in figure 9b, 9d in top view and in figure 9a, 9c in side view.

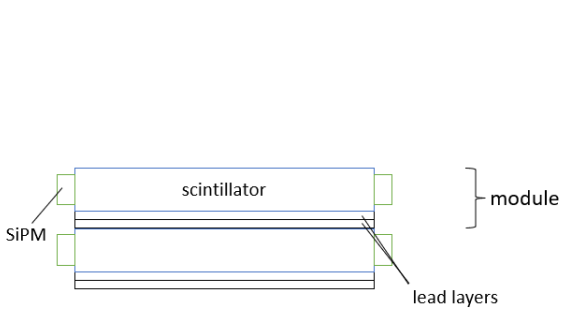

(a) sideview of Prototype 2 with aligned SiPMs

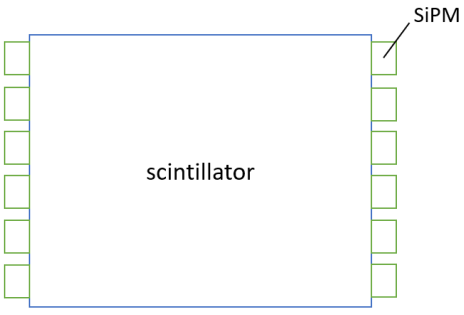

(b) topview of Prototype 2 with aligned SiPMs

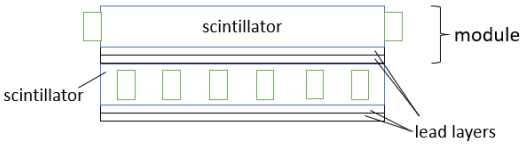

(c) sideview of Prototype 2 with rotated readout

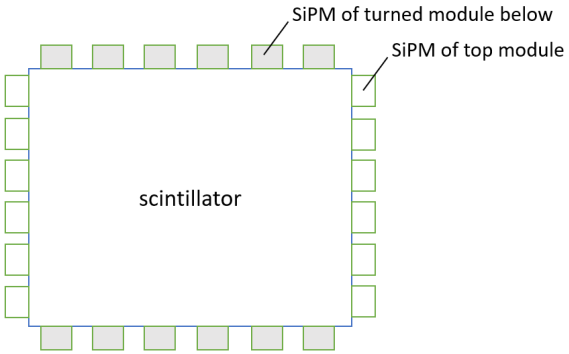

(d) topview of Prototype 2 with rotated readout

Figure 9: a Prototype 2 module viewed from different perspectives.

Unlike figures 9a - 9d suggest, the scintillator components used in our experiments were not realized as big, continuous scintillator but as several plastic scintillator bars.
In Figures 10a, 10b, one of the two used modules is shown from different perspectives.

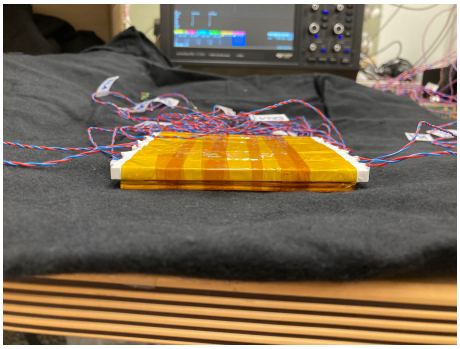

(a) sideview of a module

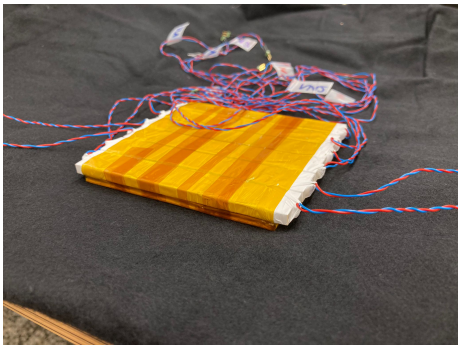

(b) oblique projection of a module

Figure 10: a Prototype 2 module viewed from different perspectives.

The bottom of each module is made up of 2 lead plates bound together with kapton tape.
On top of these 2 lead plates, there are 6 plastic scintillators forming 6 x 2 plastic scintillator detectors as described in section 'description of plastic scintillator detectors'. These detectors are then bound to the 2 bottom lead plates with kapton tape to fix their relative position.
The plastic scintillators are cuboid with size 110 mm x 16 mm x 5 mm and the lead plates are cuboids with size 101 mm x 101 mm x 2 mm.
They are arranged to each other such that the scintillator emerges the lead plate about 3-6 mm on each side.

3.4 measurement principles

Although the setups look quite different, the conceptual principles behind the measurements remain the same: charged particles propagating through the scintillator part of the detector produce photons therein, whereby the number of photons generated is related to the energy deposited.
A fraction of this light then propagates to the SiPMs, where it triggers (amplified) current pulses due to the avalanche effect. Afterwards the pulses are further amplified with an IFES amplifier board delivering a differential signal output.
Subsequently, the differential signal undergoes a conversion to a single-ended signal via a differential signal converter, realised as external unit.
From there the resulting single-ended signal is transferred to the oscilloscope with lemo cables, where it is displayed as a measureable signal.

Note that the origin of this charged particles triggering all these steps does not need to be a radioactive source. Instead, the light propagating to the SiPM can also come from Compton scattered electrons

(see section 'Compton scattering and energy calibration'). Therefore our detectors enable an indirect measurement of gamma radiation as well.
Unlike to Prototype 1 and the plastic scintillator detectors, Prototype 2, is additionally designed to measure electrically neutral particles (neutrons, gammas etc.). The lead plates between the scintillators should promote the creation of particle showers which are measurable because the secondary particles carry charge producing bremsstrahlung and scintillation light.

4 Used measurement equipment

4.1 amplifier boards

Throughout the experiments we used four different amplifier boards, depicted in figures 11a-11d.

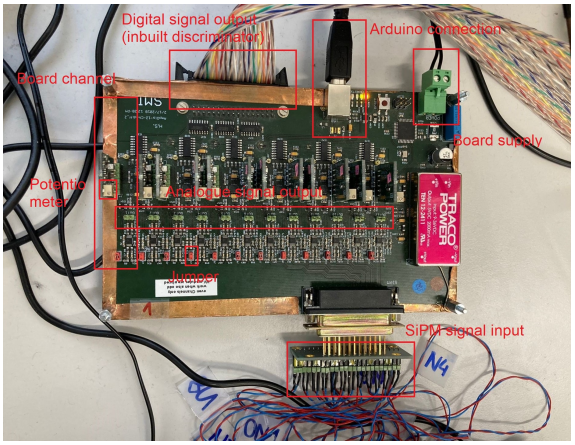

(a) Board 1

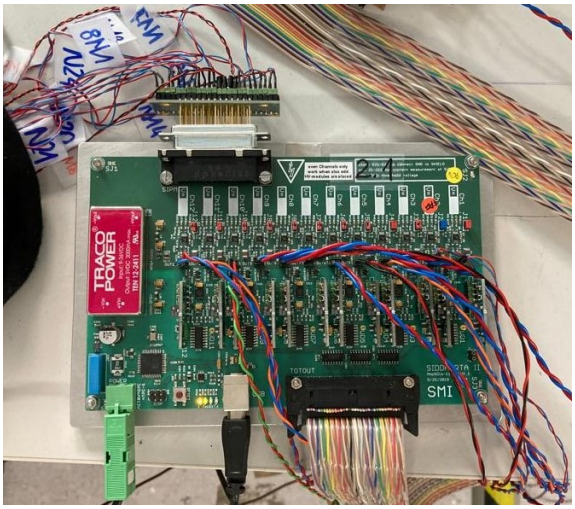

(b) Board 2.1

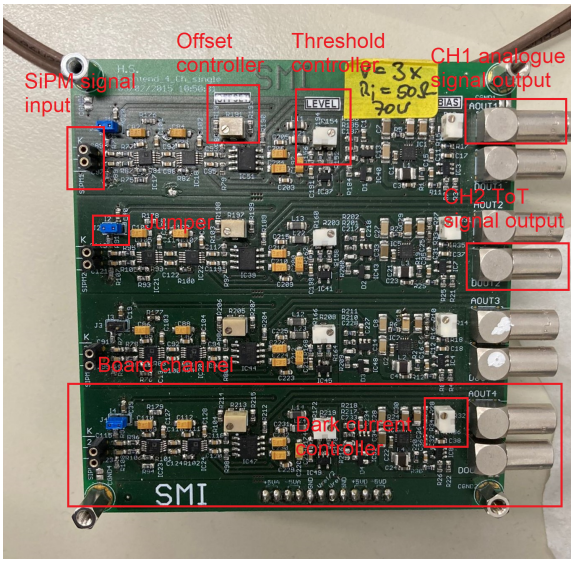

(c) little Board/ Board 3

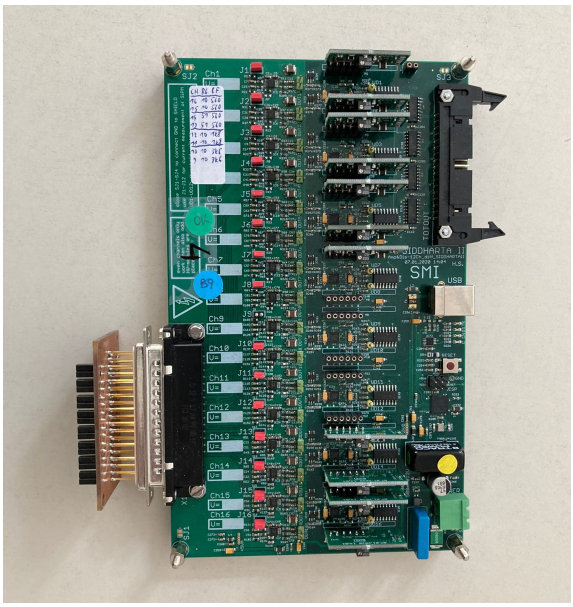

(d) Board 4

Figure 11: overview over the used amplifier boards.

For the majority of the measurements, we used amplifier board 1, the amplifier board displayed in figure 11a. It has 12 board channels with a board gain of V=5 and input resistence R_i=51 Ω.
Relevant ports are marked and labelled in figure 11a including SiPM supply, amplified analogue and digital output.
For a rough adjustment of dark current on a board channel, the screw on the potentiometer ('pottie') of the respective HV module can be used. For fine adjustments of dark current and also for digital

threshold adjustments, a laptop with appropriate software is needed.
Important to note is that after the amplification stage, the analogue signal output is a differential signal as well as the digital output.

The usage of the amplifier board 2.1, illustrated in figure 11b, was limited to the TDC experiments conducted in the section 'Prototype 2 experiments'. Board 1 and Board 2.1 resemble in various aspects: especially as far as the number of board channels and the type of output signals (differential signals) are concerned. Further similarities are the HV modules that allow to set dark currents manually and the Arduino unit (used for software-based dark current adjustments and for discriminator threshold settings).

The amplifier board 3 showed in figure 11c has a board gain of V=3 and internal resistence R_i=50 Ω. For its four board channels, it can provide a maximum, total bias voltage of 70 V.
A major difference to the previous two amplifier boards is that, it outputs single-ended signals instead of differential signals. It was mainly used for 6 x 6 mm^2 SiPMs and enabled the adjustment of dark current for each board channel by turning the screw at the corresponding potentiometer below the 'bias' label. Via turning the screws at the potties below the labels 'offset' and 'level', one could change the voltage offset and the discriminator threshold for the corresponding board channel.

Apart from the number of board channels, which is 16, amplifier board 4 (see figure 11d) is built like amplifier board 1 and 2.1: threshold adjustments and fine-tuning of dark currents can be done via software from a laptop for example, while rough changes of the dark current can be made by manipulating the potentiometer setting. As amplifier board 2.1, it was applied in the TDC measurements of section 'Prototype 2 experiments' only.

4.2 oscilloscopes

In total, three different oscilloscope models from the company Teledyne Lecroy were used for the measurements of this thesis.
These are the WaveSurfer 3104z 1GHz Oscilloscope 4GS/s, the WaveRunner 625Zi 2.5 GHz Oscilloscope 40GS/s and the WavePro 735Zi 3.5 GHz Oscilloscope 40Gs/s.
The following table gives an overview over some relevant properties of the three oscilloscopes:

	# osci ports	m= # measurement routines	n= # math modes	inbuilt histogram function
WaveSurfer	4	6	2	No
WaveRunner	4	8	8	Yes
WavePro	4	12	12	Yes

Table 3: properties of the used oscilloscope models from Teledyne Lecroy

Two frequently used examples for measurement routines are 'Minimum' (measures negative-valued signal amplitude heights) or the routine 'dt@lv()' that can be used for delay measurements between two input signals.
The measurement routines are labelled with 'Px' where x=1,...,m (see table 3) enabeling up to m different measurements P1,...,Pm.
In addition to this measurement routines, we need to specify a math-mode that indicates how the data should be processed e.g. as histograms or event-order diagrams).
It is abbreviated with 'Fy' where y=1,...,n.
The last two oscilloscopes have a math mode called 'Histogram' that sorts the measured values automatically in histogram bins and permits a record of more than 2 million counts per measurement routine.
In contrast, the WaveSurfer supports only the 'trend' math mode that allows to record up to 1000 consecutive measurement values per measurement routine.

Quite often, the consecutive measured values of the trend function are later processed to a histogram via appropriate programs.
Experience in evaluation revealed that for the majority of the cases 25 bins were sufficient to generate

a meaningful histogram.
This may also be tied to the fact that many measurement samples included 1000 counts, the upper limit of values the WaveSurfer oscilloscope can save.
In many cases, the interval that is divided into N bins ranges from the measured minimum value, x_{min}, to the measured maximum value, x_{max}, giving a binwidth bw=$\frac{|x_{max}|-|x_{min}|}{N}$.
For histograms generated with the WaveRunner or the WavePro, however, the interval seperated into bins can be bigger.
Furthermore we made the convention that the counts to a certain bin are associated with the average of the left and right bin value: $\frac{x_i+x_{i+1}}{2}$, where i=1,...,N.

4.3 bias voltage and dark current

Apart from scintillation light from charged decay products, there also occurs a small number of avalanches due to thermal radiation.
The thereby generated current is called dark current and serves as a characteristic measure for adjusting the bias voltage.
From a conceptual point of view, the adjusted dark current plays an important role to ensure reproducability since it changes the amplification factor of the SiPM.
For example: increasing the measureable dark current increases the bias voltage and broadens as well the depletion region. As a further consequence, the magnitude of the electric field in the pn^+ junction rises, leading to more multiplication processes.
But this means eventually that the probability for a charge carrier to generate an avalanche in the hit SPAD is increased. [11]
In our case, the dark current of a SiPM was determined by connecting a Fluke Multimeter to the extra foreseen pins on the board channel the SiPM is connected to. Throughout a measurement run, both pins on a board channel are connected with a jumper, closing the circuit (see figures 11a - 11d).
Keep in mind that an incomplete shielding from light also contributes to the measured dark current, which is unintended. A dark current contribution by incomplete shielding is often accompanied by great dark current fluctuations and thus it can be quite confidently distinguished from a pure thermal radiation contribution.

4.4 radioactive sources

The form and originating processes of measured spectra varies depending on the radioactive sources.

Sr-90 undergoes β^--decays (see figure 12a) and the thereby produced electrons create the scintillation light 'directly', meaning that the beta ray electrons excite the electrons of the scintillator molecules or even knock them out (ionization). Refilling of the unoccupied orbitals or falling back to lower energy levels results in emission of light with a certain wavelength. So if those beta rays propagate through the scintillator, they lose kinetic energy due to the photon emission until they either come to rest or leave the scintillator. [14]

On the other hand, the used radium pointer produces mainly high energetic photons (gammas), which do not generate scintillation light by themselves since they are electrically uncharged.
However the gammas can produce scintillation light 'indirectly' if they perform Compton scattering on freely moveable electrons in the scintillator or photo effect. Those scattered electrons then create scintillation light via excitation and decay of energy levels as it was just explained for Sr-90.
The possible energy transfers on this electrons are not arbitrary but are within a limited range as will be discussed more detailed in the next section.
Assuming that the scintillator size is suitably chosen, the Compton scattered electron deposits all its kinetic energy in the scintillator as scintillation light. Provided that all this light is detected by the SiPMs and converted into signals, the measured amplitude spectrum of the gamma decaying source corresponds to an image of the energy spectrum of the Compton scattered electrons. [14]

For this thesis, another important gamma producing source is Co-60, which obeys the decay scheme shown in figure 12b.

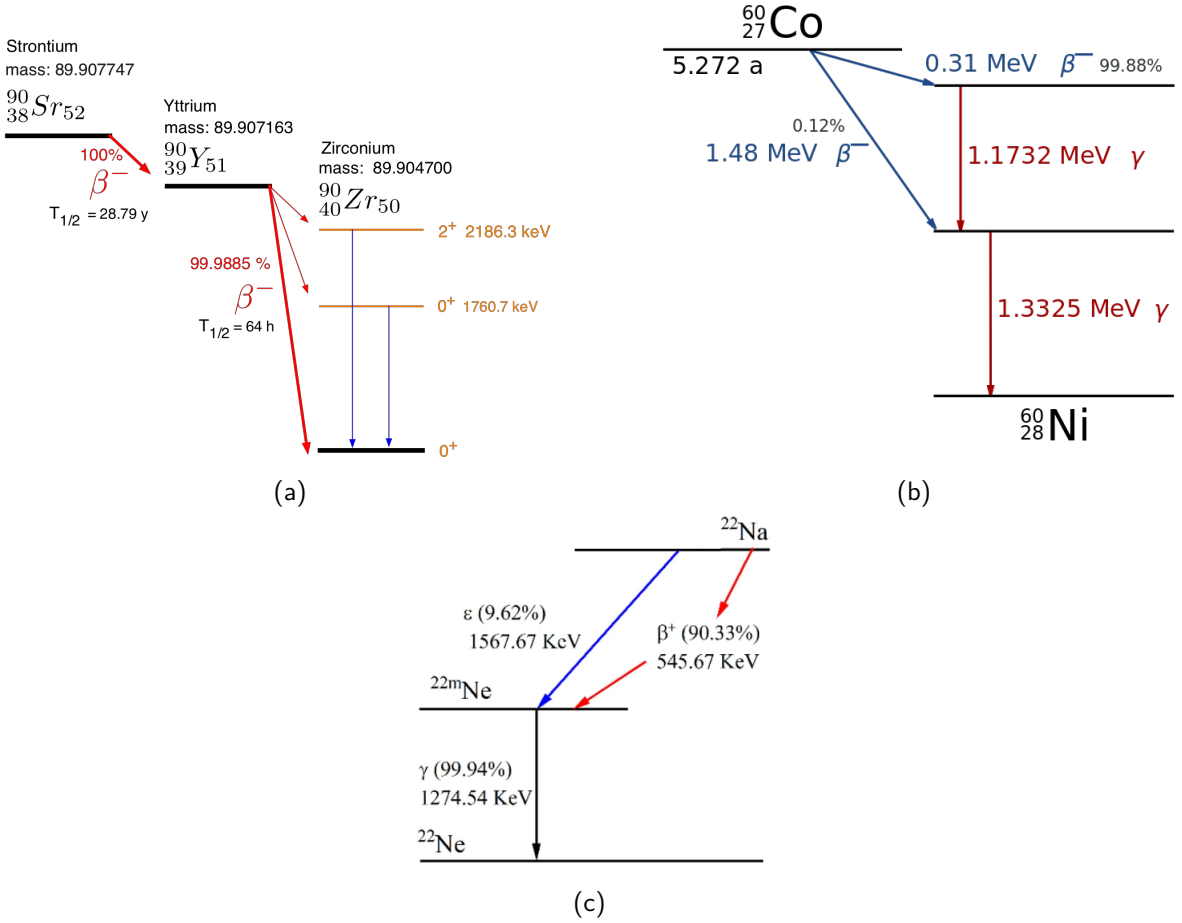

Figure 12: decay schemes of used radioactive sources; sources: [5],[6],[7]

β^+-rays, i.e. positrons from e.g. a Na-22 are indeed electrically charged but they annihilate with a nearby electron to two gammas with energy E_γ=511 keV, in accordance with energy- and momentum conservation.
Following the decay channel scheme in graph 12c we see that after undergoing the dominant β^+-decay, the daughter nucleus is still in an excited state.
Therefore a gamma with E_γ=1275 keV is emitted such that the nucleus gets into the ground state, $^{22}_{11}Ne$.
For the sake of completeness, one needs to quote the electron-capture (EC) as well, where we either get contributions from an emitted X-ray-photon (respectively its Compton-scattered electron) or from the scintillation of the emitted Auger electron. This decay occurs in $\approx 10\%$ of the cases.

4.5 Compton scattering and energy calibration

For the previously mentioned voltage-energy calibration, we will use well-known literature values as well as the formula for the so-called Compton edge. [8]
One can show, that the energy of an electron after Compton scattering is given by

$$E'_e(\varphi) = E_\gamma - E'_\gamma(\varphi) = E_\gamma \left(1 - \frac{1}{1 + \frac{E_\gamma}{m_e c^2}(1 - \cos(\varphi))}\right) \tag{1}$$

Based on equation 1, we recognize that for fixed ingoing photon energy, E_γ, the energy of the Compton-scattered electron depends only on the scattering angle, φ, seen in figure 13.
Analysing $E'_e(\varphi)$ as a function, we find that it is a continuous function in the interval $\varphi \in [0, \pi]$, so the energy spectrum of the scattered electron is not discrete but continuous.

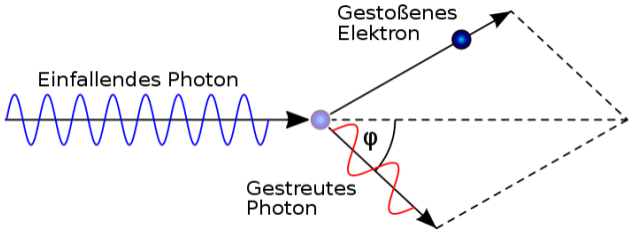

Figure 13: scheme of Compton effect with scattering angle φ; source: [8]

However the possible energy values the scattered electron can take is limited from above and below since the function has extremas at $\varphi = 0$ (minimum energy: $E'_e(\varphi) = 0$) but also at $\varphi = \pi$.
The maximum value for $E'_e(\varphi)$ is realized for back to back scattering and amounts to:

$$E'_e(\varphi = \pi) = \frac{E_\gamma}{1 + \frac{m_e c^2}{2E_\gamma}} \tag{2}$$

It is called the Compton Edge assigned to the considered transfer.
Theoretically, this means that for a recorded voltage histogram (which is linked to the energy spectrum of Compton scattered electrons), there should be a sharp edge at the position of the Compton edge since no higher energy values can occur.
In practice, the edge is smeared out due to effects like secondary Compton scattering, i.e. Compton scattered photons perform again Compton scattering with another electron.

Different sources run through different decays with distinct photon energies, E_γ, thus the Compton Edges are characteristic quantities for the respective source.
For Na-22, there are two Compton edges: the first at 340 keV and the second at 1062 keV.

Although Compton scattering forbids that $E'_e(\varphi) = E_\gamma$ (see equation 1), one obtains nevertheless a 'Full Energy Peak' (spectral line at the energy E_γ) in the measured spectrum.
There can be two reasons for this: either the inner photoelectric effect is responsible or the detector is so big that the scattered light cannot leave it.

This thesis treats also an alternative approach for the energy calibration of detectors, making use of cosmics and exploiting the fact that they are Minimal Ionizing Particles (MIPs).
This approach is presented in section 'Plastic scintillator experiments'.

4.6 shaping amplifier and ADC

For meaningful amplitude measurements, it is crucial to reduce the noise as good as possible while preserving the pulse height information at the same time.
One way to deal with this problem is by using an oscilloscope and some countermeasures (bandwidth limitation, termination) described more in detail in one of the paragraphs below.
Since the oscilloscopes at disposal have only 4 incoming ports, but one module of Prototype 2 provides already 12 different signals, an alternative approach is needed.
In order to deal with both challenges, damping noise effects and simultaneous recording of many readout channels, we will proceed like this for the Prototype 2 measurements: in a first step, the signals will be reshaped with a so-called shaping amplifier to optimize the signal-to-noise ratio and in a second step, the amplitudes of the reshaped signals will be determined and digitized by a so-called ADC, which we will describe in one of the lower paragraphs.[3].

The shaping amplifier (or spectroscopy amplifier) filters out frequency components from the input signals where noise is at its greatest. This corresponds to a limitation of bandwidth and changes the shape of the signal, since the distribution of Fourier components it's made of has changed.

[3]The signals to be reshaped are of the type shown in figure 3

As a consequence, the characteristic, analogue signal with unbiased amplitude, A, is transformed into a smooth, Gaussian signal with shortened tail and amplitude, a $\propto$ A.

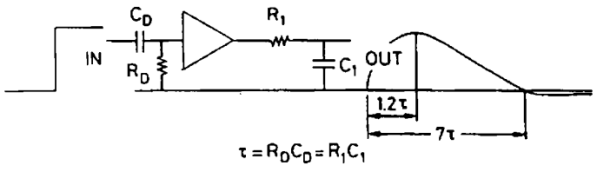

(a) CR-RC pulse shaping network

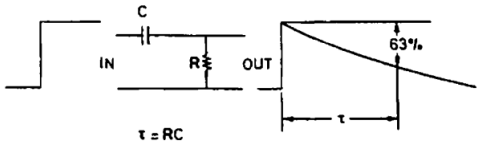

(b) CR high-pass filter, differentiating circuit

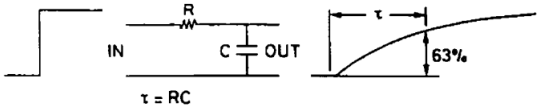

(c) RC low-pass filter, integrating circuit

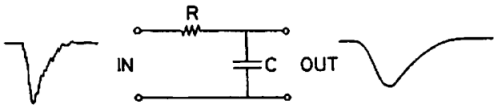

(d) Noise filtering by integration

Figure 14: CR, RC, CR-RC frequency filters acting on a step function pulse, respectively on a characteristic signal. Source: [14]

In most commercially available amplifiers, pulse shaping is realized in networks that are based on 2 methods: delay line shaping and RC differentiation-integration.
The latter is also known as CR-RC pulse shaping and is the most widespread technique.
The basic components of an CR-RC pulse shaping network are cascaded CR differentiators and RC integrators, as shown in the circuit in figure 14a. For better understanding, we will discuss its operating principles in the context of an incident step function pulse.

A CR differentiator is understood to be a high-pass filter which attenuates frequency components smaller or equal to the cutoff frequency $f_c = \frac{1}{2\pi \cdot R \cdot C}$.[4]
Its effect on a step function pulse is illustrated in figure 14b. As is seen, the flat part of the pulse (i.e. the top) is degraded and made to decay to the baseline, thereby shortening the pulse. In contrast, the fast rising part of the pulse, which depends on the higher frequencies, is not affected.
The quantity $\tau = R \cdot C$ is denoted as time constant of the circuit and needs to be small compared to the width of the pulse; otherwise the pulse passes without large change.

Opposing to that, an RC integrator is a low-pass filter that attenuates frequency components greater or equal to f_c. In figure 14c, the action of an RC integrator on an inciding step function pulse is depicted. One clearly observes that the filtering of high-frequency components leads to a significant smearing of the fast rising pulse part. For typical SiPM signals, for example, this happens as well but at the same time, fluctuations in a noisy signal are smoothed out (see figure 14d). Keep in mind that for the integrator to work properly, τ must be large compared to the pulse, since otherwise the pulse will not be changed much.

Cascading these circuits and inserting an operational amplifier in between (see figure 14a), thus causes filtering at low (differentiation) and high (integration) frequencies.
The resulting output pulse then has an improved signal-to-noise ratio and looks in case of an ingoing step function pulse like the OUT pulse in figure 14a. In most cases, optimum signal-to-noise ratio is obtained with equal differentiation and integration time constants, however, the absolute value of this constant depends on the particular characteristics of the pulse. [14]

[4] Here R refers to the resistance and C to the capacity of the circuit, shown in figure 14b .

In this thesis, the used shaping amplifier was a CAEN N568E 16 channel Spectroscopy Amplifier (see figure 15). Although its operating principle is probably based on CR-RC pulse shaping, in practice we do not manipulate the signals on the hardware level, i.e. on the level of capacitors and resistors.
Instead with the serial port of the shaping amplifier module and appropriate software (Tera Term), one can manipulate some properties of the Gaussian signal as desired.
Among those, the most relevant parameters are Coarse Gain, Shaping Time and Out Polarity.

The Coarse Gain takes the possible values: 0, 1, 2, 4, 8, 16, 32, 64. It contributes to the proportionality constant between the amplitudes, a and A but its value does not equal the actual proportionality.
The Shaping time is here defined as the rise time from 0 mV to the amplitude value, a, and is given in μs.
The parameter 'Out Polarity' can be chosen as positive (Pos) or negative (Neg) and governs whether a is positive-valued or negative-valued.

Figure 15: picture of a CAEN N568E 16 channel Spectroscopy Amplifier; source: [10]

An ADC (abbreviated for Analogue Digital Converter) converts (as its name suggests) a positive-valued analogue signal to a digital output.
For all experiments except those of Prototype 2, this job was done by the oscilloscope which used a 50 Ω termination and an internal low bandwidth setting to limit the consequences of noise (occuring during transportation and different frequency response).
As briefly mentioned above, the signals to be converted/digitized in the Prototype 2 experiments by the ADC are analogue, single-ended, Gaussian shaped voltage pulses.

Figure 16: rack with inserted PADC (top module) and inserted TDC (middle module).
For both, the ADC and the TDC, we plugged in a 50 Ω termination at one of their respective Lemo connectors to prevent possible disturbing influences from the unused connector. The TDC is here connected to a flatband cable that transports the signal of 32 TDC channels.

The ADC that was used in that experiments was a Peak-sensing ADC (PADC) from the company CAEN with model number Mod.V785 (see figure 16).
It provides two ports for ingoing flatband cables (with 16 pin pairs each) and thus the possibility to digitize 2 x 16=32 input signals at once.
The Lemo connectors on the PADC serve to feed in a so-called gate signal; this is a digital signal with a falling edge and a rising edge that governs the measurement. On the one hand, they define when a measurement shall be recorded and on the other they provide the time region in which the PADC shall look for the highest value of the Gaussian pulse. So if an event has happened, a gate signal will be produced and simultaneously the PADC looks for the maximum value of the pulse occuring within the gate signal. After the end of the gate that value is stored in a file in binary form.

For a meaningful measurement, two things are of very importance:
First, the gate signal must be at least slightly broader than the maximum width of the Gaussian pulses. Otherwise, it's possible that the PADC writes for certain pulses a local maximum to the file instead of the global maximum.
Secondly, the gate signal must be based on a signal with a well-chosen threshold value to include all events in the desired range but exclude noise.

4.7 TDC

The digitalization of time-related inputs/data is done by a Time-to-Digital-Converter (TDC).
Similar to the amplitude measurements, all time related measurements except of the Prototype 2 experiments were conducted with the oscilloscope which takes the role of the TDC.
In the course of Prototype 2 experiments, we will work with a TDC from the company CAEN with model number Mod.V1190A (see figure 16).
It has 4 ports for ingoing flatband cables (with 32 pin pairs each), giving the possibility to measure 4 x 32=128 signals at a time.
Opposed to the ADC, the signals going into the TDC are digital, differential voltage pulses from the amplifier board.

Using the CAEN TDC, there is no need to convert the signal into single-ended or Gaussian form since it can process differential signals and those are insensitive to noise as mentioned in the very first chapter. Another facilitating circumstance is that also the type of measurement we perform with the CAEN TDC

is under well-adjusted conditions quite insensitive to noise: The conducted experiments restrict namely to Time-Over-Threshold (ToT) measurements, where the timespan between falling and rising edge is measured. Given a properly set threshold and the absence of large noise, one expects that the threshold level cannot be crossed in either direction unless a real event was present.
So for a signal with amplitude A >> TH and some noise situated on the peak, the measured ToT-value is the same as if the noise was absent.

However, it is possible that noise in superposition with a real event signal of amplitude A >> TH leads to a long ToT-signal followed by several, much shorter signals. The latter result from multiple jumps above and below the threshold TH, which are induced by noise at the rising edge.
This disturbing effect is called 'jittering' and results in several short ToT events. Possible sources for noise relevant in jittering are for example mobile phones, radio frequencies or ripple from the 50 Hz current coming from the socket.

Similar as for the ADC, the TDC has connectors for ingoing signals in order to indicate the time interval in which the ToT measurement must be conducted. The difference, though, is that the TDC measurement does not require the full gate signal for this but the end of the gate only.
Assuming that the end of the gate happens at the time, τ, it forms together with a software-defined timespan, Δt, the time window $[\tau\text{-}\Delta t, \tau]$ for the measurement.

A further benefit the ToT measurement offers is the determination of the corresponding amplitudes due to a widely linear correlation between these quantities. This fact becomes noticeable if we plot the ToT against the corresponding amplitudes as we did in a schematic graph in figure 17.

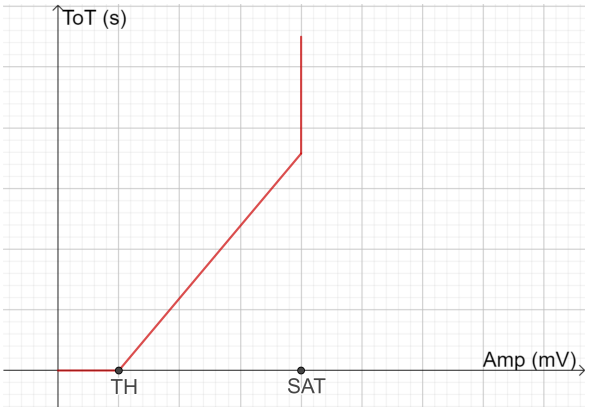

Figure 17: functional correlation of amplitude and Time-Over-Threshold.
Since the amplifier board has a maximum output voltage, denoted with SAT, very high energy events cannot have arbitrary high amplitudes but they are all assigned with the maximum signal amplitude, SAT (saturation effect). Depending on the actual deposited energy, the signal lasts longer or shorter and thus the ToT at SAT can take different values.
Keep in mind that the correlation of both quantities within the interval [0, SAT) can be described as a function and that the progression at SAT as a straight vertical line is idealized.

The upper limit of correlation arises because the amplifier board has a maximum output of SAT=800-900 mV, while the time the signal is above the threshold can vary due to saturation effect. Therefore the ToT measurement enables to extract more information from the events in the SAT-near region as from a pure amplitude measurement.
Again for a faithful result it's important to impose a well-chosen threshold on the measurement. If the threshold is set to high, some real events are excluded completely since they didn't cross the threshold. Therefore the ToT equals 0 making their distinction from noise events impossible since they also have a ToT of 0. This explains why in figure 17 the amplitudes smaller or equal than the threshold are mapped all to the ToT value of 0.

5 Determination of SiPM characteristics

Measuring the current voltage characteristic of a SiPM serves as a good approach/starting point to become familiar with its behavior under different applied voltages.
For this purpose, we used the setup shown in figure 18, where we applied the SiPM in reverse bias, as we will always do.
Plotting the measured currents with the adjusted voltages for 4 different 'double SiPMs'[5], we obtain the characteristics shown in figures 19a - 19d.

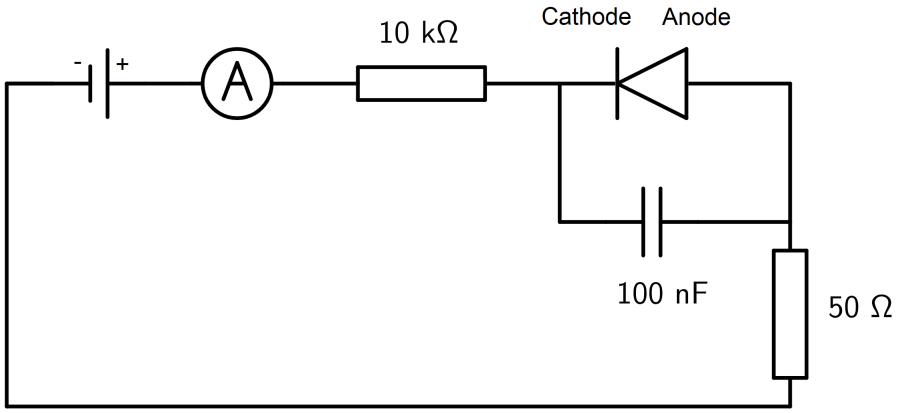

Figure 18: circuit used for determination of SiPM characteristics. Notice that the diode symbol represents the examined SiPM and also that it is inserted in reverse bias.
The resistor has 10 kΩ and the used condensator has 100 nF (type 104z). [1]

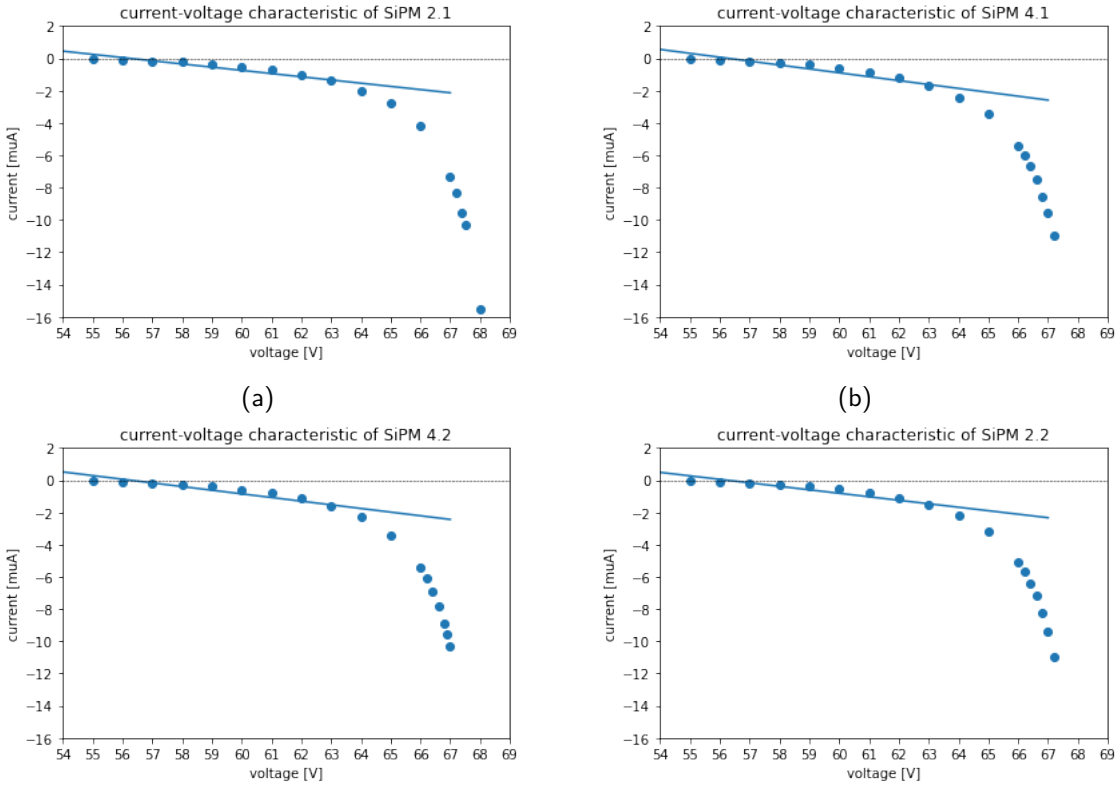

Figure 19: current-voltage characteristics for 4 different double SiPMs

[5]these are defined as 2 4 x 4 mm^2 SiPMs connected in series. The double SiPMs involved in the characteristics measurement, consisted of 2 ASD-NUV4S-P SiPMs from the company AdvanSiD.

The measurement of the characteristics was repeated later on, but this time with single 4 x 4 mm^2 ASD-NUV4S-P SiPMs from AdvanSiD that were pairwise attached to one common platine.
Unlike the double SiPMs, those pairwise attached SiPMs are not coupled and generate two seperate signals, instead of one common.
In total we had four SiPM pairs of this kind, where the following SiPMs were paired:
SiPM 3A and SiPM 3B
SiPM 3C and SiPM 3D
SiPM 4A and SiPM 4B
SiPM 4C and SiPM 4D

Figures 20a - 20h depict the obtained current-voltage characteristics.

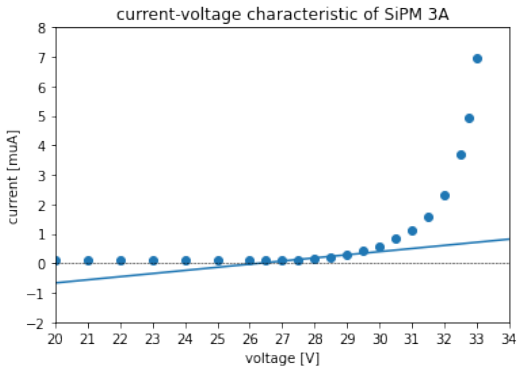

(a)

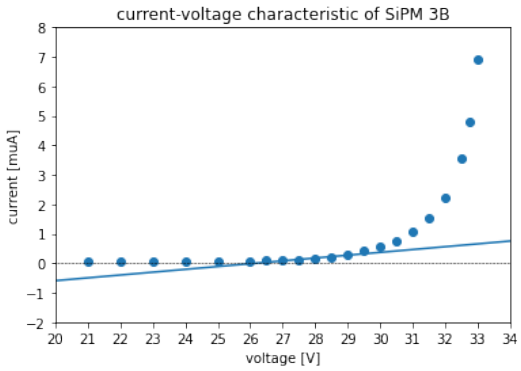

(b)

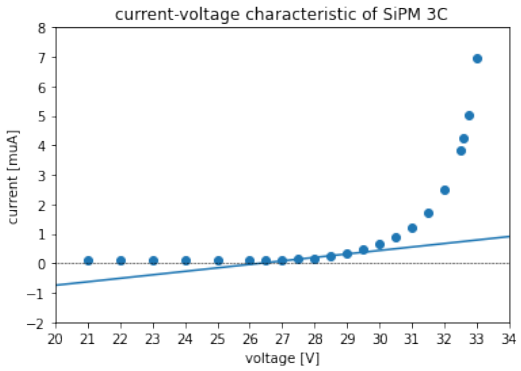

(c)

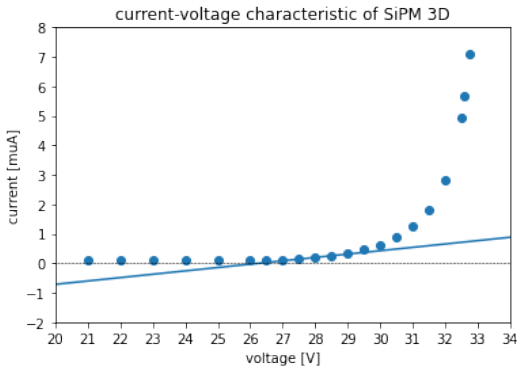

(d)

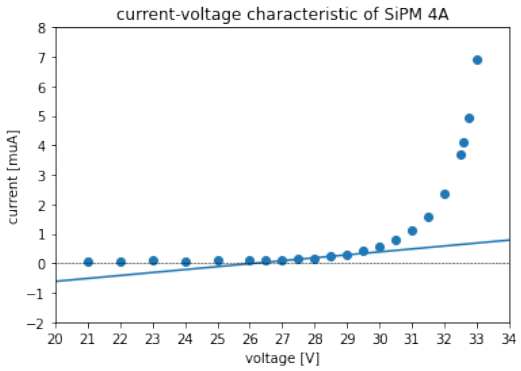

(e)

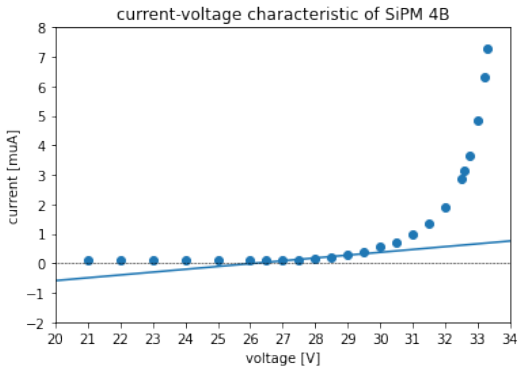

(f)

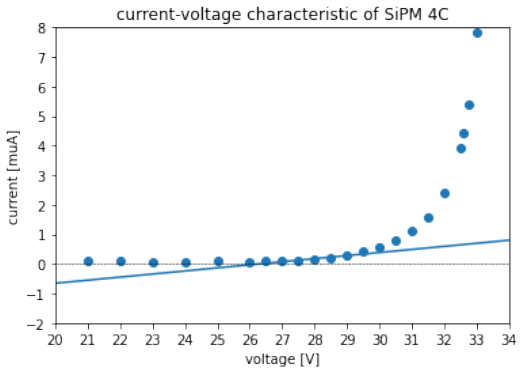

(g)

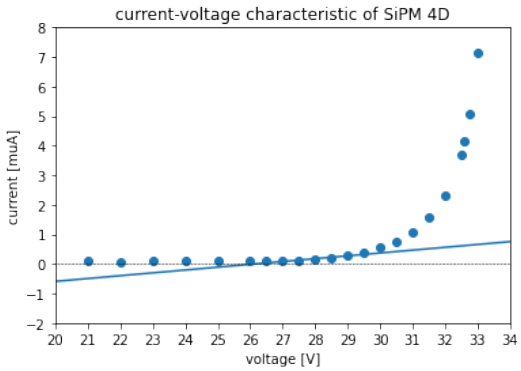

(h)

Figure 20: current-voltage characteristics for 8 different 4 x 4 mm^2 SiPMs including a linear fit for the determination of breakdown voltage

Looking at these characteristics, we find that all of them can be divided into basically three regions. On the very left side of the diagram, there is the non-conductive region, i.e. the voltage region where thermal radiation leads to no avalanches and thus to no current pulses. Above a certain bias voltage, however, thermal radiation triggers avalanches and the thus created current grows exponentially with rising bias voltage. The section with exponentially rising current can now be further subdivided into a linear region, where the linear term dominates the voltage-current correlation and a region, where the higher-order exponential terms dominate.

An important quantity for the SiPM characterisation is the breakdown voltage. It is the bias voltage value that marks the transition between the non-conductive voltage region and the linear region.
We determined the value for the breakdown voltage graphically for all tested SiPMs (see figures 19a - 19d and 20a - 20h) and listed the resulting values in table 4 and 5.
The graphical determination was done in the following manner: we applied a linear fit (blue line) to the linear region and determined its intersection point with the x-axis, i.e. the line where the current is equal to 0 μA (dashed black line). The breakdown voltage is then the abscissa of the intersection point.

SiPM name	breakdown voltage
SiPM 2.1	56.2 V
SiPM 4.1	56.3 V
SiPM 4.2	56.2 V
SiPM 2.2	56.2 V

Table 4: The breakdown voltage of the double SiPMs (2 ASD-NUV4S-P SiPMs connected in series) obtained via graphical evaluation

SiPM name	breakdown voltage
SiPM 3A	26.3 V
SiPM 3B	26.2 V
SiPM 3C	26.3 V
SiPM 3D	26.3 V
SiPM 4A	26.2 V
SiPM 4B	26.1 V
SiPM 4C	26.3 V
SiPM 4D	26.1 V

Table 5: The breakdown voltage of the 4 x 4 mm^2 ASD-NUV4S-P SiPMs obtained via graphical evaluation

As expected, all tested double SiPMs show a similar current-voltage behaviour:
the SiPMs are in a non conductive state until 56.2 V (breakdown voltage), followed by the linear region

that ranges from the breakdown voltage to approximately 64 V. Beyond this voltage, the current-voltage correlation is governed by the higher-order exponential terms.

In contrast, the non-conductive region for the 4 x 4 mm^2 SiPMs ranges until 26.3 V (breakdown voltage), where we have a constant, negligible current of 0.08 μA to 0.09 μA.
The region of linear correlation spans from the breakdown voltage to about 29 V.
Analogous to the current voltage characteristics of the double SiPMs, the linear region is followed by the region of exponential correlation.

6 Plastic scintillator experiments

In the next experiment, 2 different plastic scintillator detectors were tested, which were similar to those depicted in figures 6a, 6b, but with the double SiPMs used in the voltage-current characteristics measurement.[6]
The double SiPM pairs 2.1 and 4.1 as well as 2.2 and 4.2 were mounted on 2 opposing sides of the respective detectors as shown in figure 21.
Both cuboid plastic scintillators had the following dimensions: 100 mm x 41 mm x 10 mm.

Figure 21 shows the used setup schematically:
a radium pointer was positioned on top of one of the plastic scintillator detectors such that it is centered with respect to the double SiPMs.
Both, the detector and the pointer, were put in a black box, in order to shield the SiPMs from external light.
Before the SiPM signals are transported to the oscilloscope (WaveSurfer), they are amplified by an amplifier board (board 3) as mentioned in section 'measurement principles'.

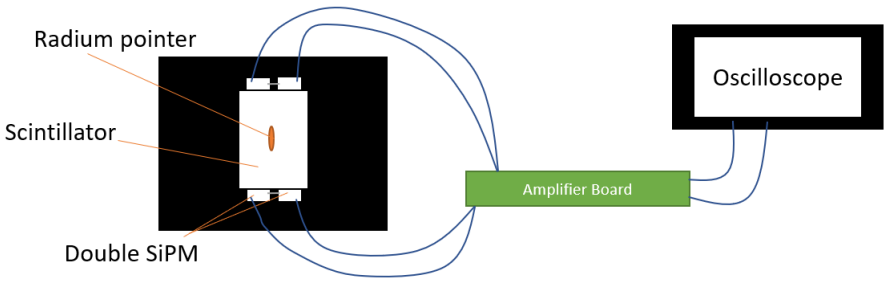

Figure 21: scheme of setup

A photo of the setup with one of the plastic scintillator detectors in use, can be seen in figure 22.

[6]Again, with a double SiPM we mean 2 SiPMs connected in series.

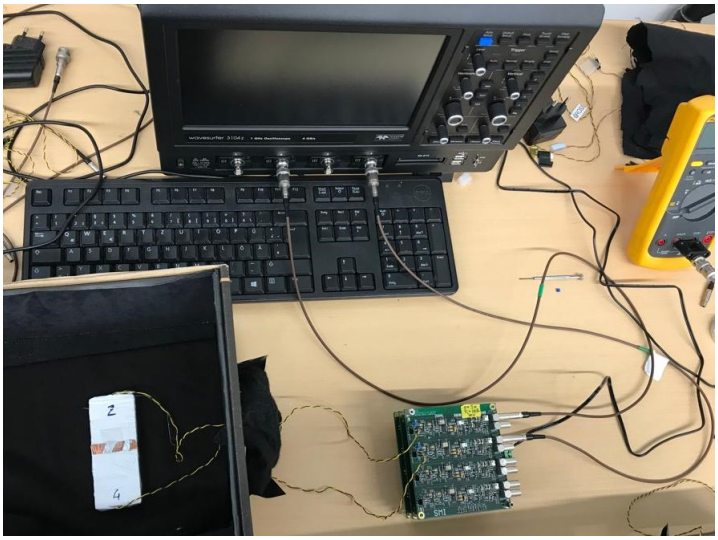

Figure 22: photo of used setup

Table 6 sums up the assignments of plastic scintillator detectors, SiPMs, amplifier board channels and oscilloscope channels.

plastic scintillator detector 1		
SiPM name	amplifier board channel	oscilloscope channel
SiPM 2.1	1	2
SiPM 4.1	2	4
plastic scintillator detector 2		
SiPM name	amplifier board channel	oscilloscope channel
SiPM 2.2	1	2
SiPM 4.2	2	4

Table 6: assignments of plastic scintillator detectors and SiPMs to their amplifier board channels and oscilloscope channels

For each plastic scintillator detector, we conducted three runs in which we measured the analogue signal amplitudes of its SiPMs.
For all runs, we chose the analogue signal entering at osci channel 2 as triggering signal with a threshold fixed at -202 mV.
All involved double SiPMs were adjusted to a dark current of 5 μA - a setting that was kept for all runs.

Parallel to the measurement, the measuring time was stopped to compare the event rates.
The number of counts, the measuring time as well as the calculated event rate are collected in table 7.

	for plastic scintillator detector 1		
number of measurement	measured counts ± 1 count	measuring time ± 1 [s]	rates $[s^{-1}]$
first measurement	251	101.7	2.47
second measurement	251	99.6	2.52
third measurement	251	99.9	2.51
	for plastic scintillator detector 2		
number of measurement	measured counts ± 1 count	measuring time ± 1 [s]	rates $[s^{-1}]$
first measurement	251	97.7	2.57
second measurement	251	102.5	2.45
third measurement	251	105.0	2.39

Table 7: determination of total counts per run, measuring time and rate

In figure 23, we show exemplarily the event-order diagram of the first measurement run using plastic scintillator detector 1.

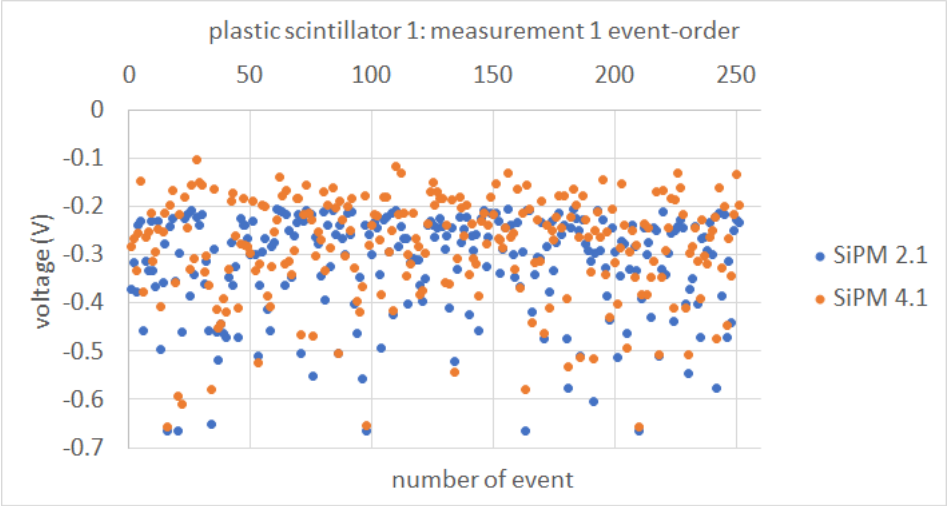

Figure 23: event order diagram of plastic scintillator detector 1: the x-axis represents the event number i.e. the enumeration of the events in which they occured. The y-axis value to the i.th event is the corresponding measured voltage in V.

The subsequently recorded events were later processed into histograms, of which we show the 3 runs of the first plastic scintillator detector (figures 24a - 24c).

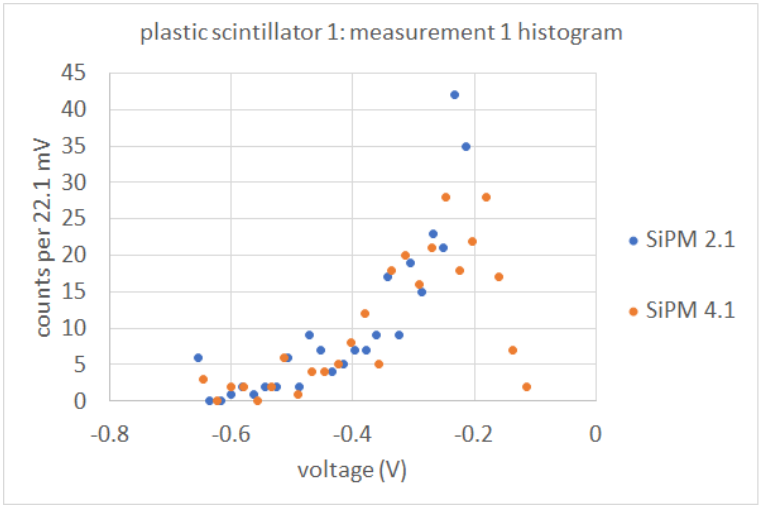

(a)

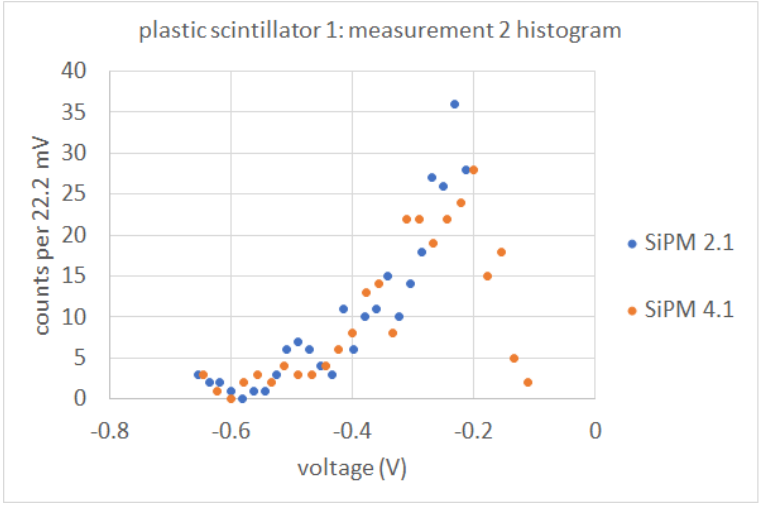

(b)

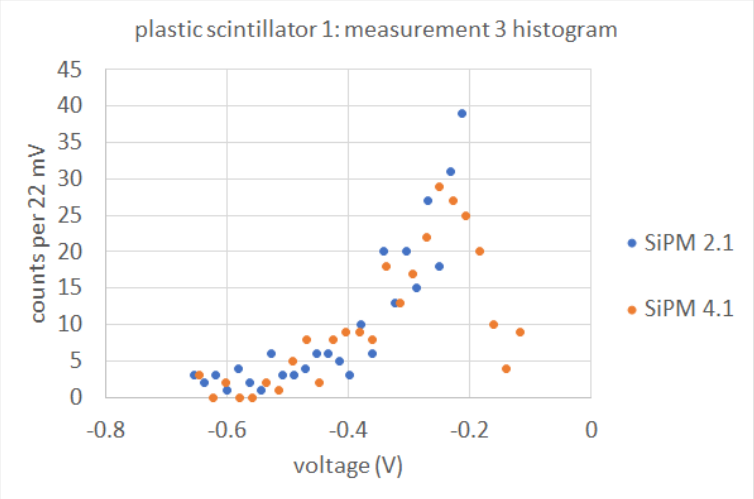

(c)

Figure 24: histograms of plastic scintillator detector 1, bins: 25

For comparisons among different runs, the count numbers within the intervals 200 mV - 300 mV and 300 mV - 500 mV are gathered in table 8.
Thereby the square root of counts in these intervals serves as associated standard deviation.
To avoid potential deviations, the counts within these intervals were determined from the event-order values and not from the values and counts of the histograms.

The third column in table 8 lists for each run and detector the measured mean amplitude difference including standard deviation.
This quantity was obtained by first taking the difference of the SiPM 2.1/2.2 amplitude with the SiPM 4.1/4.2 amplitude for each event number.
Subsequently, we then averaged over all these event-related differences and calculated the standard deviation as well.

plastic scintillator detector 1			
	Counts within 200 mV-300 mV	Counts within 300 mV-500 mV	SiPM 2.1 - SiPM 4.1
1st run	for SiPM 2.1: (139 ± 12) for SiPM 4.1: (97 ± 10)	for SiPM 2.1: (92 ± 10) for SiPM 4.1: (78 ± 9)	(-0.035 ± 0.046) V
2nd run	for SiPM 2.1: (138 ± 12) for SiPM 4.1: (97 ± 10)	for SiPM 2.1: (94 ± 10) for SiPM 4.1: (84 ± 10)	(-0.033 ± 0.053) V
3rd run	for SiPM 2.1: (132 ± 12) for SiPM 4.1: (111 ± 11)	for SiPM 2.1: (94 ± 10) for SiPM 4.1: (84 ± 10)	(-0.036 ± 0.049) V
for plastic scintillator detector 2			
	Counts within 200 mV-300 mV	Counts within 300 mV-500 mV	SiPM 2.2 - SiPM 4.2
1st run	for SiPM 2.2: (138 ± 12) for SiPM 4.2: (95 ± 10)	for SiPM 2.2: (90 ± 10) for SiPM 4.2: (105 ± 11)	(0.006 ± 0.046) V
2nd run	for SiPM 2.2: (129 ± 12) for SiPM 4.2: (97 ± 10)	for SiPM 2.2: (99 ± 10) for SiPM 4.2: (100 ± 10)	(0.008 ± 0.052) V
3rd run	for SiPM 2.2: (134 ± 12) for SiPM 4.2: (82 ± 10)	for SiPM 2.2: (90 ± 10) for SiPM 4.2: (103 ± 11)	(0.007 ± 0.052) V

Table 8: determination of counts in two different intervals and of mean amplitude difference (triggering signal - nontriggering signal)

All those histograms show similarities in their form: they are broadly and asymmetrically distributed, whereby we have more counts in the low amplitude region.
According to section 'Compton scattering and energy calibration', the gammas from the radium pointer are Compton scattered and thus lead, depending on their inital energy and scattering angle, to energy depositions in a range from 0 to the Compton edge.
The agglomeration of counts in the low energy region can be explained by the argument that there exists more pairings $[E_{photon}, \varphi]$ that lead to low energy depositions in the scintillator than to high energy depositions.
The abrupt edge of the SiPM 2.1 histograms at ≈ -0.2 V (see figures 24a - 24c) emerges because by imposing the threshold condition on the SiPM 2.1 signal, we intentionally exclude events between 0 mV and the threshold.
For the same reason, this abrupt edge appears also on the SiPM 2.2 histograms which we do not show here.
In contrast, the other signal does not underly this restrictions and can take arbitrary values between 0 mV and the maximum amplitude that can be output by the amplifier (800 mV - 900 mV).
Nevertheless, we do not expect too many counts with small amplitude values.

Another factor which shouldn't be ruled out is that there might also be a superposition with other low-energy decays (see background measurement).

The deviation in maximum count number is also non-surprising since the amplitude spectrum of the non-triggering channel is 'unfiltered', meaning it can take also values below the threshold, in contrast to the triggering channel. However since both SiPMs are attached to the same scintillator, the measured values are correlated, even though it can occur that for some events the difference in amplitude is considerable.

It turns out that the counts in the evaluated intervals (see table 8) remained the same throughout the runs within our range of uncertainty. This stability is in line with our expectations and is a good indicator for the reproducibility of our results.
Concerning the count numbers in these intervals, there are some further remarks to make.
First, the sample size for all runs (251 counts) was quite small and the agreement among separate runs would be higher if the measurement included more counts in total.
Secondly, the counts of SiPM 2.1/ 2.2 and SiPM 4.1/ 4.2 in the 200 - 300 mV interval differ on average by $\approx$ 40 counts. This 'gap' arises since we have many counts near the threshold (-202 mV) and the SiPM 2.1/2.2 values cannot be below the threshold, while the SiPM 4.1/4.2 can. Thus effectively every low amplitude signal for SiPM 2.1/2.2 is in the range (-300 mV, -200 mV]. In contrast, the "unfiltered" SiPM 4.1/4.2 values contain values below -200mV and those are therefore not included in the counts within the 200 - 300 mV interval.
Thirdly and finally, we would like to point out that unlike the other SiPMs, SiPM 4.2 has slightly more counts in the interval (-500 mV, -300 mV] than in the interval (-300 mV, -200 mV]. This indicates that the gain of SiPM 4.2 is slightly too high resulting in a shift of counts from the interval
(-300 mV, -200 mV] into the interval (-500 mV, -300 mV].

If we look at the mean differences in table 8, we find for all runs that the standard deviation exceeds the mean value. Thus the amplitude values are compatible with 0 mV, meaning that the two signals can be deemed equally high. This leads us to the conclusion that the gain of both SiPMs is well adjusted among themselves.
A deeper analysis shows that the gain of SiPM 2.1 and 4.1 match better while the gain of SiPM 4.2 is slightly too high: Due to event selection controlled by the trigger condition, we expect the trigger channel to have most of the time larger signals than the non-trigger channel.
Taking into account that the measured amplitudes are negative, the difference must then be slightly negative, which is the case for the SiPMs of plastic scintillator detector 1.
Nevertheless, we can speak of well-tuned SiPMs, even for plastic scintillator detector 2.

Subsequently to this test, we tied both plastic scintillator detectors together with a teflon band such that we obtained the arrangement seen in figure 25.

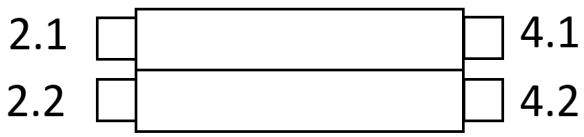

Figure 25: arrangement of the two double-SiPM plastic scintillator detectors
plastic scintillator dimensions: 100 mm x 41 mm x 10 mm
double SiPMs: two SiPMs connected in series
(in this case: ASD-NUV4S-P SiPMs from AdvanSiD as mentioned earlier)

The radium source was removed, while the choice of amplifier board (board 3), oscilloscope (WaveSurfer), light shielding (via the black box) and the dark currents (5 μA for all 4 SiPMs) were left unchanged. Our aim was to investigate the analogue signals of cosmics that propagate through both, the upper and lower detector and try to make statements about their trajectories. The assessment of the trajectories would have been more profound if we could have recorded all 4 analogue signals at a time.
Unfortunately the used oscilloscope didn't support the 'trend' record of more than 2 signals at a time. Therefore, we recorded the analogue signal of SiPM 2.1 and SiPM 2.2 in one measurement series and the analogue signal of SiPM 2.1 and SiPM 4.2 in another measurement series.

For each measurement series, we conducted 2 runs with 101 counts each, whereby we triggered on a different analogue signal in each run.
In order to seperate the cosmic events from noise or low-energetic events, we used a high threshold of -600 mV for all runs.

In figures 26a - 26d, we present the recorded amplitude values of each measurement run in a seperate event-order diagramm.

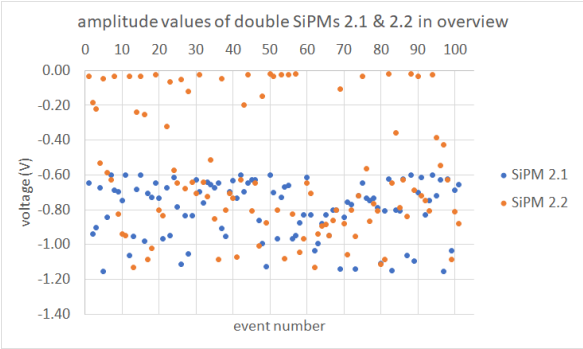

(a) trigger: SiPM 2.1

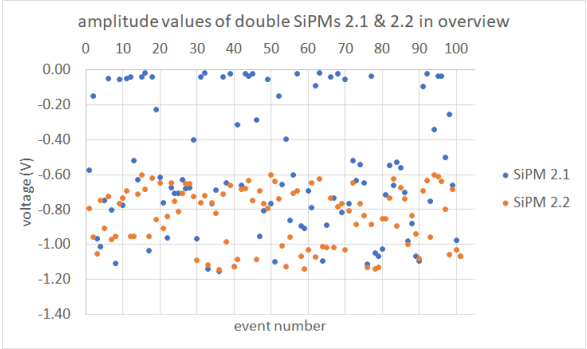

(b) trigger: SiPM 2.2

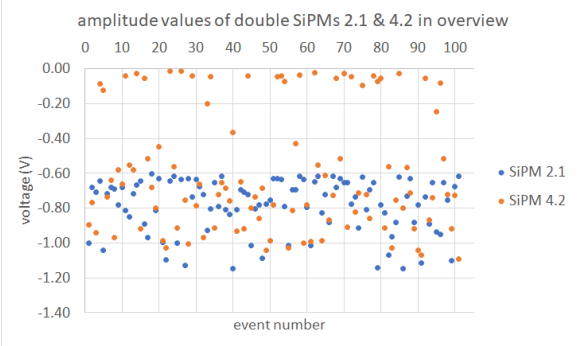

(c) trigger: SiPM 2.1

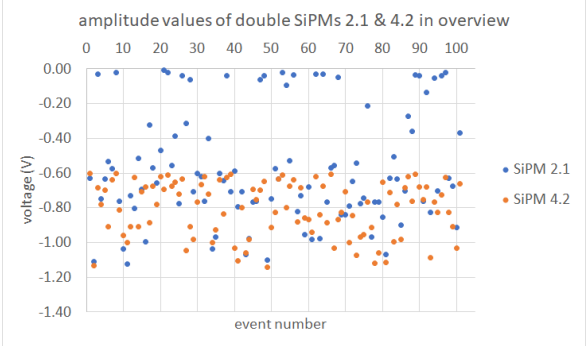

(d) trigger: SiPM 4.2

Figure 26: amplitude diagrams in occuring event-order

For a better event classification, we also look at the difference of simultaneous measuring points. Figures 27a - 27b show the difference of SiPM 2.1 amplitude - SiPM 2.2 amplitude, while figures 27c - 27d illustrate the difference SiPM 2.1 amplitude - SiPM 4.2 amplitude.

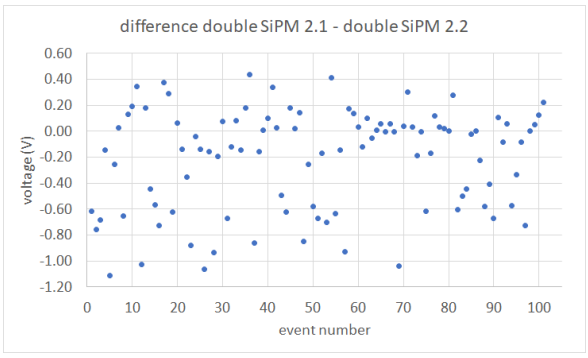

(a) trigger: SiPM 2.1

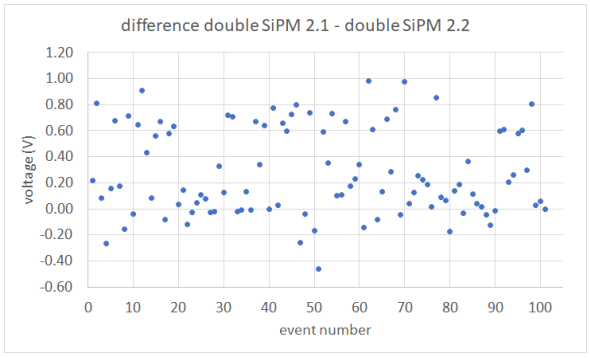

(b) trigger: SiPM 2.2

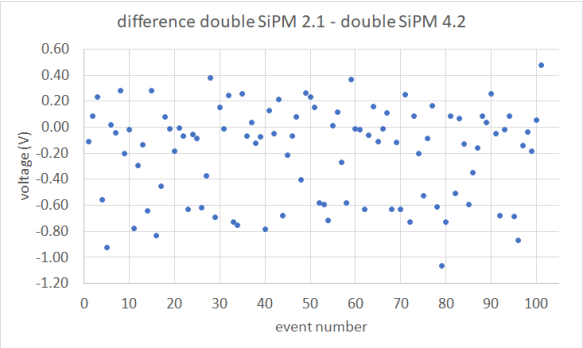

(c) trigger: SiPM 2.1

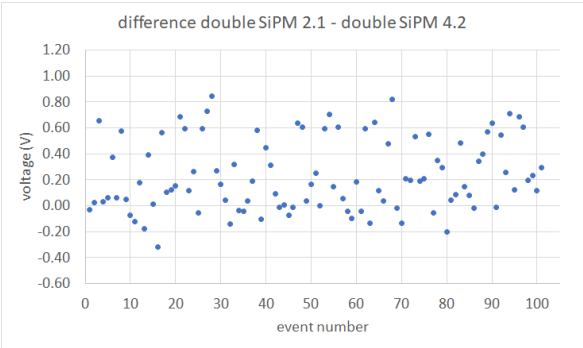

(d) trigger: SiPM 4.2

Figure 27: difference of analogue signal amplitudes

A first criteria necessary for the consistency of the measurement, is that all amplitudes of the trigger-channel must be greater or equal to -0.6 V. This condition is equivalent to the trigger condition and checking it with the graphs from above, we find it to be fullfilled.
One notices further that the magnitude of the trigger channel amplitude is greater than that of the non-trigger channel, which was expected according to arguments from earlier experiments.
Therefore if we trigger on SiPM 2.1, we expect figures 27a, 27c to have in majority negative differences. In contrast, if we choose the SiPM 2.2 or SiPM 4.2 signal as the triggering signal, we anticipate in majority positive differences. One observes that these expectations match the results.

With the knowledge of well-tuned detectors, we can draw more sophisticated conclusions from the event order diagrams. For example, cosmics with steep angle of incidence cover relatively long distances in both scintillators, yielding high amplitude signals in both of them (see figure 28a).
As a result, the difference between the recorded events is low, which enables an easy identification of these events with figures 27a - 27d.
Opposed to that, events with high difference in amplitudes arise if the triggering signal has high amplitude and the non-triggering signal has low amplitude. If we bring up again the argument that amplitude height is proportional to the covered path in the scintillator, we obtain depending on the trigger channel one of two situations (see figure 28b and 28c).

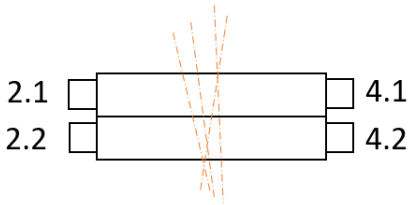

(a) trajectories for low-difference events
trigger: SiPM 2.1 or 2.2 or 4.2

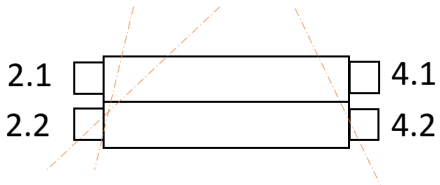

(b) trajectories for high-difference events
trigger: SiPM 2.1

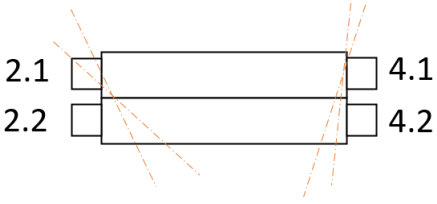

(c) trajectories for high-difference events
trigger: SiPM 2.2 or 4.2

Figure 28: cosmic trajectories through the setup corresponding to different amplitude differences and trigger channels

For completeness, we need to mention that with the information of only one signal per scintillator, we cannot make more precise statements where the cosmic has entered or propagated.
Assuming we had the measured amplitude values of all 4 SiPMs, then we could compare each two of them that are from the same scintillator and tell whether a cosmic has moved either closer at one or the other SiPM.
So if a certain cosmic has propagated e.g. centered through the upper scintillator we could identify that by the relation: amplitude SiPM 2.1 $\approx$ amplitude SiPM 4.1 .
On the other hand if the cosmic has propagated closer at SiPM 4.1 than at SiPM 2.1, we would know that due to the relation: amplitude SiPM 4.1 $>$ amplitude SiPM 2.1 .

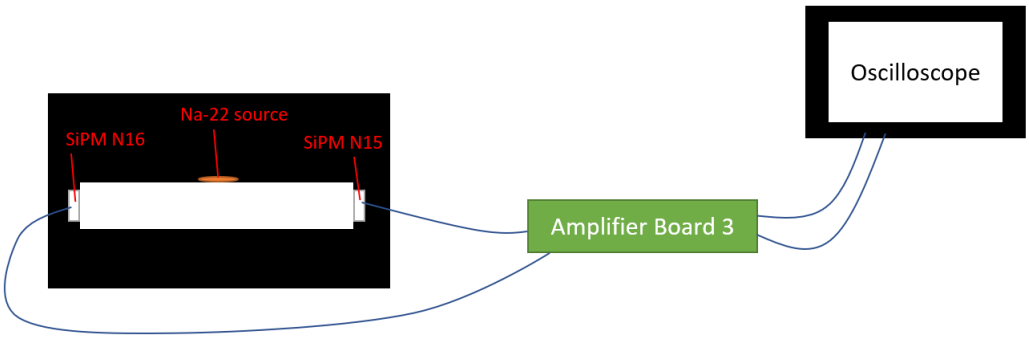

Figure 29: energy calibration of plastic scintillator detector with Na-22 source: used setup

In section 'Compton scattering and energy calibration', we identified with the Compton Edge formula (equation 2), the first Compton edge of Na-22 to be at $\approx$ 340 keV.
The aim of the following measurement is to use this value for an energy calibration of the plastic scintillator detector from figures 6a, 6b.
The setup in figure 29 shows how this is achieved: a Na-22 source is placed centered between the SiPMs N15 and N16 and the corresponding Na-22 spectrum is measured.
If the threshold is chosen properly, one should be able to identify the Compton Edge in the measured amplitude spectrum and assign it the energy value 340 keV. Assuming a linear correlation between the amplitude and the deposited energy, this completes the calibration.

Notice however that the tuned dark current and therefore the overvoltage have a significant influence on the measured amplitudes and thus also on the position of the Compton edge.
In order to quantify the change of the proportionality, three runs with 1 μA, 2 μA and 5 μA dark current were conducted. For all three calibration runs, a trigger threshold of about -50 mV was imposed on the analogue signal of SiPM N15.

SiPM N15 and SiPM N16 were connected to the WaveRunner oscilloscope via board 3, with connections made according to table 9.

SiPM name	amplifier board channel	oscilloscope channel
SiPM N15	CH 1	CH 1
SiPM N16	CH 2	CH 2

Table 9: connections for the Na-22 energy calibration

The recorded histograms of all three runs are depicted in figures 30a - 30c.

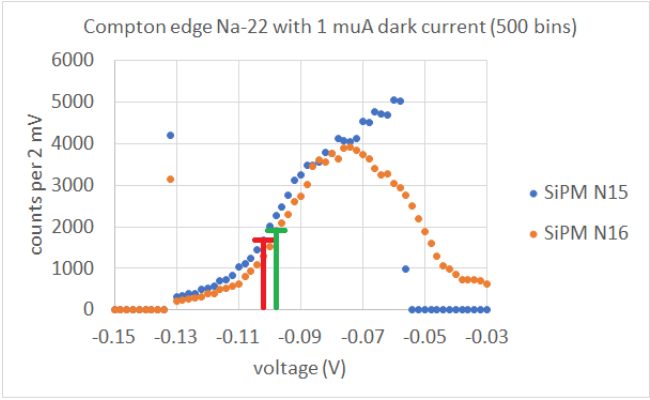

(a) vertical scale: 20mV/div

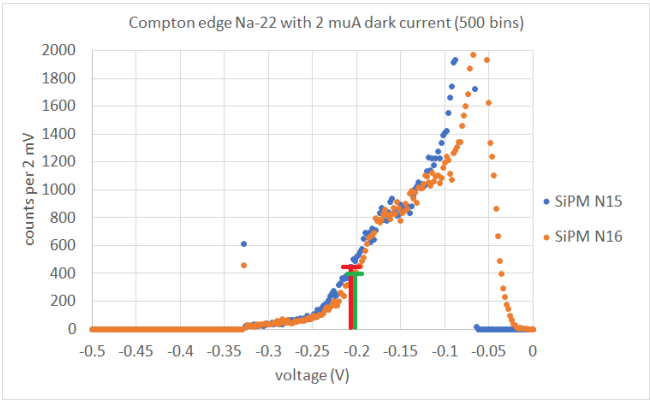

(b) vertical scale: 50mV/div

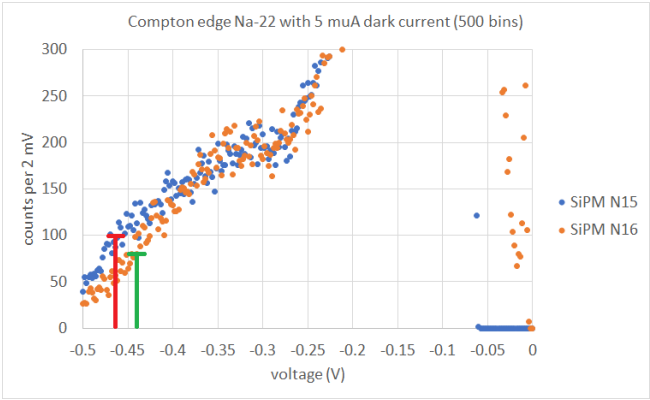

(c) vertical scale: 100mV/div

Figure 30: Na-22 spectrum recorded with the plastic scintillator to be calibrated at three different dark currents

	1 μA-run	2 μA-run	5 μA-run
SiPM N15	Compton edge at: (-102 ± 30) mV event rate: (116.36 ± 0.14) counts/s	Compton edge at: (-208 ± 30) mV event rate: (126.52 ± 0.16) counts/s	Compton edge at: (-462 ± 30) mV event rate: (132.15 ± 0.18) counts/s
SiPM N16	Compton edge at: (-98 ± 30) mV event rate: (116.36 ± 0.14) counts/s	Compton edge at: (-202 ± 30) mV event rate: (126.52 ± 0.16) counts/s	Compton edge at: (-442 ± 30) mV event rate: (132.15 ± 0.18) counts/s

Table 10: position of first Na-22 Compton edge and corresponding event rate
For the rates, we assumed a measuring time uncertainty of 1 s, while the recorded counts are assumed to have no deviations.

In addition to the measurement itself, the event rate for ≈ 100 000 counts was determined, which is listed in table 10, together with the Compton edge position.
Reading off the Compton edge from the histograms is an ambiguous task, since the edge is smeared out as mentioned earlier. The edge positions in table 10 were determined by first searching for a kink in an imaginary line that 'fits' the data points ('Compton knee').
Going to higher voltages from there, we next looked for the voltage bin, where the count number drops to zero. Then, we identified the Compton Edge position as the voltage value in between the two points, that has half the counts of the kink.

Since the amplitudes increase with growing dark current (overvoltage), we expect that the position of the Compton edge is shifted to regions with higher voltage. In parallel, we anticipate that the measuring time decreases or rather that the rates increase when we change to higher dark currents. This can be justified by the fact that measured signals are due to a higher gain more likely to be above the threshold. Looking at the results in table 10, we find that both predictions are very well satisfied.

Interestingly, it turned out during the measurement that the Compton edge is much easier to identify if the measuring scale on the oscilloscope is well chosen. For example, the 1 μA-run was first conducted with a scale of 50 mV/div but the kink wasn't clearly visible for both signals at a time.
By reducing the vertical scale to 20 mV/div, we shifted the dynamic range (meaning here the range of amplitudes that can be reasonable processed excluding overflow or underflow) towards lower amplitudes. Therefore we obtained a better resolution of the Compton edge in the histograms.
Simultaneously this shift, however, caused that events with amplitudes ≥ 130 mV where not fully depicted on the oscilloscope screen and were stored as overflow events (see the blue and orange point at ≈ 130 mV in figure 30a). Since the goal of this measurement was to find the voltage value at which the Compton edge occurs, it does not bother us that we do not have more precise information about the events beyond the -130 mV range.

Experimenting reveals as well that a well-chosen binwidth is crucial for the visibility of the Compton edges. If the bin width is chosen too large, there will be only a few bins with relatively high count numbers, so that no large structure can be seen.
On the other hand, given too small bin width, we have many bins with relatively low count numbers, such that the histogram is too flat. Again, we cannot extract meaningful information from the histogram structure.
In extrem cases it occurs that there form 'gaps', i.e. histogram values with 0 counts that lie in-between two non-zero histogram values.
In the measurement runs presented in figures 30a - 30c, a binwidth of $\frac{100\ mV/div \cdot 10\ div}{500\ bins} = 2$ mV/bin was used. Comparing the dark currents and the corresponding Compton edge positions, we can furthermore conclude that the shift is realized almost by a constant factor.

Attempts for measuring Compton edges of other available sources to directly verify the previous found voltage-energy calibration were in most cases far from successful. The main reason for this was probably that we didn't have a second, proper source available for which this calibration is a manageable task. Either the edge position was presumed outside the maximum accessible voltage or in a low voltage region where noise covers it. Moreover, the histogram shape depended, as in the previous measurement, significantly on the dynamic range (i.e. the vertical scale setting) and the chosen number of total bins.

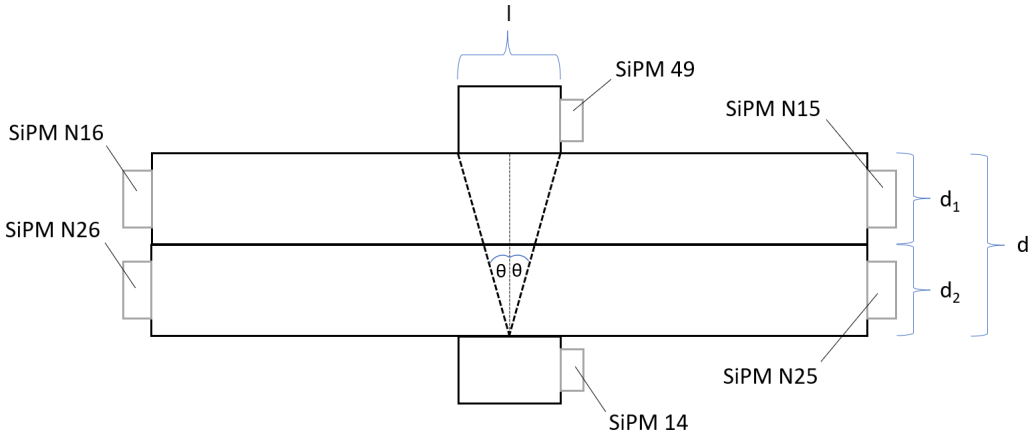

Figure 31: scheme of a setup used for an alternative energy calibration approach with cosmics
All of the 6 SiPMs depicted in this figure were 4 x 4 mm^2 ASD-NUV4S-P SiPMs from AdvanSiD with a pixel size of 40 μm x 40 μm.

So for a check of the calibration, a completely new approach was chosen: we put under the detectors to be calibrated a second pair of plastic-scintillator detectors and sandwiched them between two test detectors (see figure 31).
The detectors were arranged in the way depicted in figure 31: the plastic scintillator detector we wanted to calibrate carried SiPM N16 and N15 and the second detector below used SiPM N26 and N25.
The test detector on the top had SiPM 49 attached and the lower test detector carried SiPM 14.

The cuboid test detectors sandwiching from below and above had equal size with
length l=50 mm, width b=12 mm and thickness d_i=5 mm (where i=1,2).
The plastic scintillator detector to be calibrated and the plastic scintillator detector with SiPMs N26 and N25, on the other hand, had the dimensions: 101 mm x 16 mm x 5 mm.

The digital signals of the test detectors were adjusted to thresholds of -400 mV and then connected via an AND logic to form the triggering signal. The detectors were chosen according to demands in their size: on the one hand they should be small to have mainly vertically incident cosmics trigger them, on the other hand they shouldn't be too small such that we have a reasonable event rate.

The second plastic scintillator detector with SiPM N26 and N25 served to decrease the maximum possible angle, θ_{max}, entering into our records (see angle θ in figure 31). In this way, the range of angles of incidence possible for the recorded events was reduced to steeper inciding trajectories.
The restriction to steep inciding trajectories will serve to increase the accuracy of our calibration, as will be clarified at the end of the discussion.

Table 11 associates the SiPMs with their respective board channel and their adjusted dark currents.

	first run		second run	
	dark current	board channel	dark current	board channel
SiPM 49	4.23 μA	1	4.23 μA	1
SiPM 14	4.21 μA	2	4.21 μA	2
SiPM N16	2.01 μA	10	2.01 μA	10
SiPM N15	2.16 μA	9	2.16 μA	9
SiPM N26	2.04 μA	3	-	-
SiPM N25	-	-	2.05 μA	3

Table 11: settings for the energy calibration approach with cosmics

For the calibration, we measured the amplitude spectrum of SiPM N16, N15, N26 and N25 using the coincidence of SiPM 49 and 14 as a trigger.
The used oscilloscope has a limit of 4 ingoing signals at at time, thus the amplitudes were recorded in

two measurement runs.
In the first run, the amplitudes of SiPM N16, N15 and N26 were measured and in the second run, the amplitudes of SiPM N16, N15 and N25 were recorded.
In the following table, the SiPMs of the 2 middle detectors are assigned to their mean amplitudes including standard deviation.

	first run	second run
	mean amplitude ± std	mean amplitude ± std
SiPM N16	(-572.6 ± 118.4) mV	(-566.5 ± 120.3) mV
SiPM N15	(-673.5 ± 93.9) mV	(-665.3 ± 87.6) mV
SiPM N26	(-544.3 ± 121.9) mV	(– ± –) mV
SiPM N25	(– ± –) mV	(-517.1 ± 113.5) mV

Table 12: measured mean amplitude including standard deviation for the energy calibration approach with cosmics

Provided with these mean amplitudes, we can accomplish the calibration by the following additional considerations:
The Bethe-Bloch formula for plastic scintillators predicts that cosmics are in good approximation MIPs (Minimal Ionizing Particles), meaning that their kinetic energies are in a range where the energy loss per length, -$\frac{dE}{dx}(E_{kin})$, is not only minimal but also to very good approximation constant. [15]
This enables us to establish an easier relation between amplitude, A, and total energy loss, -dE:

$$-dE(E_{kin}) = -\frac{dE}{dx}(E_{kin}) \cdot \Delta x \stackrel{!}{=} \alpha^{-1} \cdot A \longrightarrow A = -\alpha \cdot \frac{dE}{dx}(E_{kin}) \cdot \Delta x \tag{3}$$

Note that we avoided here the integration with respect to the covered path, dx, by exploiting the fact that $-\frac{dE}{dx}(E_{kin})$=2.0 MeV/cm=const. [15]
Therefore only the total covered distance, Δx, is relevant.
α represents here the proportionality constant that links both quantities.

In particular, this equation should hold for the mean amplitude $\overline{A}$ and the mean total energy loss -$\overline{dE}$:
Whereas the mean amplitude can be obtained by a measurement, the mean total energy loss (or mean total energy deposited in the scintillator) can be calculated as indicated above:
-$\overline{dE}$=$-\frac{dE}{dx}(E_{kin}) \cdot \overline{\Delta x}$ with the mean covered distance $\overline{\Delta x}$.

The mean covered distance can now be obtained by e.g. a Monte-Carlo simulation.
For this thesis we will however choose a simpler approach.
Assuming that cosmics propagate in straight lines and isotropically, we find by analysing the geometry of the setup that there exists a maximum angle, θ_{max}, under which a cosmic can propagate through the setup such that it is recorded in the data.
This angle amounts to

$$\theta_{max} = \arctan\left(\frac{0.5 \cdot l}{d}\right) = 68.2^\circ \quad or \quad 1.19029$$

In addition, one can convince oneself that events with steep angles of incidence are more likely to be recorded than events with flat angles of incidence. The reason for this is that the former have more possible trajectories that lead to a trigger.
Thus we modelled a Gaussian distribution, $p(\theta)$, with μ=0 and σ=15°=0.2617 to weigh the possible covered distances, $s(\theta) = \frac{d}{\cos(\theta)}$, according to their frequency.
Then the averaged covered path is

$$\Delta x = \int_0^{\theta_{max}} p(\theta) \cdot s(\theta) d\theta$$

Of course, $p(\theta)$ must first be normalized to 1 within the range $[0, \theta_{max}]$, yielding a normalization constant N=1/0.327991 .

Plugging all the information in, we arrive at the following mean covered distance within the detector to be calibrated:

$$\Delta x = \int_0^{\theta_{max}} N \cdot e^{-\frac{\theta^2}{2\cdot\sigma^2}} \cdot \frac{d_1}{\cos(\theta)} d\theta = 5.19\ mm$$

The measured mean amplitudes from table 12 and equation 3, finally, enables the calculation of the proportionality constant α:

$$\alpha = -\frac{\overline{A}}{\overline{dE}} = -\frac{\overline{A}}{\frac{dE}{dx}(E_{kin}) \cdot \overline{\Delta x}} = -\frac{\overline{A}}{2000\ keV/cm \cdot 0.519\ cm} \tag{4}$$

The resulting values for α including their errors are collected in table 13:

	first run	second run
	α ± error	α ± error
SiPM N16	(-0.55 ± 0.12) mV/keV	(-0.55 ± 0.12) mV/keV
SiPM N15	(-0.65 ± 0.10) mV/keV	(-0.64 ± 0.10) mV/keV

Table 13: calculated values for the proportionality constant α

In order to determine the errors, error propagation was applied where we assumed that
-) ΔA equals the standard deviation of the amplitudes
-) the read-off error of the constant $\frac{dE}{dx}$ value is $\Delta\frac{dE}{dx}$=100 keV/cm
-) errors in the mean covered distance arise since our considerations are a 2-dimensional idealization, but particles can in practice also incide at an angle. Assuming that such an angle has a maximum value of $15°$, we conclude $\Delta\overline{x}$=0.02 cm.

Concerning the uncertainty of these results, there must be stated that the better we can exclude flat inciding trajectories, the smaller the ΔA contribution within the error propagation becomes.

If the relation of amplitude to total energy loss, i.e. α, is the same for the Na-22 calibration and this verification experiment with cosmics, then the calibration of the detector can be deemed successful.
Recall that the Compton edge for Na-22 was found in the 2 μA run at -208 mV (SiPM N15) respectively at -202 mV (SiPM N16).
Equation 4 can then be modified to $\alpha = -\frac{A_C}{E_C}$, using the literature value for the Compton edge of Na-22: E_C=340 keV. This gives the following α values for the detector to be calibrated:

for SiPM N15: $\alpha = -\frac{A_C}{E_C} = -\frac{208\ mV}{340\ keV} = -0.61\ mV/keV$

for SiPM N16: $\alpha = -\frac{A_C}{E_C} = -\frac{202\ mV}{340\ keV} = -0.59\ mV/keV$

Similarly as above, the uncertainty of this result is determined by error propagation under the following assumptions:
-) E_C has no error, since it was obtained by calculation
-) since identifying the exact location of the Compton edge is a challenging task, we indicate a rather high value for the amplitude uncertainty, ΔA_C=30 mV.

Including the error, the result reads:

SiPM N15	SiPM N16
α=(-0.61 ± 0.09) mV/keV	α=(-0.59 ± 0.09) mV/keV

Table 14: calculated values for α in the 2 μA run of the Na-22 energy calibration including uncertainties

We find that the determined α-values all lie within their respective ± 1σ-region, so the calibration was successful.

7 Prototype 1 experiments

The series of Prototype 1 measurements starts with a voltage amplitude measurement on both SiPMs in presence of a Sr-90 source in the middle of the casing. In the following, we refer to measurements with sources at this position as 'centered measurements'.
For this centered measurement, we arranged the setup such that the analogue signal corresponding to SiPM 7 was measured on oscilloscope channel CH1 after being amplified at board channel 1 on amplifier board 3. At the same time, the analogue signal of SiPM 6 was measured on oscilloscope channel CH2 with amplification at board channel 2.
The trigger was set on CH2, (the analogue signal of SiPM 6), and adjusted in three runs to three different thresholds: -30 mV, -50 mV and -70 mV.

Figure 32 shows the setup of Sr-90 centered measurements and figure 33a - 33c depicts the plots created from measured histograms including measuring time.

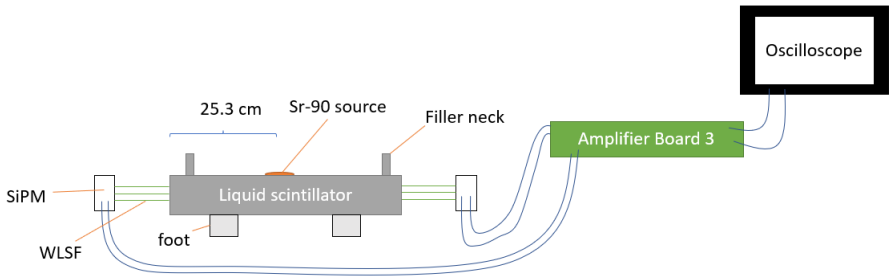

Figure 32: scheme of Prototype 1 experiment with centered Sr-90 source.

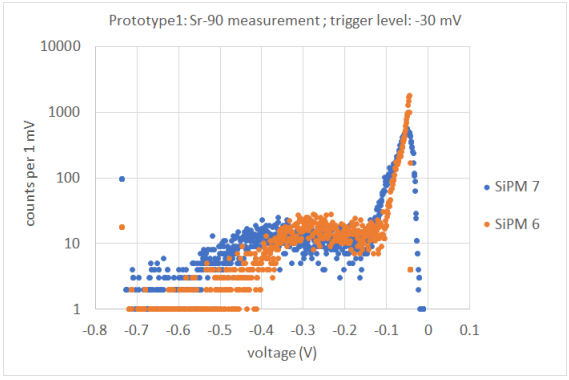

(a) measuring time: 33min

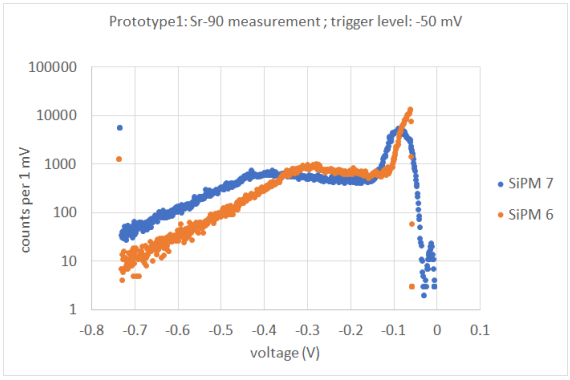

(b) measuring time: 22h 26min

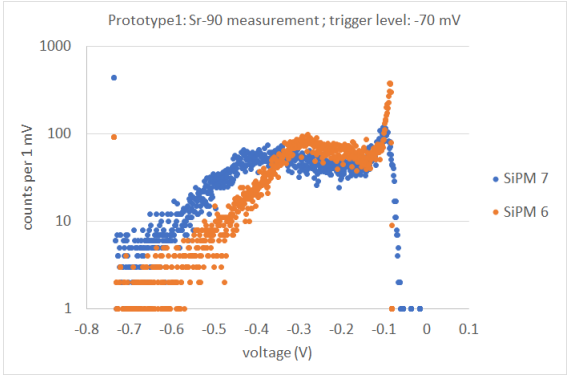

(c) measuring time: 114 min

Figure 33: Prototype 1 histograms generated from measurements with centered Sr-90 source at different threshold levels

Reproducability of these results was checked in repeated measurements but with a much lower data sample and they were in good agreement.

It turns out that changing the trigger does not influence the form of the spectrum. If we go from right to left, the count number rises from 0 at 0 mV to a maximum value around the adjusted threshold level. Afterwards it declines until it reaches a plateau with 200 - 300 mV width, followed by another drop. Further we can conclude from these experiments that SiPM 7 has a higher internal gain than SiPM 6.

Next, Prototype 1 was used to perform an amplitude measurement for cosmics. The oscilloscope channels and board channels were connected with the SiPMs in accordance with the previous measurement. We triggered on each of both SiPMs twice with a trigger threshold of -130 mV. The dark currents of SiPM 7 and SiPM 6 were set to 5 μA.
Each of this four runs contains 1000 amplitude values per SiPM, i.e. 1000 events for SiPM 6 and 1000 events for SiPM 7. For each run and SiPM, the corresponding mean amplitude including standard deviation was calculated and a histogram was created.

Table 15 lists the mean $\pm$ standard deviation results for all 4 runs as well as the mean difference of triggering signal - non-triggering signal:

triggering signal	SiPM 7	SiPM 6
1st run	mean amplitude SiPM 7: (-0.272 $\pm$ 0.096) V mean amplitude SiPM 6: (-0.261 $\pm$ 0.094) V mean difference: (-0.01 $\pm$ 0.040) V	mean amplitude SiPM 7: (-0.259 $\pm$ 0.093) V mean amplitude SiPM 6: (-0.259 $\pm$ 0.091) V mean difference: (0 $\pm$ 0.040) V
2nd run	mean amplitude SiPM 7: (-0.254 $\pm$ 0.088) V mean amplitude SiPM 6: (-0.248 $\pm$ 0.088) V mean difference: (-0.005 $\pm$ 0.038) V	mean amplitude SiPM 7: (-0.261 $\pm$ 0.096) V mean amplitude SiPM 6: (-0.257 $\pm$ 0.094) V mean difference: (0.004 $\pm$ 0.038) V

Table 15: mean amplitudes and mean differences calculated from the Prototype 1 cosmic measurement runs

The corresponding histograms using 25 bins are shown in figures 34a - 34d.

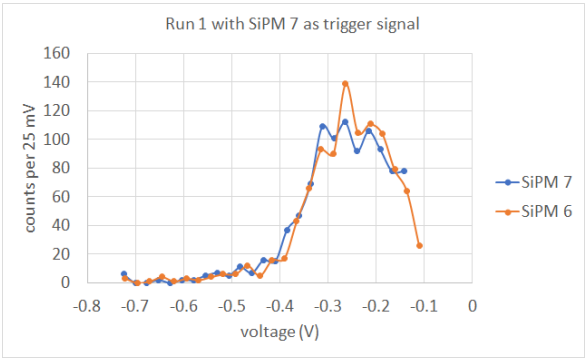

(a)

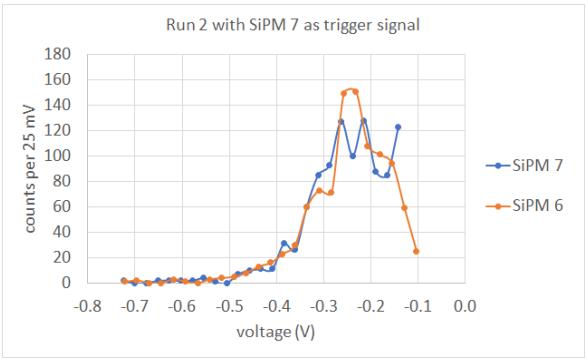

(b)

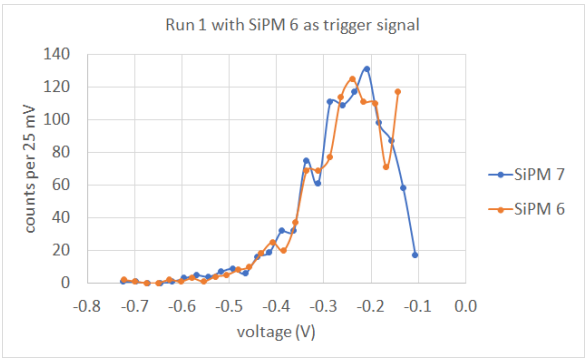

(c)

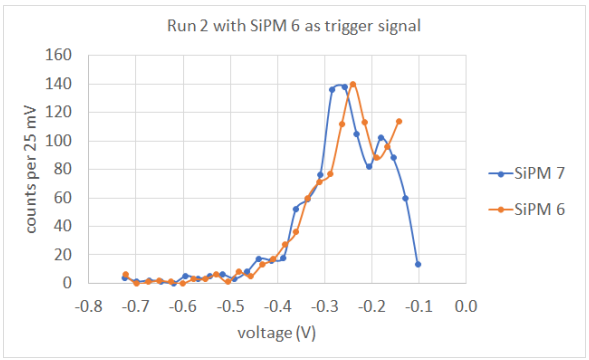

(d)

Figure 34: Prototype 1 histograms generated from cosmics measurements using different trigger channels; threshold at -130 mV

Under ideal conditions (absence of systematic errors, isotropic cosmics distribution and ideal properties of SiPMs), we assume that the averages of both SiPMs should approach asymptotically to each other for increasing count number. Idealizing cosmic propagation as isotropic, there exists a broad distribution of possible path lengths and thus also for the energy depositions.
Therefore we expect that the standard deviations should be high compared to the mean values.
At the same time this should imply that the mean difference between the signals should be distributed around 0 mV.
Looking at the table, one finds many of those expectations fulfilled in good approximation:
all mean amplitude values are close together.

However, all mean values of SiPM 7 are slightly higher than of SiPM 6, which supports the previous finding that SiPM 7 has a slightly higher internal gain than SiPM 6.
This manifests also in the respective sign of the mean differences.
Additionally, the evaluation shows that all mean difference values fluctuate around 0 V.

For the next experiment, we prepared two test detectors of the type we had in the previous chapter (2 scintillators with 2 double SiPMs respectively for readout) and attached them to the center of the aluminium casing with tape; one on the top surface and one on the bottom surface (see figures 35a, 35b).

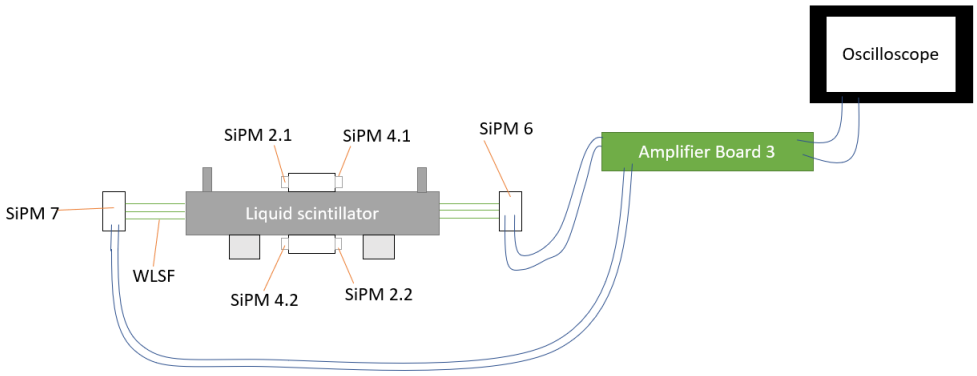

(a) frontside view on the setup used in the efficiency preparation measurement.
Notice that the cables from the test detector SiPMs to amplifier board 3 were omitted.

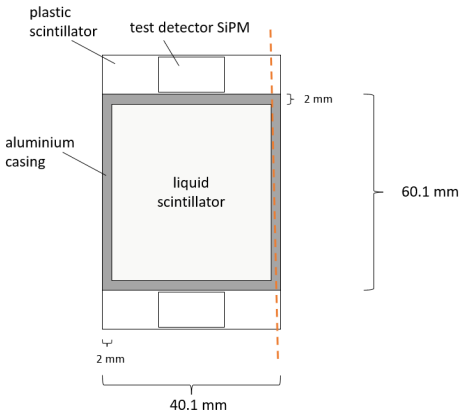

(b) side view on the setup used in the efficiency preparation measurement.
The dotted, orange line represents a possible cosmic trajectory that leads to a recorded background event at SiPM 7 and SiPM 6

Figure 35: preparation for efficiency measurement with Prototype 1: setup from different perspectives

The detectors on the top surface carried SiPM 2.1 and 4.1 and the bottom detectors used the SiPMs 4.2 and 2.2.
As preparation for the efficiency measurements, we measured in a sequence of measurements the analogue signal of SiPM 6 on CH2 and the analogue signal of one of the four test SiPM readouts at CH4. Afterwards an analogous sequence of measurements was conducted with SiPM 7 being measured at CH2 and one of the four test SiPM readouts being measured at CH4.
For signal amplification, amplifier board 3 was used with the SiPMs 6/7 being amplified at board channel 1 and the test SiPMs being amplified at board channel 2.

The trigger for all those measurements was set on CH4 with a threshold of -600 mV.
While the dark currents of SiPM 6 and 7 were adjusted to 7 μA, the test SiPMs were operated with bias voltage corresponding to 5 μA dark current.

Table 16 depicts the measured mean $\pm$ standard deviation results for both measurement sequences.

detector pairing	mean ± std.	detector pairing	mean ± std.
SiPM 6 & SiPM 2.1	mean amplitude SiPM 6: (-0.195 ± 0.186) V mean amplitude SiPM 2.1: (-0.781 ± 0.155) V	SiPM 7 & SiPM 2.1	mean amplitude SiPM 7: (-0.208 ± 0.196) V mean amplitude SiPM 2.1: (-0.774 ± 0.140) V
SiPM 6 & SiPM 4.1	mean amplitude SiPM 6: (-0.190 ± 0.172) V mean amplitude SiPM 4.1: (-0.764 ± 0.141) V	SiPM 7 & SiPM 4.1	mean amplitude SiPM 7: (-0.213 ± 0.189) V mean amplitude SiPM 4.1: (-0.780 ± 0.144) V
SiPM 6 & SiPM 4.2	mean amplitude SiPM 6: (-0.180 ± 0.179) V mean amplitude SiPM 4.2: (-0.804 ± 0.158) V	SiPM 7 & SiPM 4.2	mean amplitude SiPM 7: (-0.209 ± 0.192) V mean amplitude SiPM 4.2: (-0.799 ± 0.152) V
SiPM 6 & SiPM 2.2	mean amplitude SiPM 6: (-0.203 ± 0.182) V mean amplitude SiPM 2.2: (-0.807 ± 0.158) V	SiPM 7 & SiPM 2.2	mean amplitude SiPM 7: (-0.210 ± 0.188) V mean amplitude SiPM 2.2: (-0.798 ± 0.160) V

Table 16: mean amplitudes ± standard deviations of all pairings consisting of a Prototype 1 SiPM and a test SiPM

The corresponding event-order diagrams are shown in the following collection of figures.

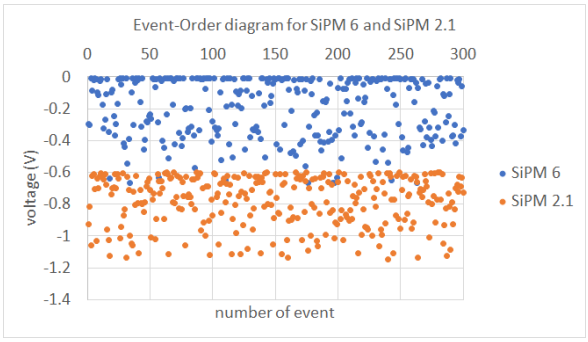

(a)

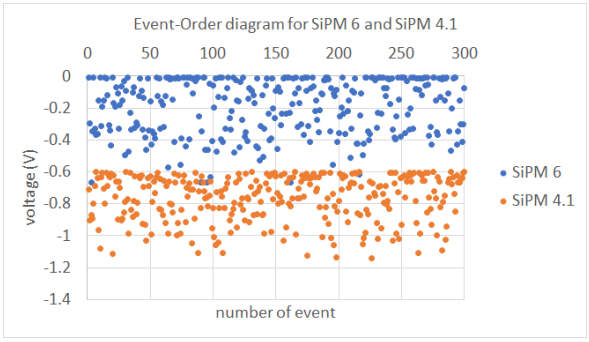

(b)

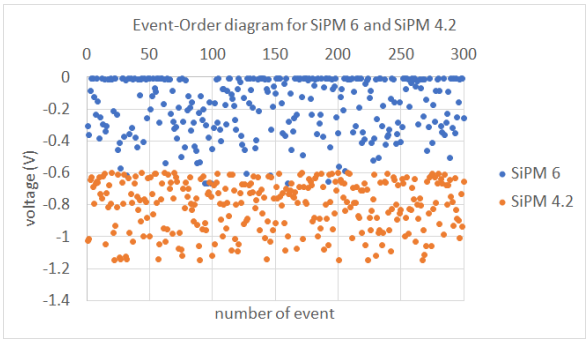

(c)

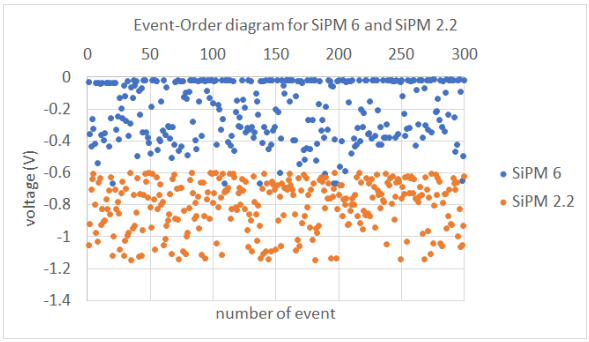

(d)

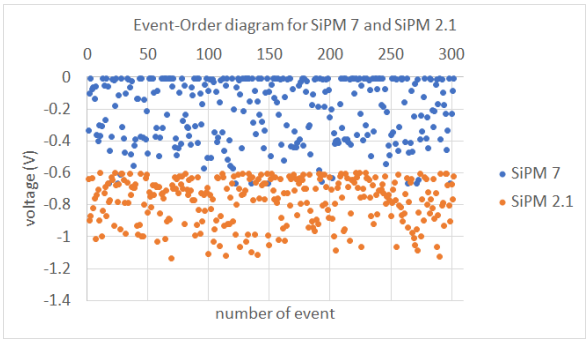

(e)

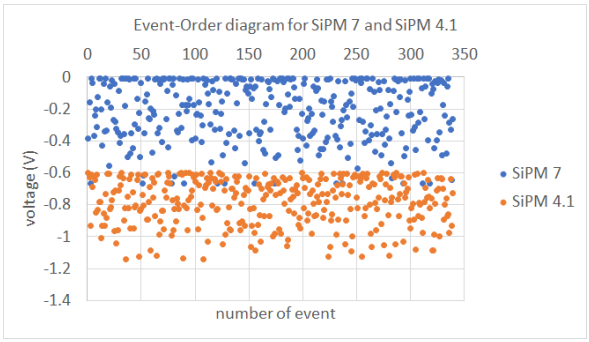

(f)

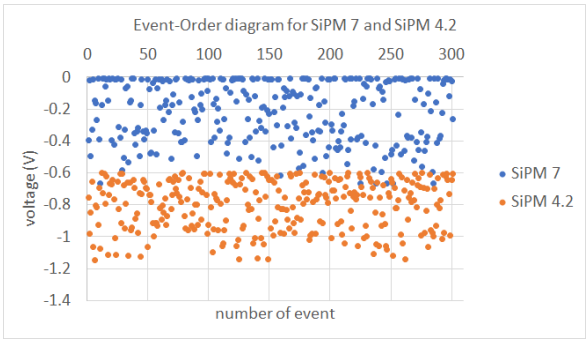

(g)

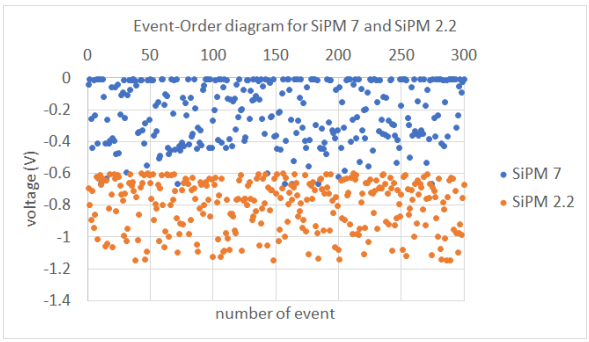

(h)

Figure 36: preparation for efficiency measurement with Prototype 1: histograms for all possible pairs of SiPM 7 with test detector readouts as well as all possible pairs of SiPM 6 with test detector readouts

The main goal of these measurements was reached, since we could show that all measurements yielded plausible results: On the one hand, the threshold was set quite high, filtering away low amplitude events. On the other hand, the standard deviation of both signals is quite high compared to the mean amplitude which is backed up by the nearly fulfilled isotropy of cosmic radiation and their broad distribution of energy deposition.

Based on the arrangement of test detectors to Prototype 1, we expect 10% of the cosmics to propagate through the scintillators but not through the Prototype's liquid scintillator.
Instead, the cosmics will move through one of the two, 2 mm thick aluminum walls.
Additional events with low amplitudes for the Prototype 1 readouts will be recorded due to cosmic trajectories with such flat angles of incidence, that they do not pass through any Prototype 1 part, at all. One can easily identify them in the event order diagrams (see figures 36a - 36h) as those events that assign a 0 mV amplitude to SiPM 7/6. Those events do not allow to compare gain or light collection of a simultaneously measured detector pair and thus they are irrelevant for such an analysis.

Looking at the event-order diagrams, one notices that despite of a much higher dark current, the SiPMs of the Prototype 1 detector yield in majority by far smaller signals than the test detector SiPMs.
Interpretating the measured signal heights reveals two competing effects:
The test scintillator generates less scintillation light as Prototype 1 because Prototype 1 is thicker such that more particle energy can be deposited in there.
However, the light collection of Prototype 1 is lower since only a fraction of the produced light is transferred into the fibres and from the fibres to the SiPMs.

An even more important finding, however, is that based on our results we are able to reliably read out a relatively large volume with only 16 wavelength shifting fibers and 1 SiPM per side.

Equipped with these informations from the preparation, an efficiency measurement for Prototype 1 was started. The setup from the preparation experiment (see figure 35a) was slightly modified by replacing amplifier board 3 with amplifier board 1 to provide the required number of board channels.
Discriminator thresholds, dark currents and board channel connections were adjusted and chosen according to the following table:

	dark current	discriminator threshold	board channel
SiPM 2.1:	-7.09 μA	-400 mV	CH1
SiPM 4.1:	-7.10 μA	-350 mV	CH2
SiPM 4.2:	-7.05 μA	-350 mV	CH3
SiPM 2.2:	-7.07 μA	-300 mV	CH4
SiPM 7:	-6.97 μA	-	CH9
SiPM 6:	-7.06 μA	-	CH10

Table 17: adjusted dark currents, discriminator threshold settings and choice of amplifier board channels for the Prototype 1 efficiency measurement

The trigger of this measurement was created from two AND signals (#1, #2) that were fed into another AND-logic.
One of those AND signals (#1) was formed from the digital signals of SiPM 2.1 and 4.1 and the other AND signal (#2) originated from the digital signals of SiPM 4.2 and 2.2.
By feeding this two logic signals into another AND, we select only signals which pass through both scintillators of the test detector.
We measured the amplitudes of the SiPM 6 and SiPM 7 signals and determined from the corresponding histograms the efficiency of each of the two Prototype 1 detector readouts.

Important quantities for both Prototype 1 readouts measured in 3 runs are summarized in table 18 .

first run	mean amplitude SiPM 7 ± std.: (-0.629 ± 0.122) V mean amplitude SiPM 6 ± std.: (-0.575 ± 0.124) V mean difference ± std.: (-0.053 ± 0.035) V counts: 1000
second run	mean amplitude SiPM 7 ± std.: (-0.634 ± 0.125) V mean amplitude SiPM 6 ± std.: (-0.578 ± 0.126) V mean difference ± std.: (-0.055 ± 0.034) V counts: 1000
third run	mean amplitude SiPM 7 ± std.: (-0.623 ± 0.126) V mean amplitude SiPM 6 ± std.: (-0.573 ± 0.128) V mean difference ± std.: (-0.050 ± 0.034) V counts: 1000

Table 18: relevant quantities of the Prototype 1 efficiency measurement, collected in 3 runs

The following figure 37 depicts the histograms of all runs in centered position in one graph:

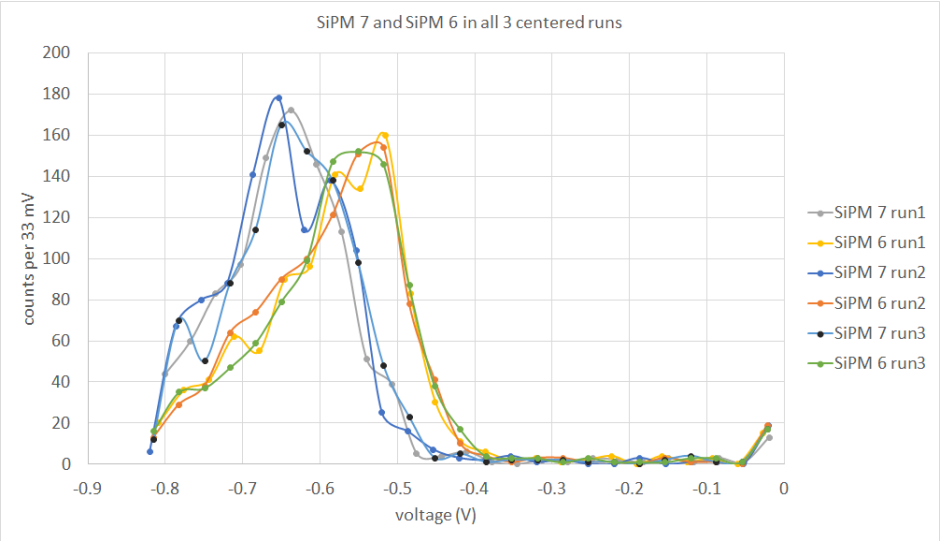

Figure 37: Prototype 1 histograms of 3 centered runs plotted in one graph

The used measurement mode 'Trend' preserved the event order of the counts as exemplarily shown for the first and second run in the figures 38a - 38b.
For reasons of clearliness in the discussion, we also add the difference SiPM 7 amplitude - SiPM 6 amplitude (see figures 39a - 39b).

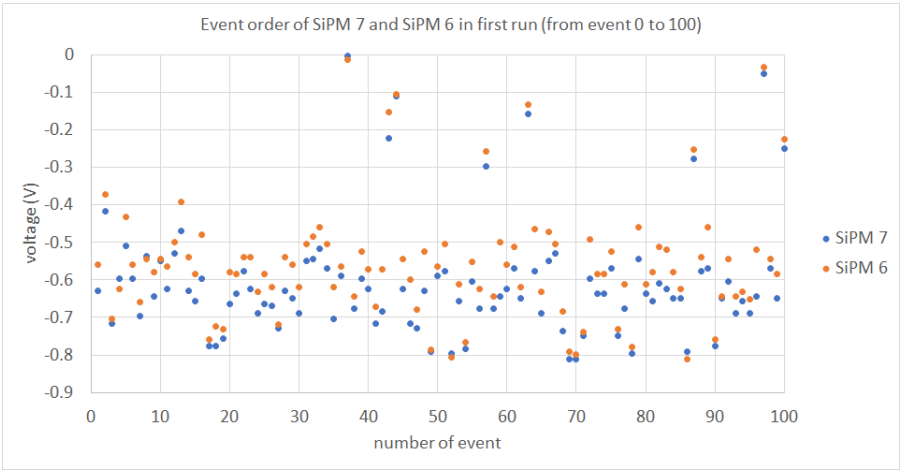

(a)

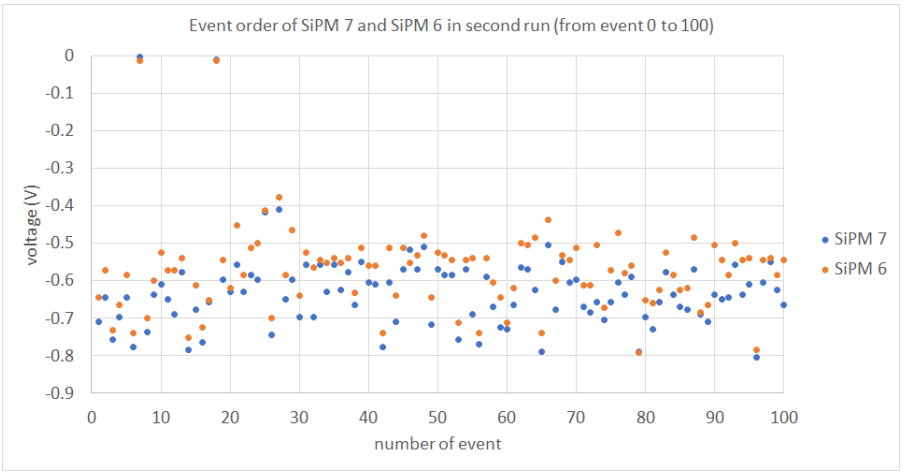

(b)

Figure 38: Prototype 1 efficiency measurement: event-order plots for the first two centered runs

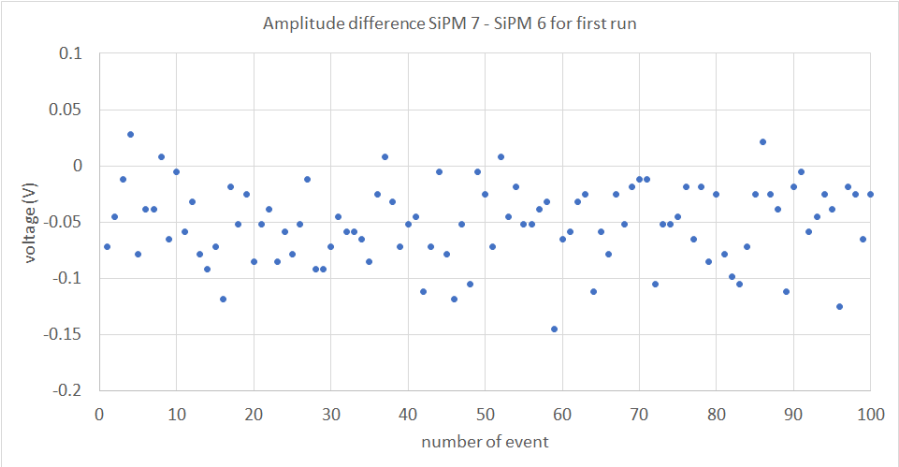

(a)

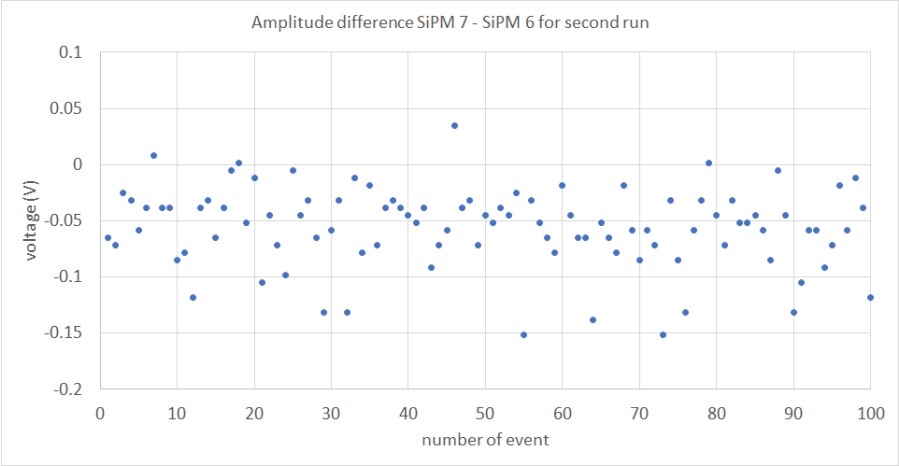

(b)

Figure 39: Prototype 1 efficiency measurement: difference plots for the first two centered runs

Analysing the histograms, we find on the one hand reproducability fulfilled and on the other hand a good matching with our expectations.
Due to the discriminator thresholds imposed via the trigger (test detectors), we also filter out low energy events in the Prototype 1 detector and thus there should only be quite few counts below -400 mV.
Those counts that are below this value gather mostly in the region below -100 mV. These events are associated to the background events: these are the events, where both test detectors detected a charged particle, but the Prototype SiPMs didn't.

Since the test detectors were located in the centered position and measuring points are only recorded if a cosmic particle has propagated through both test detectors, production of scintillation light will in majority take place in the small scattering volume in between the test detectors.
From that volume, the fraction of light that enters the fibre must cover approximately equal distances to the SiPMs. It is assumed that the portion of light that scatters out of the fibre again is proportional to the covered distance, so we predict equal light fractions at the SiPMs and further equal voltage amplitudes.

This anticipation of outcome fits good with our results: the maxima of the histograms have almost the same number of counts and are located at almost equal amplitudes.
One of the main reasons for deviations is the different internal gain of SiPM 6 and 7.
This assumption is supported by figures 38a - 38b, for which we notice that for equal event number the amplitude of SiPM 7 is in the vast majority of the cases higher than the SiPM 6 amplitude. This can be even better observed when we look at the difference diagrams.
Notice that since both amplitudes are negative, the difference SiPM 7 - SiPM 6 is also negative, if SiPM 7 has a higher amplitude.

At this point, it is remarked that the event order diagrams as well as the amplitude difference diagrams of the third run were omitted due to space reasons but they look very similar to those from the first and second run.

Since Prototype 1 is a name for a detector with two seperate readouts, as mentioned in the 'description of Prototype 1', there exists also a seperate efficiency for each of them.

The efficiency of a detector is defined as the ratio between the successfully detected events and the number of total events.
So in order to calculate the efficiencies, one needs to define a criteria to distinguish between successful and background events. Thus the efficiency is dependent on the convention made.
In this thesis, we make the convention that we define a certain amplitude threshold such that events with lower amplitudes are considered as background events, i.e. no 'good' particle was measured.

For Prototype 1, we chose the amplitudes for failed events to be above -100 mV.
With this convention and given histograms, we obtain for the detector efficiencies:

	detector efficiency for SiPM 7 readout	detector efficiency for SiPM 6 readout
1st run	98.3 [+1.7, -3.1] %	98.2 [+1.8, -3.1] %
2nd run	98.0 [+2.0, -3.1] %	98.0 [+2.0, -3.1] %
3rd run	98.1 [+1.9, -3.1] %	97.9 [+2.1, -3.1] %

Table 19: calculated efficiencies of both Prototype 1 readouts

The determined values for efficiency are high and all very close to each other. This demonstrates, as stated in the previous experiment, the good and reliable light collection of Prototype 1, achieved with few SiPMs in combination with WLSFs.

Based on these well matching results, we repeated the measurements but with the test detectors attached at different positions of the Prototype 1 detector.

For comprehensible comparisons with the centered runs, amplifier board 1 was again used including the discriminator thresholds and board channel connections listed in table 17.
For all SiPMs used, slight deviations of the dark currents (up to $\pm$ 0.2 μA) from their nominal value (7 μA) occurred throughout the different runs.
For space reasons, we will not give the dark currents for each of the following efficiency runs, but refer to the dark currents in table 17.

At first we placed the test detectors at a position, we will abbreviate with 'left side', which is 27.5 cm from the edge of the black cap over SiPM 7.
Later, we deposited the test detectors at the position 'right side', which is 46.7 cm from the edge of the black cap over SiPM 7.

For better visualization, we provide in figure 40 a scheme showing the three measurement positions: centered, left side and right side.
The 2 cm difference was chosen to take into account that the fibres emerge 2 cm more on the SiPM 6 side than on the SiPM 7 side.

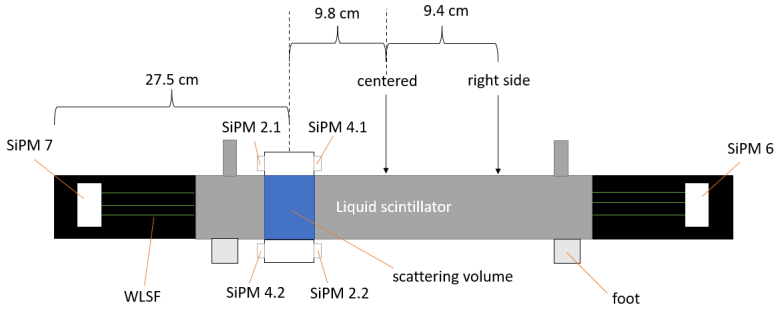

Figure 40: Prototype 1 scheme in left side position with marking of centered position and right side position. Mind that for each position, the markings were aligned with the center of the test detectors.

The histograms of 2 left side runs are grouped together down below in one histogram:

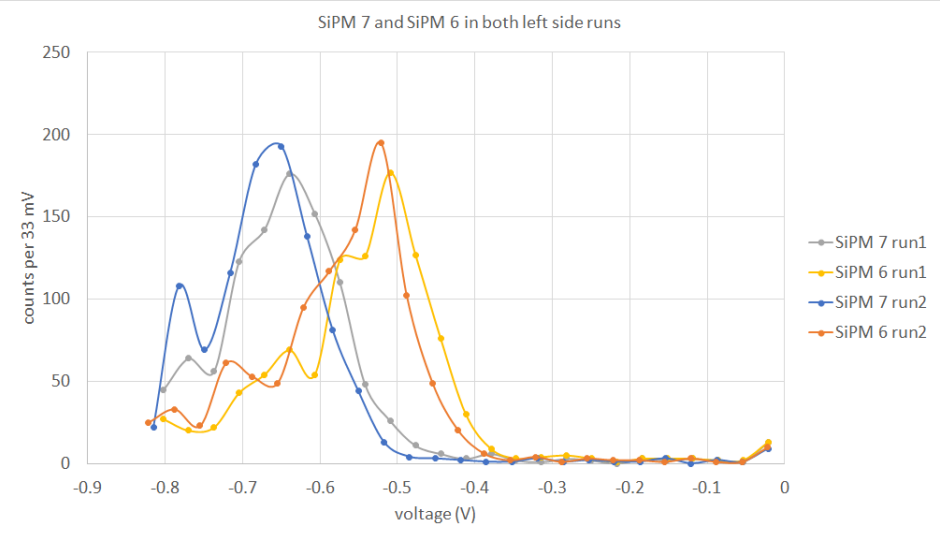

Figure 41: Prototype 1 histograms of 2 left side runs plotted in one graph

Graph 42 provides a comparison between the measurement in centered position and in left side position:

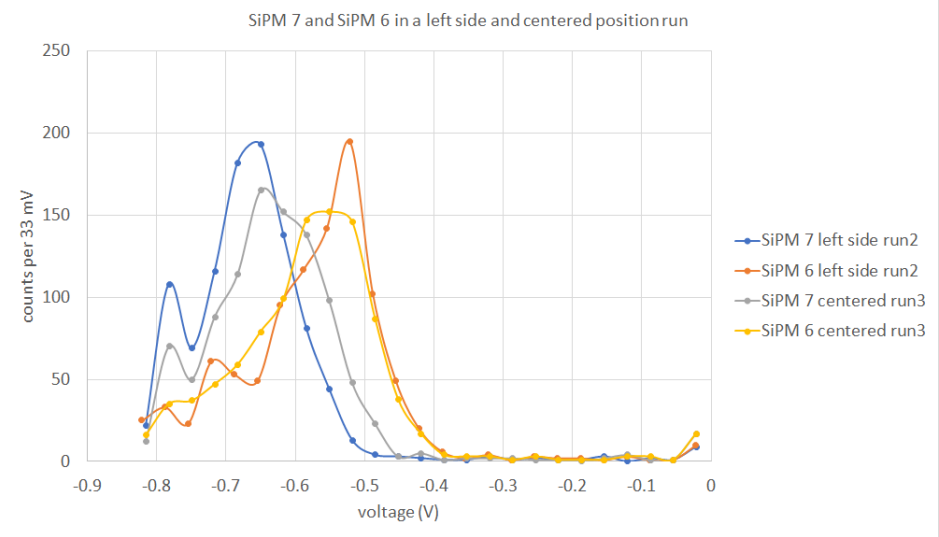

Figure 42: Prototype 1 efficiency measurement: comparison of centered run 3 histogram and left side run 2 histogram within one graph

Analogous to the previous position, we can examine the event order and the corresponding amplitude differences, which are depicted in graph 43a, 43b respectively figure 44a, 44b.

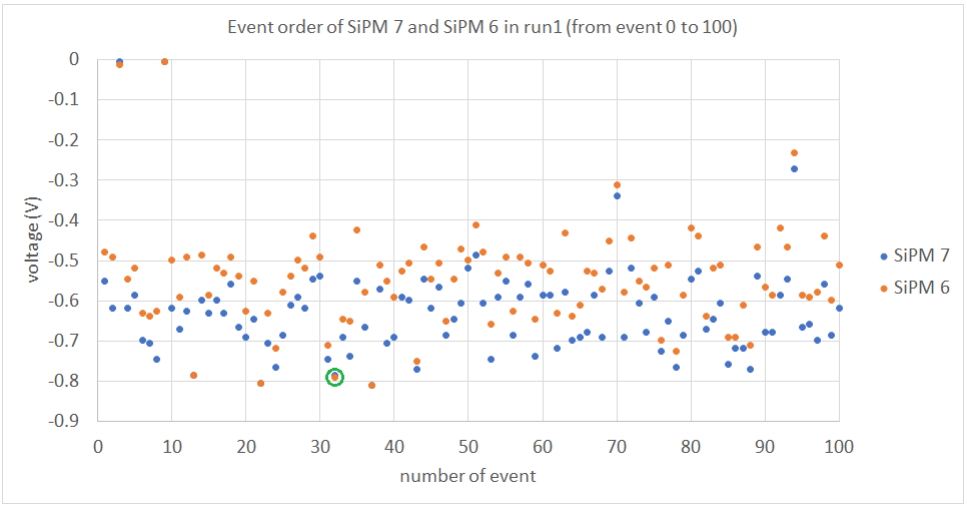

(a)

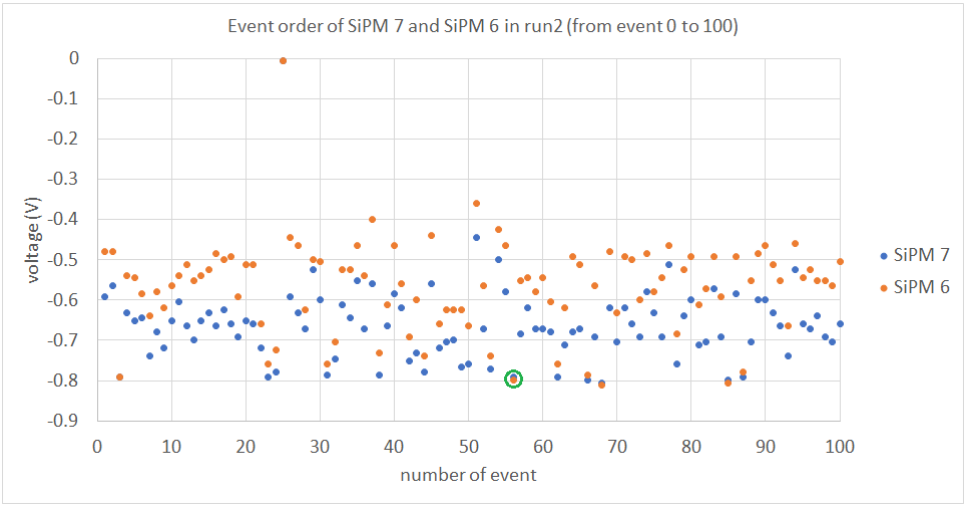

(b)

Figure 43: Prototype 1 efficiency measurement: event-order plots for 2 left side runs

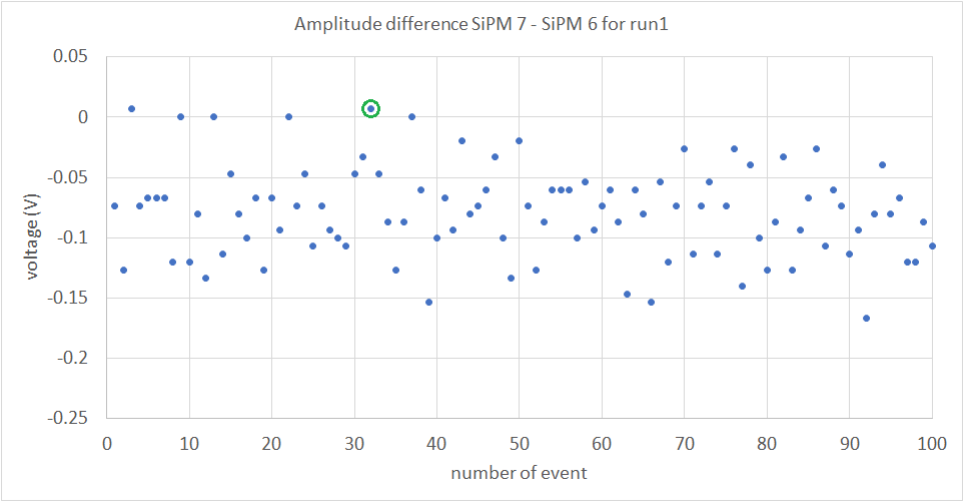

(a)

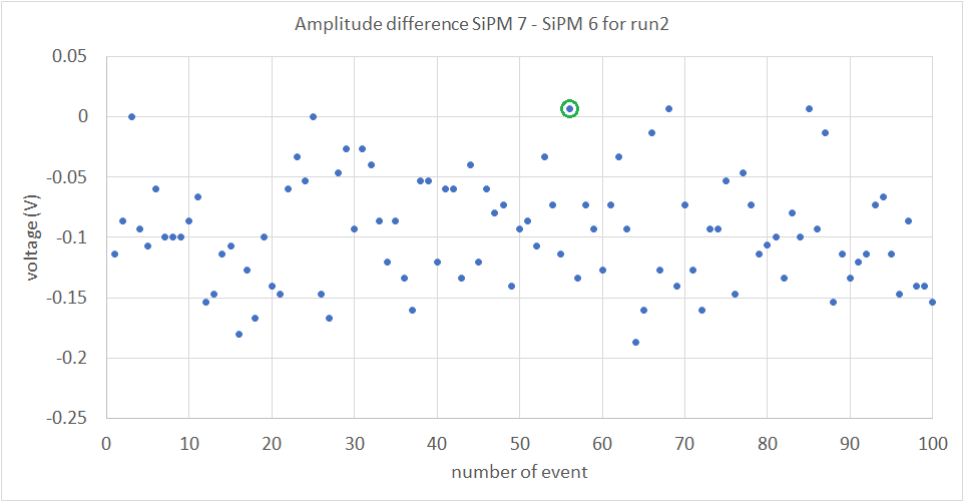

(b)

Figure 44: Prototype 1 efficiency measurement: difference plots for both, left side runs

Again for events, that fulfill the trigger condition, the measured scintillation light is produced in a small scattering volume inside Prototype 1.
However the scattering volume has moved with the test detectors and thus the distance to be covered to SiPM 7 is smaller compared to SiPM 6. As a consequence of the length-related outscattering, the fraction of scintillation light arriving at SiPM 6 is smaller than that arriving at SiPM 7.
So, we predict for the 'left side' measurements higher mean amplitudes for SiPM 7 and lower SiPM 6 mean amplitudes as in the centered position case.

Indeed, the presented results turn out to be consistent with this anticipation: the peak of the SiPM 7 histogram has moved to higher amplitude regions, while the SiPM 6 histogram peak is shifted to the right of the corresponding histogram in centered position (as can be seen in figure 42).
At the same time, the histograms in the region below -400 mV look very similar and thus we get almost equal efficiencies.

Declaring events below -100 mV again to background events, we obtain the following efficiencies for the Prototype 1 detectors:

	efficiency SiPM 7 detector incl. error	efficiency SiPM 6 detector incl. error
1st run	(98.4 [+1.6, -3.1]) %	(98.3 [+1.7, -3.1]) %
2nd run	(98.8 [+1.2, -3.1]) %	(98.8 [+1.2, -3.1]) %

Table 20: calculated efficiencies of both Prototype 1 readouts in left side position

The histograms in figure 41 demonstrate in a notable precision the reproducability of the experiment.
Analysing the event order diagrams, we observe this shift to higher amplitudes for SiPM 7 events and to lower amplitudes for SiPM 6 events for individual counts. The difference between events of same event number has increased for almost all events, as can be seen in figures 43a and 43b.
It can be observed even better in figures 44a and 44b, where we see the difference SiPM 7 amplitude minus SiPM 6 amplitude for the corresponding event number.
The vast majority of the differences is negative, since the SiPM 7 amplitude is almost always greater than the SiPM 6 amplitude.
Most exceptions happen in the region close to -0.8 V, which is caused by the amplification limits of the amplifier board (encirceled points).

The right side position is obtained by mirroring the left side position at a vertical axis crossing the point at half the length of SiPM 6 to SiPM 7 (see figure 40).
Note that the point at half the length of SiPM 6 to SiPM 7 does not exactly coincide with the centered position, since the fibres do not emerge equally at both ends of the casing.

In the right side position, the scattering volume inside Prototype 1 is closer to SiPM 6, resulting in a higher fraction of scintillation light to arrive at SiPM 6 and in a lower fraction to arrive at SiPM 7. Therefore we expect that the amplitudes of SiPM 7 decrease, while the amplitudes of SiPM 6 increase. If the SiPMs had exactly the same internal gain, we would predict that the amplitudes of SiPM 6 exceed the amplitudes of SiPM 7 and thus the difference SiPM 7 amplitude minus SiPM 6 amplitude should become positive. Another implication would be that the histograms of both detectors should swap positions with the left side results. But due to internal gain difference, there might be deviations.

In figure 45, the histograms of two measurement runs in right side position are shown in one plot.

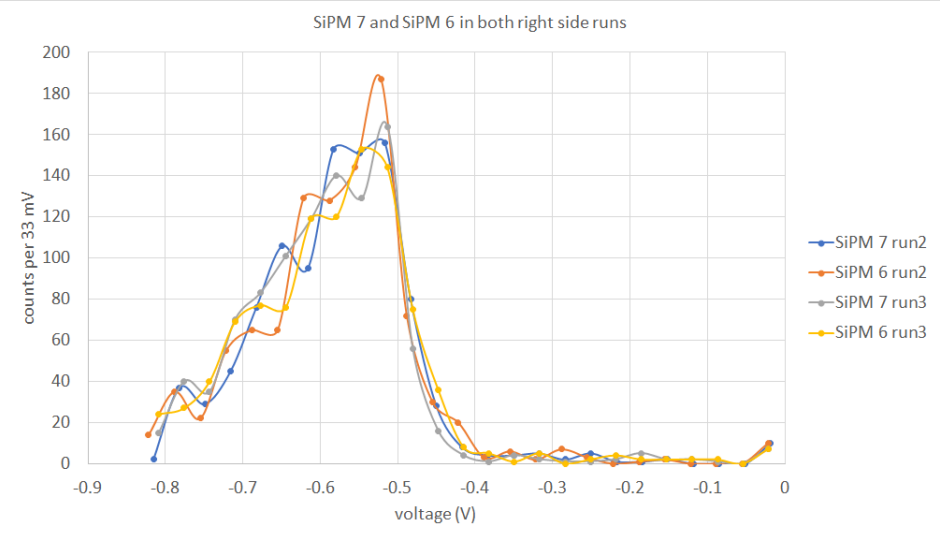

Figure 45: Prototype 1 histograms of 2 right side runs plotted in one graph

Analogously to the other two measurements, the event order for the right side measurements was investigated and is presented in the following graphs (see figures 46a, 46b).
Furthermore, the difference SiPM 7 amplitude minus SiPM 6 amplitude is depicted in figures 47a, 47b.

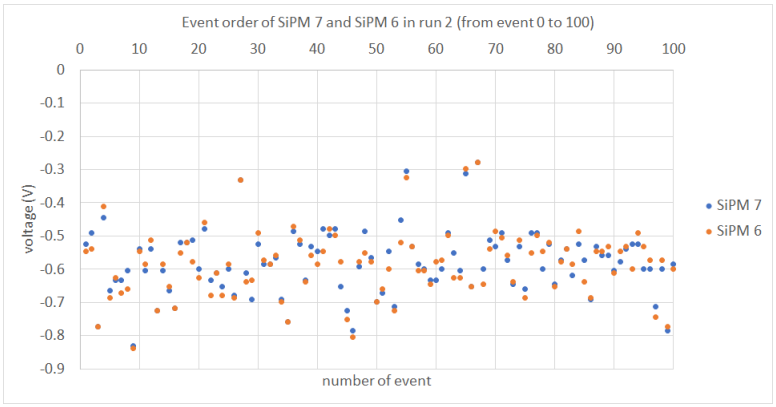

(a)

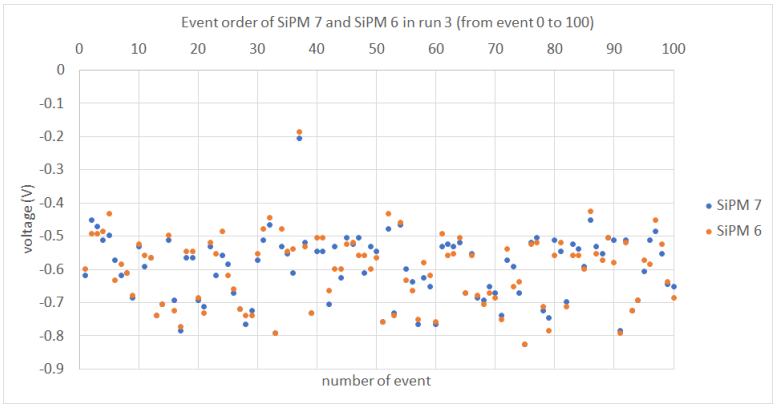

(b)

Figure 46: Prototype 1 efficiency measurement: event-order plots for 2 right side runs

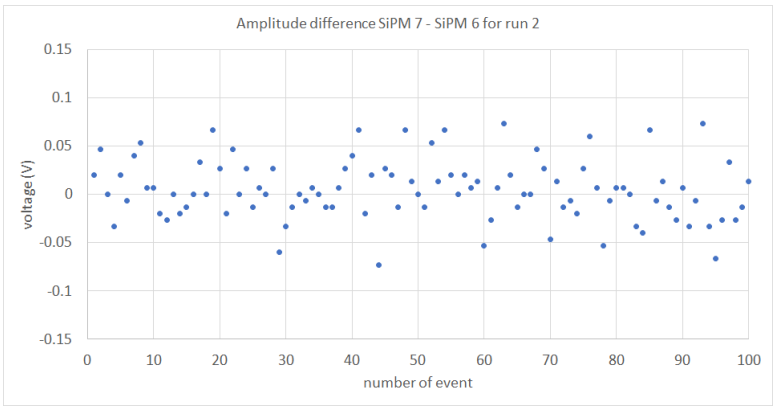

(a)

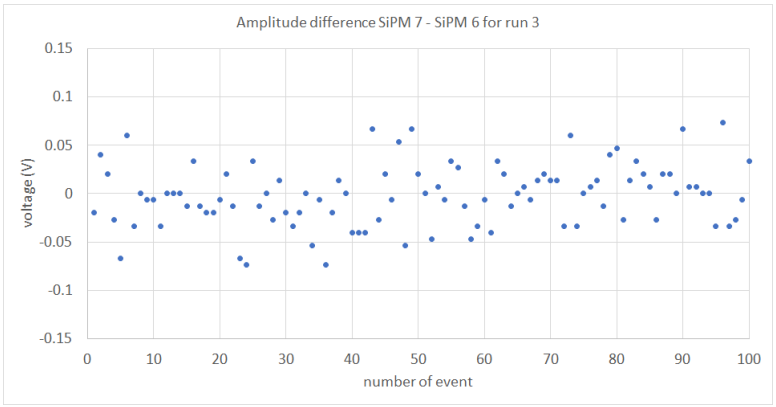

(b)

Figure 47: Prototype 1 efficiency measurement: difference plots for both, right side runs

Although we measure in a position that is symmetric to the left side position, the idealized outcome described above was not obtained.
The shifts in peak position are directed as anticipated but not too the extent the ideal case would suggest. Instead, we found that the histogram peaks are aligned over each other and further that the difference in individual amplitudes is distributed around 0 V and not around a positive value.
This is however not surprising, since the previous measurements revealed that the internal gain of SiPM 7 is larger than the internal gain of SiPM 6.
So despite receiving a lower dosis of light than SiPM 6, SiPM 7 turns it into a signal of almost equal amplitude as of SiPM 6.

As far as the efficiency is concerned, we obtain under the same convention as before (amplitudes lower than -100 mV are deemed as background events), almost equal values:

	efficiency SiPM 7 detector incl. error	efficiency SiPM 6 detector incl. error
2nd run	(99.0 [+1.0, -3.1]) %	(99.0 [+1.0, -3.1]) %
3rd run	(99.2 [+0.8, -3.1]) %	(99.1 [+0.8, -3.1]) %

Table 21: calculated efficiencies of both Prototype 1 readouts in right side position

An explanation for the small deviations in efficiency at different positions could be statistical fluctutations. In this context, we have to point out that the evaluated measurements consists of 1000 events and fluctuations will be minimized if the sample would be larger.

Measurements at 3 different positions are of course not enough evidence to prove the position independence of efficiency, but at least we can state the following: If we would make the claim that detector efficiency is position independent, we haven't found anything that contradicts it.

In the following measurement, we recorded the amount of background our Prototype 1 setup is exposed to. Test detectors have been removed such that we had the Prototype 1 setup in use.
We used amplifier board 1 for signal amplification, whereby SiPM 7 and 6 were connected to the same board channels as in the efficiency measurements (SiPM 7 amplified by board channel 9 and SiPM 6 amplified by board channel 10).

In total, 6 background measurements with 1000 events respectively, were recorded: for 3 runs we used the analogue signal of SiPM 7 as trigger and for the other 3 runs we triggered on the analogue signal of SiPM 6.
The dark current of SiPM 7 was adjusted to -6.91 μA and for SiPM 6, it was set to -7.00 μA.

The event order diagrams in the following graphs (see figures 48a - 48d) display the background using a trigger threshold of -100 mV.

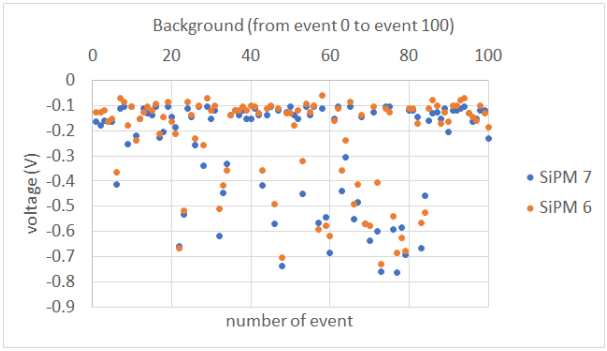

(a) Trigger SiPM 7 run 1

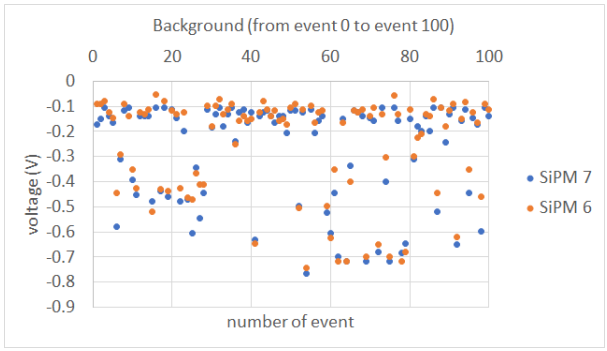

(b) Trigger SiPM 7 run 2

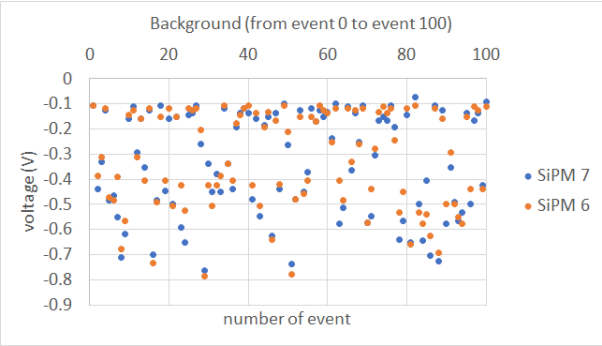

(c) Trigger SiPM 6 run 1

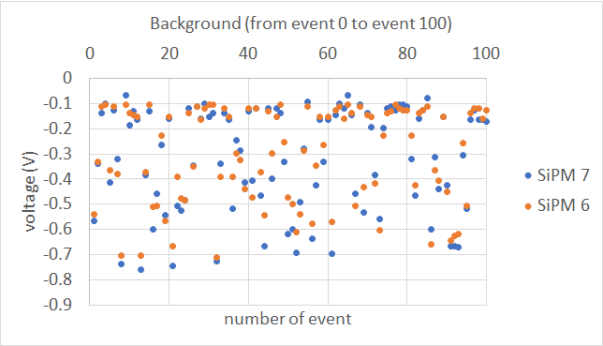

(d) Trigger SiPM 6 run 2

Figure 48: background measurements: event order diagrams for 4 of 6 runs

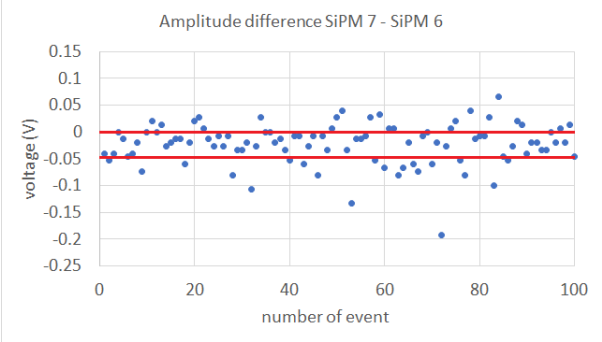

(a) Trigger SiPM 7 run 1

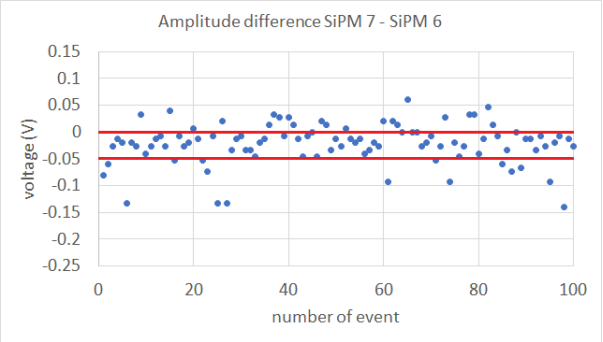

(b) Trigger SiPM 7 run 2

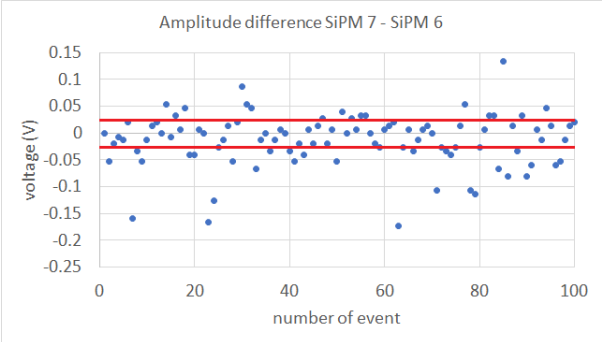

(c) Trigger SiPM 6 run 1

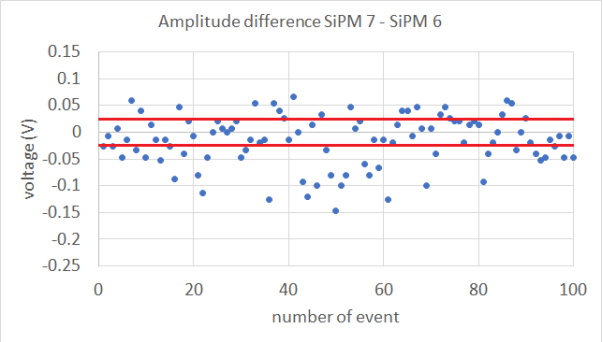

(d) Trigger SiPM 6 run 2

Figure 49: background measurements: amplitude difference diagrams for 4 of 6 runs

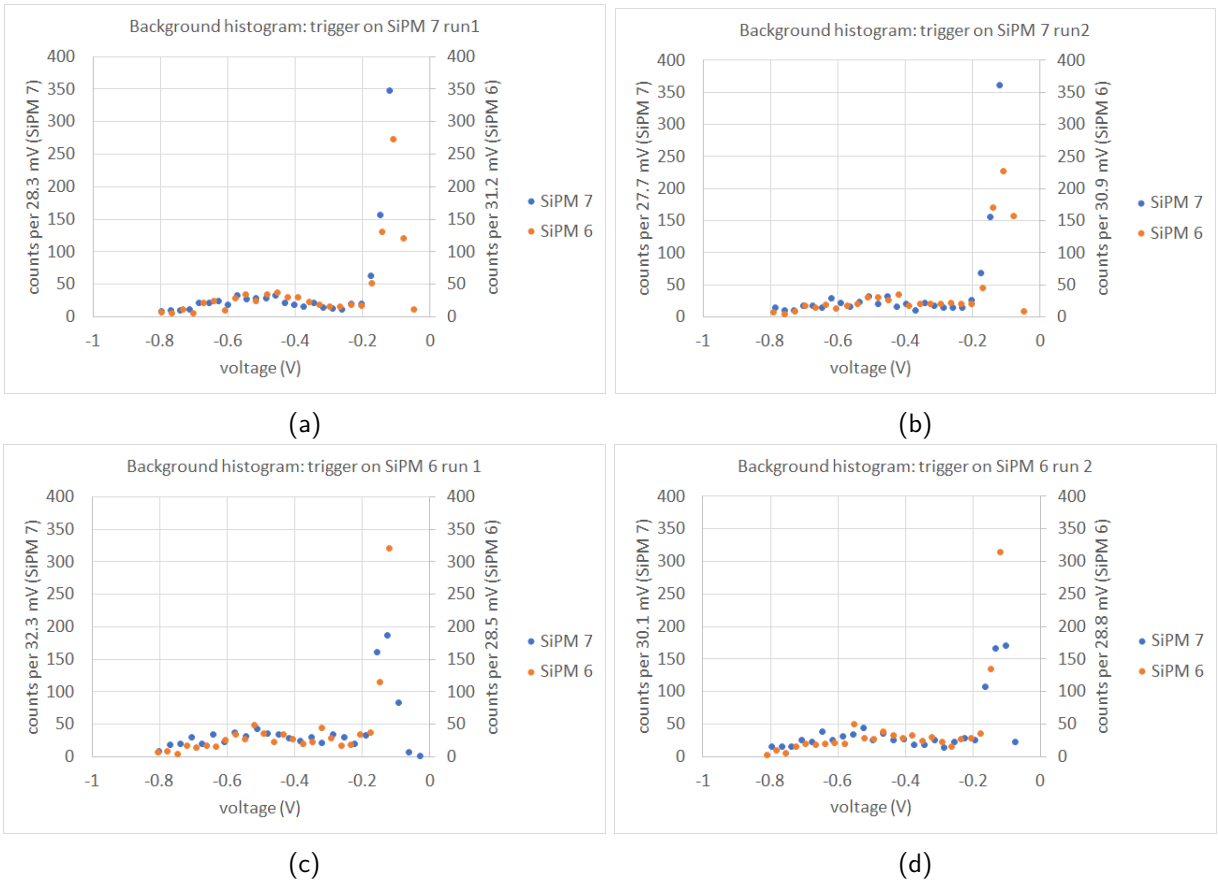

Figure 50: background measurements: histograms for 4 of 6 runs

From these ordered events, we also evaluated the amplitude difference of SiPM 7 and SiPM 6 at same event number, which can be seen in figures 49a - 49d.
As in prior experiments, we process the event order data into histograms with 25 bins.
These background histograms with 1000 counts each are presented in figures 50a - 50d.

In order to provide a more detailed picture of the background, we also determined the background rates at different thresholds.
These rates were calculated from the time for approximately 100 counts to occur and are collected in table 22.

SiPM 7	measured time and total counts	rates
threshold: -100 mV	45.65 s for 100 counts	2.19 counts/s
	45.27 s for 101 counts	2.23 counts/s
	46.23 s for 100 counts	2.16 counts/s
threshold: -200 mV	67.93 s for 100 counts	1.47 counts/s
	62.07 s for 101 counts	1.63 counts/s
	67.07 s for 101 counts	1.49 counts/s
threshold: -300 mV	73.07 s for 101 counts	1.38 counts/s
	71.58 s for 101 counts	1.41 counts/s
	67.73 s for 100 counts	1.48 counts/s
threshold: -400 mV	75.59 s for 101 counts	1.34 counts/s
	87.33 s for 100 counts	1.15 counts/s
	73.82 s for 101 counts	1.37 counts/s
SiPM 6	measured time and total counts	rates
threshold: -100 mV	49.58 s for 101 counts	2.04 counts/s
	46.65 s for 100 counts	2.14 counts/s
	46.18 s for 100 counts	2.17 counts/s
threshold: -200 mV	73.15 s for 102 counts	1.39 counts/s
	65.23 s for 101 counts	1.55 counts/s
	72.67 s for 100 counts	1.38 counts/s
threshold: -300 mV	73.35 s for 99 counts	1.35 counts/s
	72.32 s for 100 counts	1.38 counts/s
	74.20 s for 101 counts	1.36 counts/s
threshold: -400 mV	79.28 s for 100 counts	1.26 counts/s
	89.33 s for 101 counts	1.13 counts/s
	83.22 s for 101 counts	1.21 counts/s

Table 22: determination of background rates at thresholds of -100 mV, -200 mV, -300 mV, -400 mV

By studying the low voltage decay region in the background event order diagrams, we were able to make an important finding:
Since there are hardly any counts close to 0 mV, it seems as if a weak radioactive source is present. Among others, we identified radiation from the walls as one of the contributions to the background.
The presence of a weak radioactive source is also supported by the histograms. They show that the count distribution in the range of -300 mV to -650 mV follows roughly the form of a rectangle before it decreases with a flat decline.

In absence of radioactive sources, we would expect that the count number is high close to the threshold and decreases strongly towards higher amplitudes. However, we predict very low, but non-zero count numbers in the region ≤ -300 mV due to cosmics. The high proportion of counts in this range, which accounts for 30 - 45% of the total counts, clearly contradicts this expectation.
The approximately rectangular distribution in the ≤ -300 mV region suggests that shifts to higher thresholds will not result in severe changes in the shape of the spectrum.
Only a shift of the characteristic threshold edge towards the set threshold is expected.

In earlier experiments, we found that low energetic events occur more frequently than high energetic events. From this we deduce that the event rates drop when we increase the trigger threshold, since we exclude data below the threshold. This conclusion indeed fits with the measurement results from the tables.
Further one observes that for equal thresholds the rates of SiPM 6 are lower than those of SiPM 7.

Taking into account our knowledge about the internal gains of both SiPMs, this does not come surprisingly: Higher internal gain results in higher amplitudes and thus signals with amplitudes over the threshold occur more frequently.

In an attempt to check whether it is possible to deduce the trigger detector position from the measured amplitudes (position-sensitive measuring), we modified the efficiency setup shown in figure 40 to the one depicted in figures 51a, 51b.

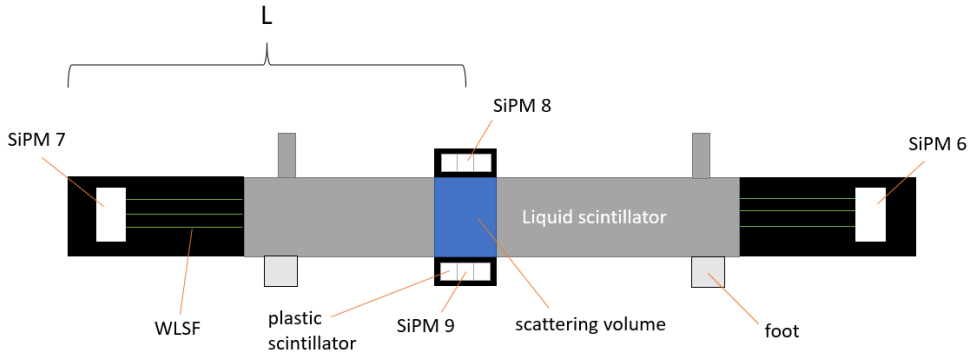

(a) frontview

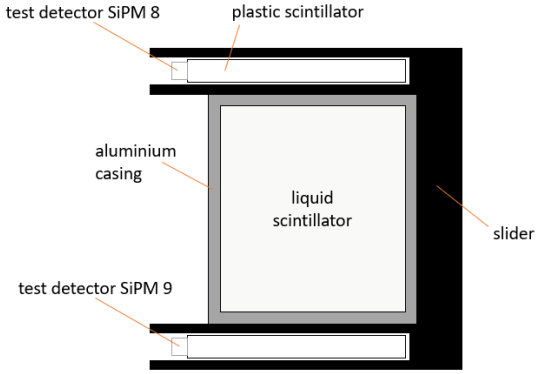

(b) sideview

Figure 51: modified efficiency setup using a black slider in which there are two plastic scintillator detectors with double SiPMs. The position of the slider is uniquely defined by the length L, ranging from the edge of the black cap over SiPM 7 to the center of the slider.
The plastic scintillators covering the SiPMs 8 and 9 had the following dimensions:
42 mm x 53 mm x 5 mm.
The pockets in which the plastic scintillator detectors were inserted have been closed light impenetrable afterwards with a special black tape.

Instead of fixing the detectors at the casing via tape strips, we modeled a slider with an upper and lower stacker pocket, in which we put a test detector, respectively. This slider could be moved along the symmetry axis of Prototype 1 and thus enables a flexible positioning of the test detectors.
Each of those test detectors consisted of a plastic scintillator emerging slightly over the edge of the Prototype 1 casing and a double SiPM[7] (see figure 51b). The SiPM on the upper detector was named SiPM 8, while the SiPM on the lower detector was called SiPM 9.

As triggering signal we used the AND signal of their digital signals, which were prepared previously with the following discriminator thresholds:
discriminator threshold for SiPM 8: -400 mV ; discriminator threshold for SiPM 9: -350 mV

[7]Once again, the double SiPMs were 2 ASD-NUV4S-P SiPMs from AdvanSiD connected in series.

Under these adaptions, we conducted amplitude measurements in three new positions (position 1, position 2, position 3). Position 1, 2 and 3 lie quite close to the centered, left side or right side position we had earlier, but they do not coincide exactly. Thus new names for the measuring positions were provided. Their definitions are given in analogy to the previous measurement: with a distance measure from the edge of the black cap over SiPM 7 to the center of the slider (see figure 51a).
Although the measured dark currents varied only slightly among the measurements, we provide them for each measurement position due to reasons of completeness (see table 23).

position 1		position 2		position 3	
SiPM name	dark current	SiPM name	dark current	SiPM name	dark current
SiPM 8	5.11 μA	SiPM 8	5.08 μA	SiPM 8	5.10 μA
SiPM 9	5.25 μA	SiPM 9	5.21 μA	SiPM 9	5.23 μA
SiPM 7	7.14 μA	SiPM 7	7.08 μA	SiPM 7	7.12 μA
SiPM 6	7.27 μA	SiPM 6	7.23 μA	SiPM 6	7.24 μA

Table 23: dark currents for the slider measurements in all 3 positions
position 1: L=35.7 cm ; position 2: L=23.1 cm ; position 3: L=49.3 cm

The histograms of these so-called slider measurements are collected in figures 52a - 52c. In addition, we plot the histograms of SiPM 7 from all three positions together in one graph (see figure 52d).

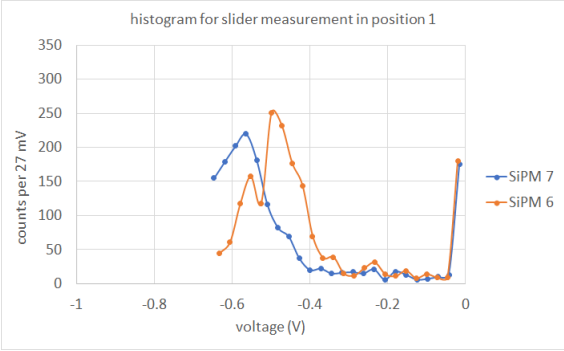

(a) L=35.7 cm
additional remark to 52a: an unfavorable set base line (i.e. 0 mV-line) caused that higher amplitude values were cut off (see also down below in the discussion)

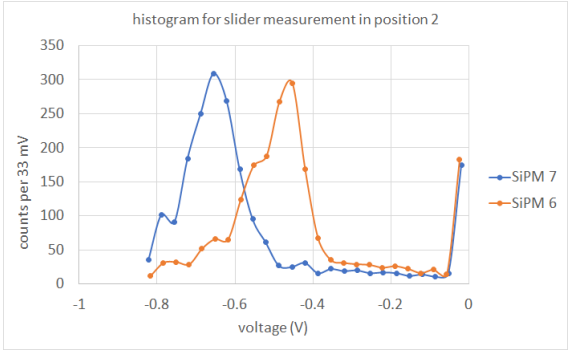

(b) L=23.1 cm

(c) L=49.3 cm

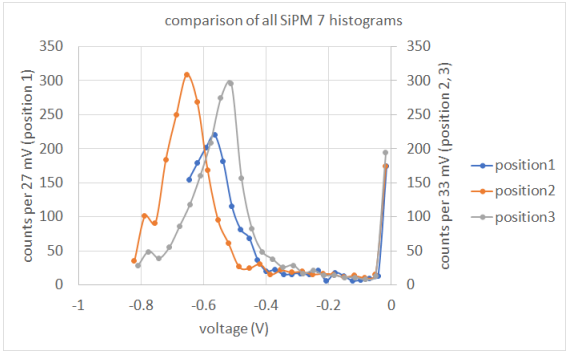

(d)

Figure 52: slider measurements: histograms of SiPM 6 and 7 in all three positions and seperate graph for all SiPM 7 histograms. Each histogram contains 2000 counts.

In the ideal case, the histograms of these modified measurements ('slider measurements') show a similar behaviour concerning shifts of the test detectors along the Prototype 1 symmetry axis as in the earlier setup. Comparing the graphs of both setups at same measuring positions respectively, we find similarities in certain characteristics but also deviations in the peak positions of the amplitude spectra.
For example, the dynamic range in position 1 is affected by misalignment of the oscilloscope baseline,

therefore higher amplitudes fall out of the measurement range. As a consequence, the histogram in position 1 (figure 52a) and in centered position (figure 37) do not agree that well.

One also notices a shift of the histogram peaks in the other two measurement positions: on the one hand the SiPM 6 peak in the position 2 run is displaced to a lower voltage value (compare with figure 41). On the other hand, the SiPM 7 peak in the position 3 run is slightly shifted to lower voltage values while the SiPM 6 peak is now located at a slightly higher voltage value (compare with figure 45).
The reason for this is that the test detector positions of this and the previous measurement series do not coincide exactly but deviate by some centimeters. However, these deviations have an effect in accordance with our expectations: the further away the test detectors are from SiPM 7/6, the lower the voltage value at which the SiPM 7/6 peak occurs.

Despite all these complications, we must emphasize that our main goal to check on position sensitive measuring succeeded. When we look at figure 52d, we find that the maxima of the SiPM 7 histograms move with the measurement position. As we would expect, the histogram peaks are at higher voltages if the trigger detectors are located closer to SiPM 7.
Conversely, for growing L, the peaks are shifted to lower voltage values, which perfectly fits with our earlier arguments about light collection and outscattering in the WLSFs. By comparison with the previous histograms we also find that we are not only capable to distinguish between the three extreme positions, but also to tell smaller displacements of the order of 3 to 4.5 cm.

In this series of experiments, we again see that the internal gain of SiPM 7 is larger than that of SiPM 6. As mentioned earlier, mirroring the measurement position should cause the histograms to swap places if the gain is the same. Instead, we find two approximately overlapping spectra for the histograms of position 3. The higher internal gain of SiPM 7 is now compensated by a better light collection at SiPM 6 and thus we get two approximately equal signals.

In the experiment, described in the following, we moved the slider with the test detectors to the center of the casing (25.3 cm from the casing edge) and measured the analogue signal amplitudes of SiPM 6, 7 and 8 using cosmics as source.
From the analogue signals, we additionally determined the dt@lv(SiPM 8, SiPM 6) and dt@lv(SiPM 8, SiPM 7) at the 20%-level.[8]
As before, SiPM 7 and 6 denote the readouts of Prototype 1 and SiPM 8 and 9 are used to read out the upper and lower test detectors. For this experiment, the amplifier board channels (board 1 was used) and dark currents were chosen as indicated in table 24.

SiPM name	amplifier board channel	dark current (μA)
SiPM 8	1	4.97 // 4.99
SiPM 9	2	4.97 // 4.97
SiPM 7	9	7.16 // 7.13
SiPM 6	10	7.10 // 7.12

Table 24: assignments of SiPMs to their used amplifier board channel as well as to the adjusted dark current.
Notice that the left dark current value was measured before the measurement start while the right dark current value indicates the value after the measurement.

In order to prevent background events in the records, we built with the AND signal of SiPM 8 and 9 and the AND signal of SiPM 6 and 7 a coincidence and used the resulting signal as trigger.
While the discriminator thresholds of SiPM 8 and 9 were adjusted to -400 mV, we chose -200 mV as discriminator thresholds of SiPM 6 and SiPM 7. Before being processed by the double coincidence method (coincidence of both AND signals), both AND signals were sent to a disciminator module to be broadened. This adaption was made to ensure a digital triggering signal of appropriate width.
In the course of the preparations, we took care of equal cable lengths to the oscilloscope for all trigger relevant digital signals, but also we checked that the analogue signals of SiPM 6, 7 and 8 have equal

[8]Recall the terminology introduced in section 'delays and hysteresis'.

cable lengths.

It turned out that a properly set hysteresis is crucial to obtain reasonable data sets.[9]
Otherwise multiple delay values are recorded, if a signal occurs that is superpositioned with noise of appropriate height (see chapter 'delays and hysteresis').
We changed the hysteresis several times and made several runs with small amounts of data points. This, however, has no influence on the measurement as long as the signal does not undergo fluctuations caused by noticeable noise.
Most of the data points were recorded using a hysteresis of 200 mdiv, but for longer measurements (i.e. over several days), a hysteresis of 500 mdiv for future delay measurements is recommended.

Table 25 provides the measured mean values including the standard-deviations.

	mean ± sdev.
amplitude SiPM 7	(-550.5 ± 95.9) mV
amplitude SiPM 6	(-409.9 ± 98.5) mV
amplitude SiPM 8	(-630.2 ± 104.7) mV
dt@lv(SiPM 8, SiPM 7) at 20%	(9.50 ± 0.72) ns
dt@lv(SiPM 8, SiPM 6) at 20%	(7.75 ± 0.65) ns

Table 25: mean values of measured quantities

For better comparison, the recorded amplitude histograms are visualised in figure 53a - 53c and the delay20 histograms in figure 54a, 54b.

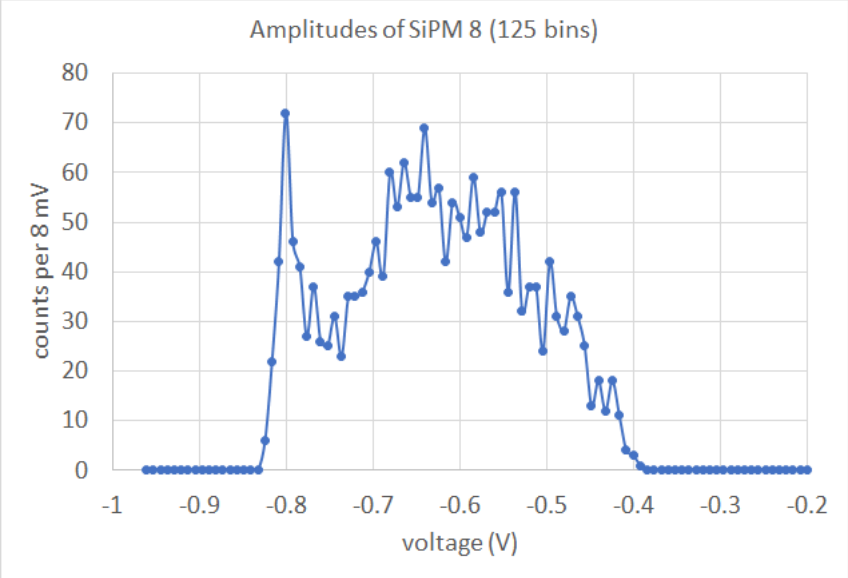

(a) The peak at -800 mV is due to overflow: cosmics that incide oblique or propagate very close to SiPM 8 lead to very high amplitudes (≈ -800 mV). The signal amplification done by the amplifier board is not arbitrary but amplifies up to a maximum signal amplitude that cannot be exceeded. Therefore there is an agglomeration of events with this maximum value in the measuring data. The region of -500 mV to -700m V is made up of vertical or steep inciding events taking place in the center. Counts with amplitudes between -400 mV to -500 mV could be due to vertical inciding cosmics propagating very close to the scintillator edges such that some light is scattered out of the scintillator.

[9]The hysteresis control is a measurement setting provided by the oscilloscope and was described in section 'delays and hysteresis'.

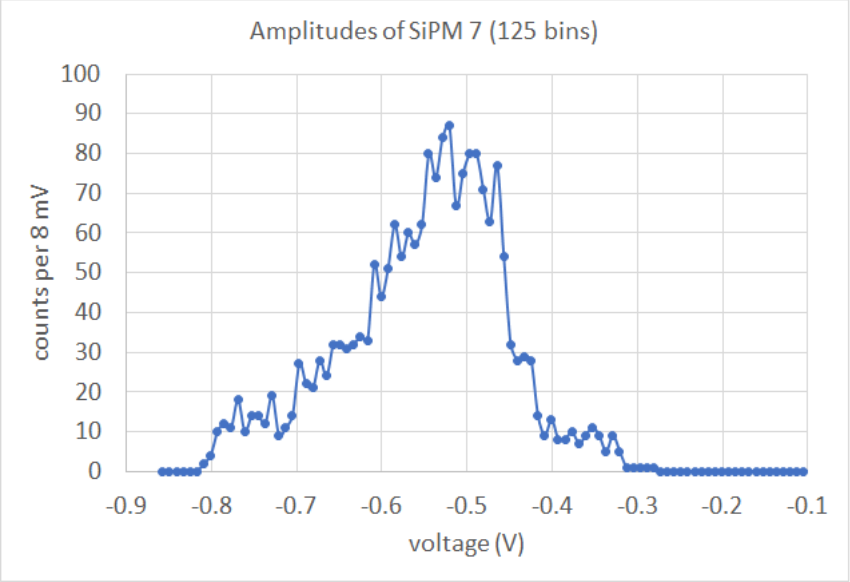

(b) Although the amplitude spectra of SiPM 7 and 6, both, have the same form (i.e. similar to a Maxwell-Boltmann distribution to some extent), the peak position of their spectra deviate strongly. While the amplitude peak of SiPM 7 is located at ≈ -550 mV, the amplitude spectrum of SiPM 6 reaches a count maximum at ≈ -380 mV. The reason for this large difference is the deviation in SiPM internal gain, which we encountered several times so far.

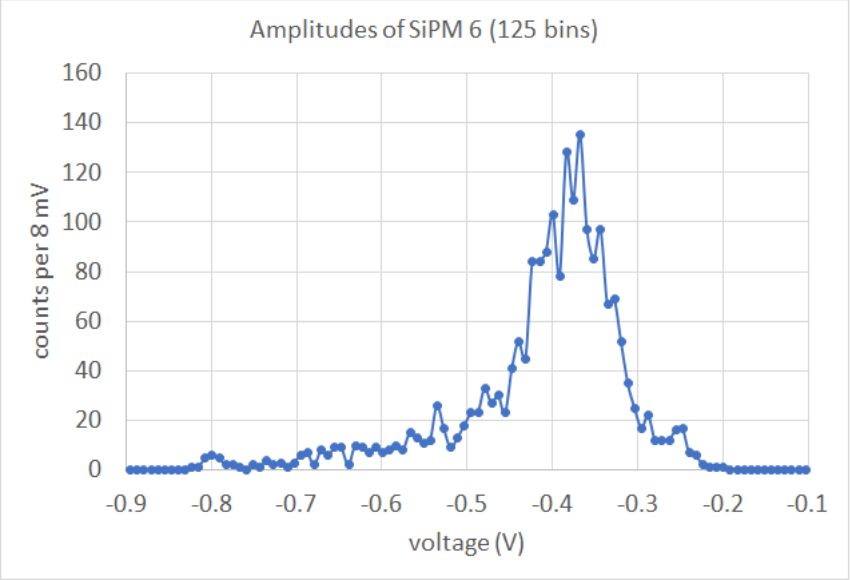

(c) As mentioned in 53b the peak position of the SiPM 6 amplitude histogram is at ≈ -380 mV.

Figure 53: amplitude histograms of SiPM 8, SiPM 7 and SiPM 6

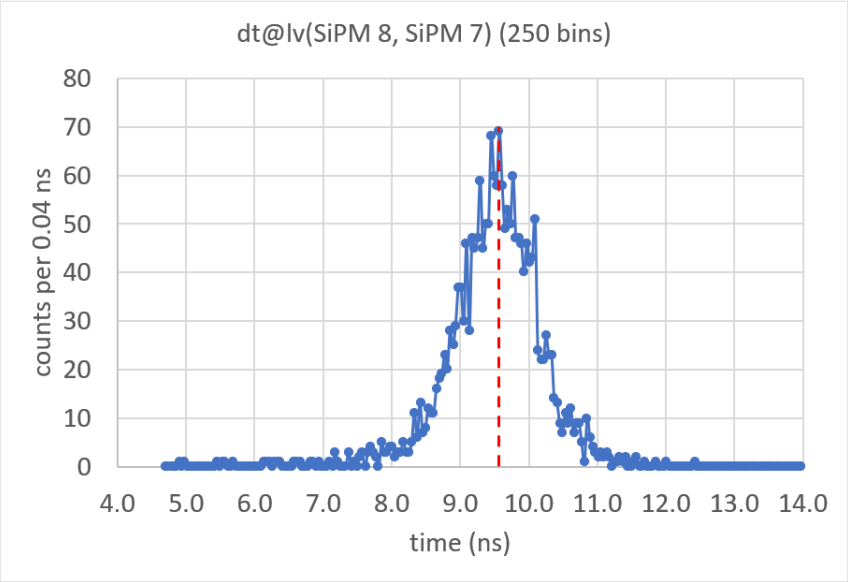

(a)

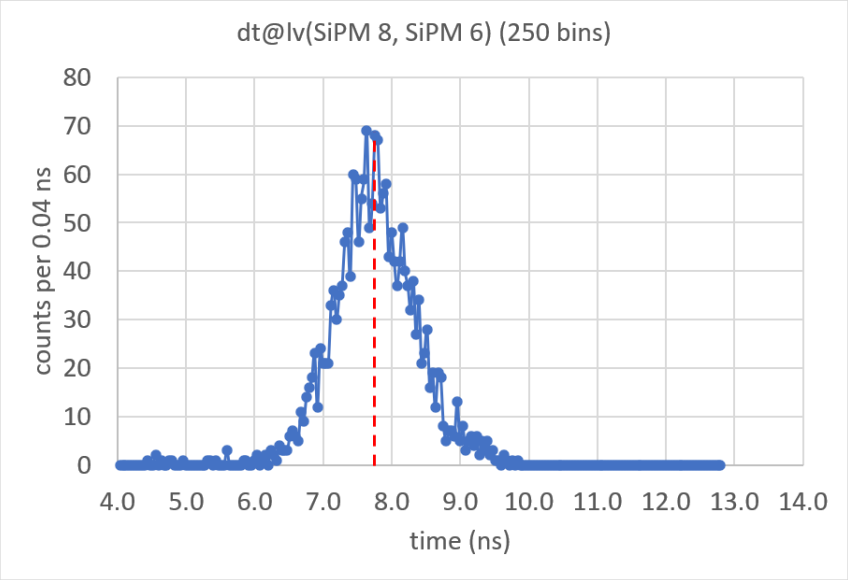

(b)

Figure 54: delay at 20% - level between SiPM 8 and SiPM 7 respectively between SiPM 8 and SiPM 6

A good point to start with the discussion of the graphs is the triggering signal and its consequences. Remember, measurement values are only recorded if the triggering signal fulfills the trigger condition, i.e. the signal amplitudes of SiPM 8 and 9 must be above -400 mV, the signal amplitudes of SiPM 6 and 7 must be higher than -200 mV and finally there must be an overlap within the defined trigger region.
Accordingly, we observe that the analogue signal amplitudes of SiPM 8 are greater or equal to -400 mV, while the analogue signal amplitudes of SiPM 6 and 7 have a lower boundary of -200 mV.
Furthermore, we know that the amplifier board has a maximum output of approximately -800 mV, providing an upper limit.

Recalling that cosmics fulfill $\frac{dE}{dx} \approx$ constant, leads us to the conclusion that the total energy deposition $dE = \frac{dE}{dx} \cdot dx$ in a scintillator depends predominantly on the length of the covered paths, Δx. As we have discussed earlier, Δx follows a frequency distribution best found by a Monte Carlo simulation, which we won't do here. However, we will give an impression on some basic properties of the distribution.

Looking at figure 51a and imagining possible cosmic paths through the setup, it is intuitively clear that the trigger condition is satisfied by a large number of vertical and steep-angle-of-incidence trajectories and only by a small number of trajectories with flat angle of incidence.

In considerations made for the energy-calibration, we found that trajectories with a flat angle-of-incidence come with a larger covered distance, Δx, than for trajectories with a steep or vertical angle of incidence and thus they deposit more energy in the scintillator.
Combining these informations, we predict an asymmetric energy distribution with more counts in the low-voltage region and few counts in the higher-voltage region.
Superposition with additional influences such as scattering effects within the fibre, imperfections of the fibre surface etc., leads eventually to the spectrum in figures 53b, 53c, that looks similar to a Maxwell-Boltzmann distribution.

The following can be stated about the delay measurements:
considering random, independent parameters, that determine the delay such as scattering angles in the fibres and light absorption ratio by the fibres, we predict a Gaussian distribution.
Figures 54a and 54b show that this distribution is indeed realized.
Due to the alignment of cable lengths and time order of the signal creation, we assume that the rise of the SiPM 8 analogue signal happens before the rise of the other analogue signals is measured.
Thus the measured quantities dt@lv(SiPM 8, SiPM 6) and dt@lv(SiPM 8, SiPM 7) should take positive time values.

Under ideal conditions, the symmetric position of the trigger should lead to symmetric delay distributions and peak positions in the histograms.
The screenshot depicted in figure 55 shows that the analogue signals of SiPM 6 and 7 rise almost simultaneously, but due to differences in the amplitudes and slopes, the 20% values of SiPM 7 are reached later than the 20% values of SiPM 6.
This is the reason why the peak in the SiPM 7 delay histogram appears at a higher delay value than the peak of SiPM 6.

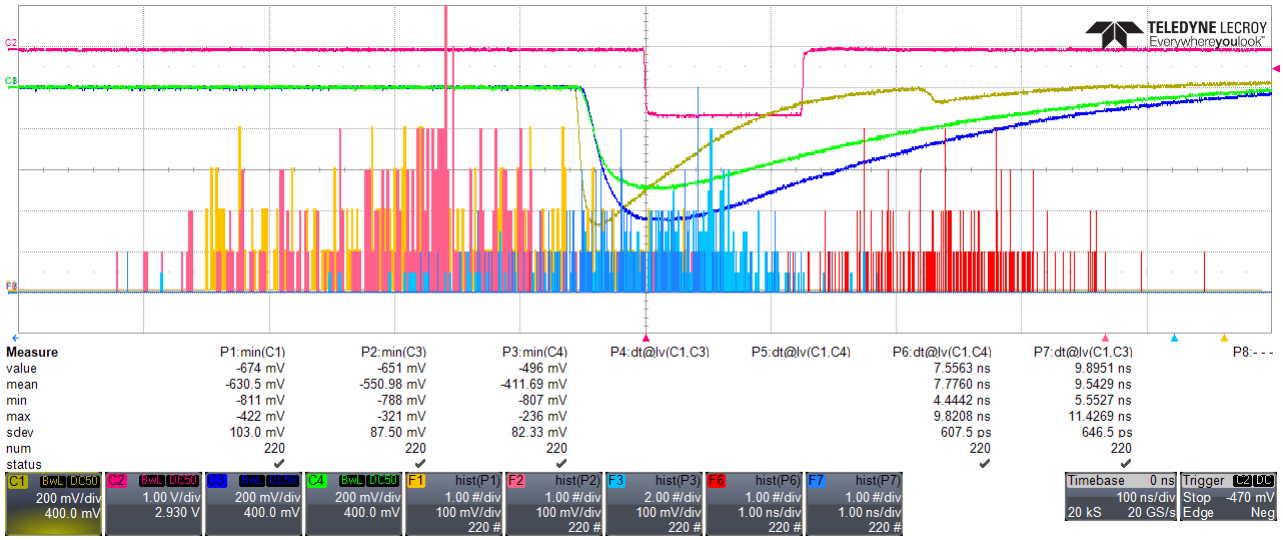

Figure 55: screenshot of one short measurement run with a hysteresis of 500 mdiv.
The coincidence of the broadened coincidences (pink signal) on CH2 was chosen as triggering signal.
Notice that the analogue signal amplitude of SiPM 7 (blue signal) on CH4 is higher than the analogue signal amplitude of SiPM 6 (green signal) on CH3.
Therefore, the delay at the 20% - level to the analogue signal from SiPM 8 (yellow signal) on CH1 is longer for the SiPM 7 signal than for the SiPM 6 signal.
From the depicted table, one can read off the mean value for dt@lv(SiPM 8, SiPM 6) (column P6: dt@lv(C1,C4)) and the mean value for dt@lv(SiPM 8, SiPM 7) (column P7: dt@lv(C1,C3)). Consequently, we obtain a difference of the mean values of
9.54 ns - 7.77 ns = 1.77 ns ≈ 2 ns

While we focussed in the last experiment on delay measurements between 2 analogue signals, we now want to investigate the delay between a digital triggering signal and an analogue signal.
In specific, we are interested in the delays between the triggering signal and SiPM 7 respectively SiPM 6 (Prototype 1 detector readouts) with the slider being in centered position.
Unlike to before, we now want to use the AND signal of SiPM 8 and 9 as triggering signal (instead of the coincidence of the AND of SiPM 6 and 7 with the AND of SiPM 8 and 9).
For the discriminator thresholds of the individual digital signals, we chose -400 mV for SiPM 8 and -350 mV for SiPM 9.

In the previous measurements we realized that the signal amplitudes and thus the internal SiPM gain have a significant influence on the delay values. Since we want to use the delay values as parameters to compare the signal propagation in different/opposite directions, we want to minimize this influence. Thus we adapted the dark currents such that the mean amplitudes in this position were almost the same. Additionally, the dark currents of both test detectors were raised to increase their gain and amplitudes. As a consequence of this, we obtain longer Time-Over-Threshold signals and higher rates.

Because of a relatively long measuring period, the dark current of all involved SiPMs was measured twice: the first time was right before the measurement was started and the second time was right after the histograms were saved.
For better overview, their values are listed in the following table:

	SiPM 6	SiPM 7	SiPM 8	SiPM 9
before start:	8.73 μA	5.33 μA	5.98 μA	6.05 μA
after saving:	8.72 μA	5.32 μA	5.98 μA	6.00 μA

Table 26: dark current values before and after the measurement

Figure 56a depicts the recorded amplitude histograms and figure 56b shows the delays between the SiPM 7 signal and the triggering signal at 25% levels as well as between the SiPM 6 signal and the triggering signal at 25% levels.

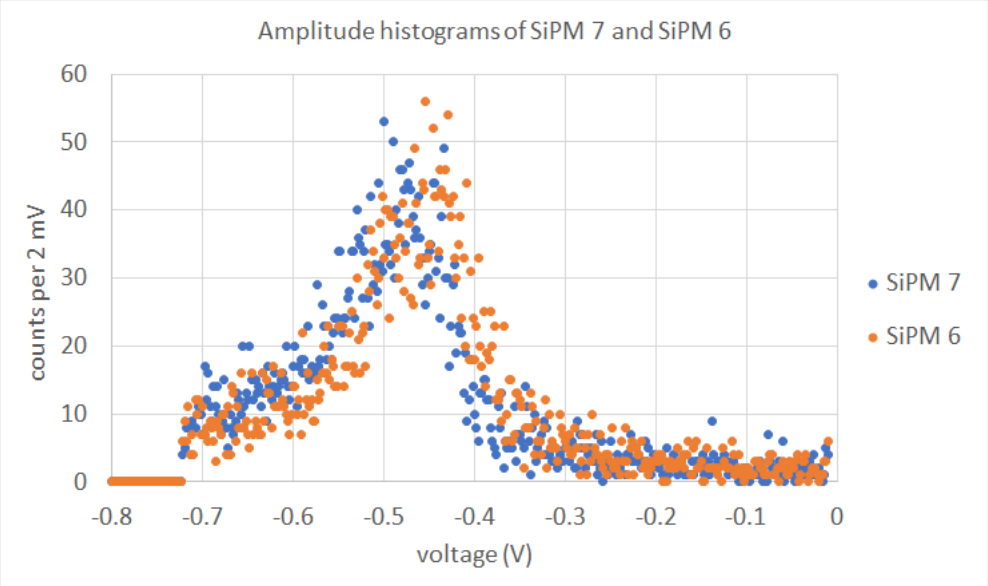

(a)

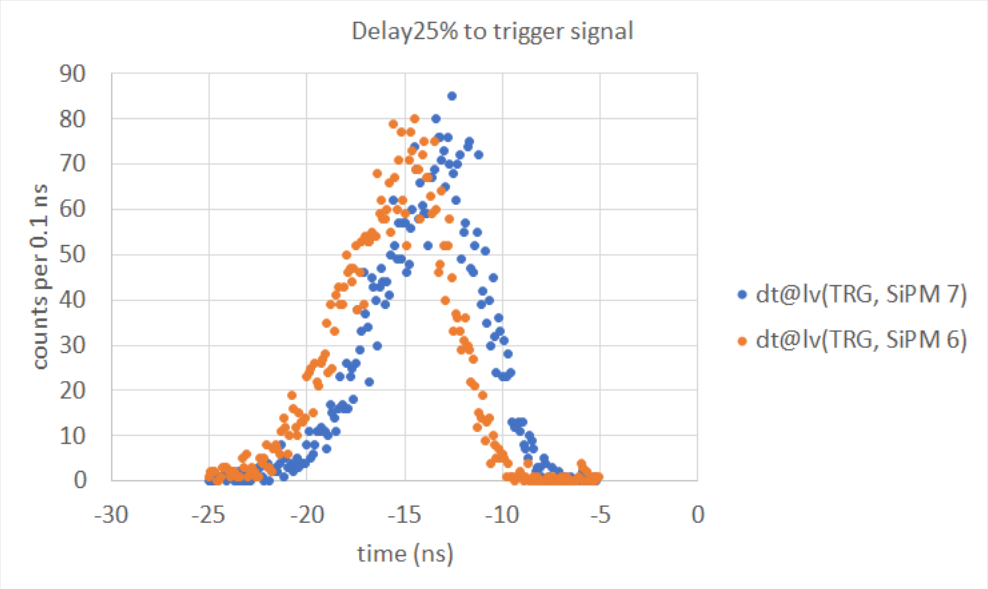

(b)

Figure 56: amplitude and delay histograms

The corresponding mean amplitudes and mean delays including standard deviations can be found in table 27.

	mean amplitude ± sdev.	delay trigger to respective SiPM ± sdev.
SiPM 7	(-458.9 ± 187.4) mV	(-13.9 ± 2.7) ns
SiPM 6	(-437.0 ± 182.7) mV	(-15.6 ± 2.7) ns

Table 27: collection of all measured mean amplitudes and mean delays including standard deviations

Looking closer at the amplitude histograms, one recognizes that they have some expectable characteristics. Since we are dealing with basically the same setup and the same source (cosmics), all prior considerations concerning the spectrum are still valid and we should obtain the same shape for the amplitude histograms (similar to Maxwell-Boltzmann distribution) as in the last experiment.

According to the changes in dark currents (dark current of SiPM 7 was reduced from 7.16 μA to 5.33 μA and dark current of SiPM 6 was raised from 7.10 μA to 8.73 μA), we expect the amplitude histogram peak of SiPM 7 to move to lower voltage values and at the same time the amplitude histogram peak of SiPM 6 to move to higher voltage values.
Even more: According to our choice of dark currents for SiPM 7 and 6, both SiPMs should now be per design equally sensitive.
If we take the symmetry of the measurement position into account, this should then imply that the spectra of SiPM 7 and 6 should be almost the same.
By looking at figure 56a we find that all these predictions are realized.
Beside the histogram shapes, we can interpret the low difference of mean amplitudes as another indicator for a well adjusted bias-driven gain.

Due to the renouncement of a coincidence of the coincidences, we do not impose a minimum amplitude on both Prototype 1 signals and thus background events starting with 0 mV are recorded as well.
In the last measurement, we demanded to have no amplitudes recorded in the (-200 mV, 0 mV] interval, but in this measurement $\approx$ 12% of the recorded events lie within this range. Therefore it's no surprise that these background events lower the mean amplitudes compared to the previous measurement.
When comparing the mean values in table 25 and table 27, the mean amplitude of SiPM 6 seems at first to contradict this explanation. The contradiction can be removed, however, when we consider that the SiPM 6 dark current has now a considerably larger value than in the previous measurement.

In figure 56a, the y-axis has been limited to the range relevant for us, so that overflow and underflow events are truncated.

Similar to before, we aligned cable lengths to make sure that the signals cover the same distance to the oscilloscope. Analogous to the previous experiment, the realised delay values are governed by a sum of independent random variables leading to a normal distribution.
When we compare with figure 56b we find that this assumption is indeed fulfilled. Due to the symmetric adjustment of amplitudes and covered distances, we ideally expect same values for the average delay and almost overlapping spectra. It turns out that this prediction matches indeed with the recorded histogram in figure 56b.
Although the average delay values are distanced by less than 1 σ, the extent of this difference with approximately 2 ns is quite high. So, we can conclude that the angle under which scintillation light is scattered within the WLSFs, varies strongly and therefore also the path covered from the point of its creation to the SiPM.

Although these expectations may seem at first glance to coincide with those of the previous experiment, one should be careful about a direct comparison.
First, the dark currents of the Prototype 1 readouts as well as the test detector readouts distinguish strongly from the previously tuned values (see table 25 and 27).
Secondly, the trigger was changed by omitting the AND condition that forced SiPM 6 and 7 to have a -200 mV minimum amplitude.
Thirdly, the measured delays as such are not the same. While the last measurement included the quantities dt@20%(SiPM 8, SiPM 7) & dt@20%(SiPM 8, SiPM 6), the current experiment involves dt@25%(TRG, SiPM 7) & dt@25%(TRG, SiPM 6).

8 Prototype 2 experiments

In this section, we will deal with two different types of signal amplifiers: the Arduino Amplifier Board, we had also in previous experiments and the shaping amplifier.
For a clear distinction, we will sometimes refer to the Amplifier Board as 'preamplifier'.
The final goal is to perform measurements using a TDC, testing 2 modules on top of each other and check if the resulting Prototype 2 detector works properly. (see figures 9a, 9b & 9c, 9d)

To achieve maximal transparency and reproducability, we decided to give names to all used modules, preamplifiers, SiPMs and to arrange them into pairings such that we do not mix up the devices and components throughout several measurements.
We will now list the conventions that have been followed throughout this chapter.
The readouts of the test detector are SiPMs called 'T1' and 'T2' and their signals are amplified on the board channels 1 and 2 of amplifier board 4.
One module has the name 'module 1' and is carrying the SiPMs N1, N2, ... , N12.
Its signals are amplified by amplifier board 1 (see figure 11a) only.
The second module has the name 'module 2' and is carrying the SiPMs N13, N14, M5, M6, N17, N18, N19, N20, N21, N22, N23, N24.
The signals of 'module 2' are amplified by amplifier board 2.1 (see figure 11b) only.

Before the modules can be combined to the Prototype 2 detector, it must be granted that both modules separately lead to reasonable histograms.
Thus, we positioned a start/trigger detector on top of the examined module (see figure 57) and performed a Time-Over-Threshold (ToT) measurement with a Time-to-Digital (TDC) Converter.
The trigger detector is a plastic scintillator detector of the kind, we described in chapter 3.1, with 2 SiPMs named 'T1' and 'T2' .
It has the following size: length: 100 mm , width: 100 mm, thickness: 10 mm.

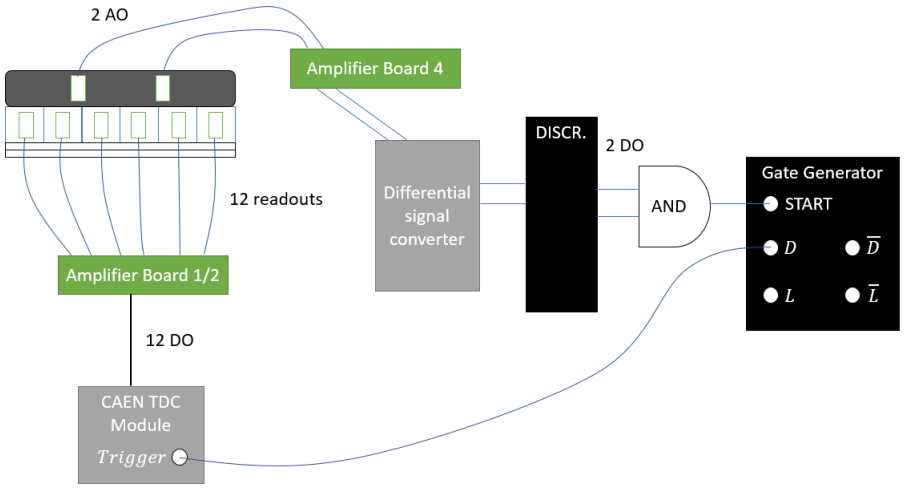

Figure 57: simplified scheme of TDC measurement setup.
For a better overview, the twisted two-wire cables from the SiPMs to the amplifier board are represented as one line. Also the flatband cable that connects the 12 digital outputs of the amplifier board channels with the TDC Module are represented by one (black) line.

A scheme providing details about the ToT measuring setup is provided in figure 57.
The digital signals to be measured, are guided from the digital ports of amplifier board 1 or 2 straight to the TDC module by flatband cables, where they are measured and processed.
Analogously to prior experiments, the digital signals are generated directly at the preamplifier board and the thereby needed threshold can be imposed on each board channel by appropriate software (in our case: Arduino).

For proper functioning, the TDC must be passed a so called 'time window': a time interval in which it should look for the digital signal of a certain event.
For this purpose the TDC module has a connector labelled with 'Trigger'.
If the 'time window' is properly set, the TDC will measure and digitize subsequently to each event the length of all ToT signals happening within the same time window.

Defining such a time window is a non-trivial task and involves a special processing of the test detector signals (see right branch of figure 57).
First, the 2 analogue outputs (AO) of the test detector were amplified at amplifier board 4, before they were converted from differential to single-ended signals at the Differential Signal Converter.
In a next step, we processed these single-ended, analogue signals to single-ended, digital signals at a discriminator unit.
Concretely, a Phillips Scientific Sixteen Channel Discriminator (Model 706 / Serial number: 15 886) was used.
The threshold separating between the digital states '0' and '1' was set to -105.1 mV.
Subsequently, the 2 digital outputs (DO) were combined to the coincidence signal of the trigger detector (also referred to as coincidence of the trigger detector readouts) via the AND logic.

This coincidence signal (yellow signal in figure 58) is then fed into the Gate Generator and one obtains two digital signals at the ports 'L' and 'D' as well as their sign-reversed signals at the ports '$\overline{L}$' (green signal in figure 58) and '$\overline{D}$' (orange signal in figure 58).

As far as the TDC-measurements are concerned, the 'L'-port signal ('gate') will serve as an auxiliary signal only. Its falling edge coincides with the falling edge of the coincidence signal, while its rising edge and thus its width can be adjusted with a rotary control as desired.
For the TDC measurement, its width was chosen to be between 800 ns to 1 μs.
For the 'L'-signal, a width inside this interval was picked to guarantee that the longest ToT signal will be completely inside the gate.

If this would not be the case, a ToT value would be saved before the signal to measure has ended.

The 'D'-port signal is a comparatively short digital signal (width: < 50 ns) and has the property of moving along with the rising edge of the gate. Even more: apart from small delays caused by the electronics, the falling edge of the 'D'-signal coincides with the position of the rising gate edge.
Due to this property, we will call the 'D'-port signal also the 'End-of-the-Gate (EoG)' signal.
For better visualization, it is recommended to check these properties with the signals in figure 58.
When doing so, keep in mind that the figure depicts the inversed signals '$\overline{L}$', '$\overline{D}$' instead of the 'L'- and 'D'-signals and thus the terms 'rising edge' and 'falling edge' must be reversed.
($\overline{L}$ and $\overline{D}$ are displayed on the oscilloscope in figure 58!)

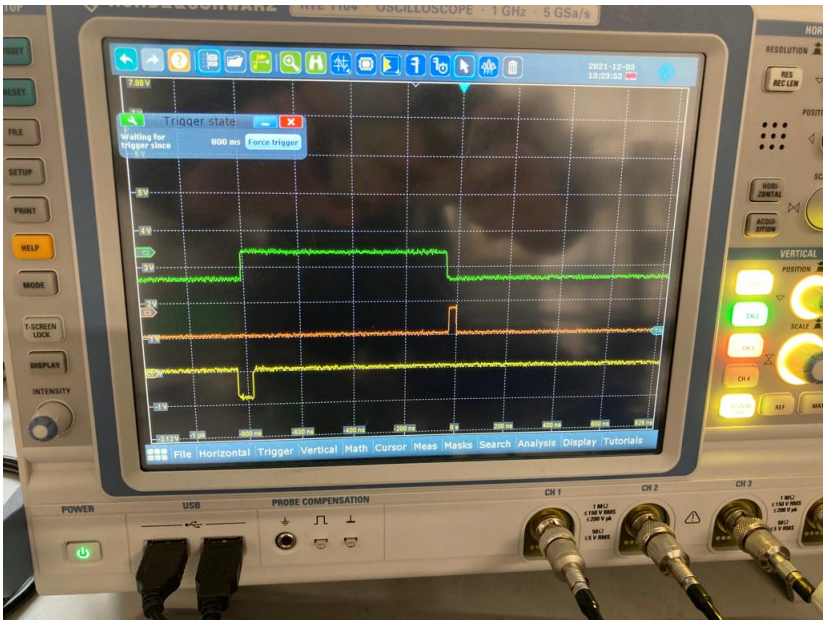

Figure 58: oscilloscope screenshot of the 3 relevant signals used in ToT measurements.
yellow signal: coincidence of the trigger detector readouts
green signal: sign-reversed signal of the 'L'-port signal (i.e. '$\overline{L}$'-signal)
orange signal: sign-reversed signal of the 'D'-port signal (i.e. '$\overline{D}$'-signal)

The EoG signal plays a crucial role in the TDC measurement, because it is sent to the TDC module and is used there to define the end of the 'time window'. One could also interpret the EoG signal as a clock signal for recording the Time-Over-Threshold values, since it marks the point in time when measurements are saved. Although the EoG-signal marks the end of the 'time window' we discussed above, the begin of the time window is not the falling edge of the 'L'-port signal.
Instead the time window has a predefined begin: per default it starts 1.5 μs before the EoG.
In principle, this predefined setting could also be changed, though, it's important that the time window fully contains the preset gate.

In figure 59, we depict the ToT histograms of all SiPMs attached to module 1.
The ToT histograms of module 2 can be seen in figure 60.
For simplicity, all histograms in figures 59, 60 were arranged in a way, that is consistent with the position of its generating SiPM on the respective module.
Table 28 associates the SiPMs to the set dark currents and the Arduino thresholds imposed on their digital signals.

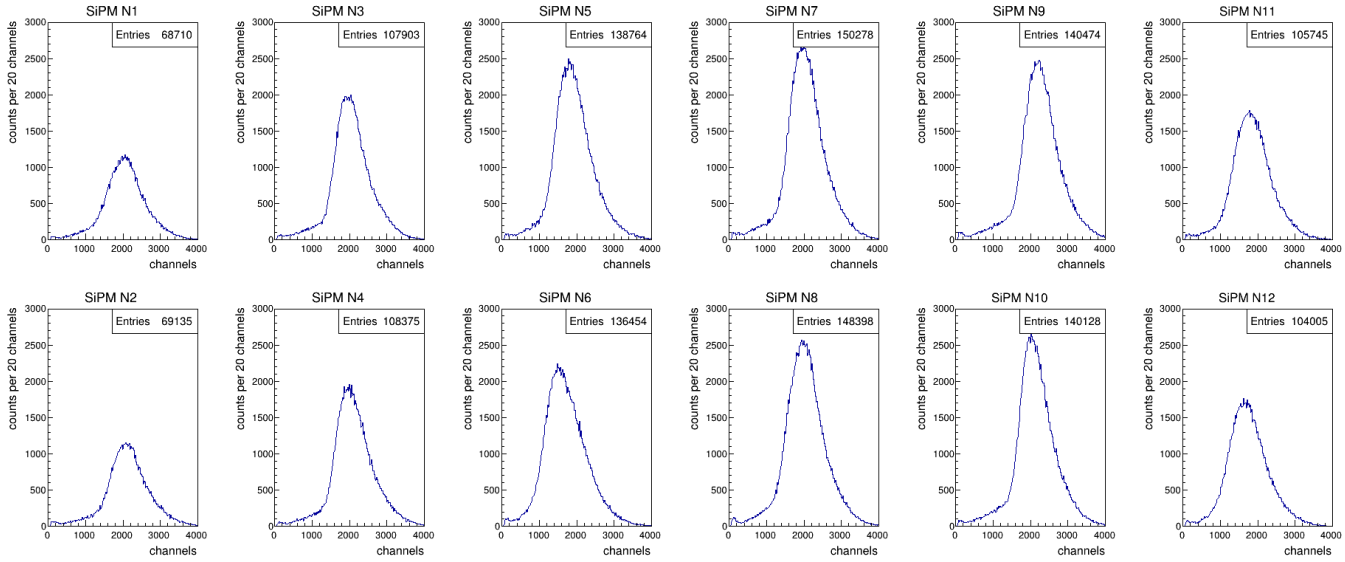

Figure 59: ToT histograms for all readouts of module 1.
The full ToT range of each histogram (≈ 4000 channels) was divided in 200 bins.
x-axis: ToT expressed in channels (100 ps = 1 channel), y-axis: corresponding counts

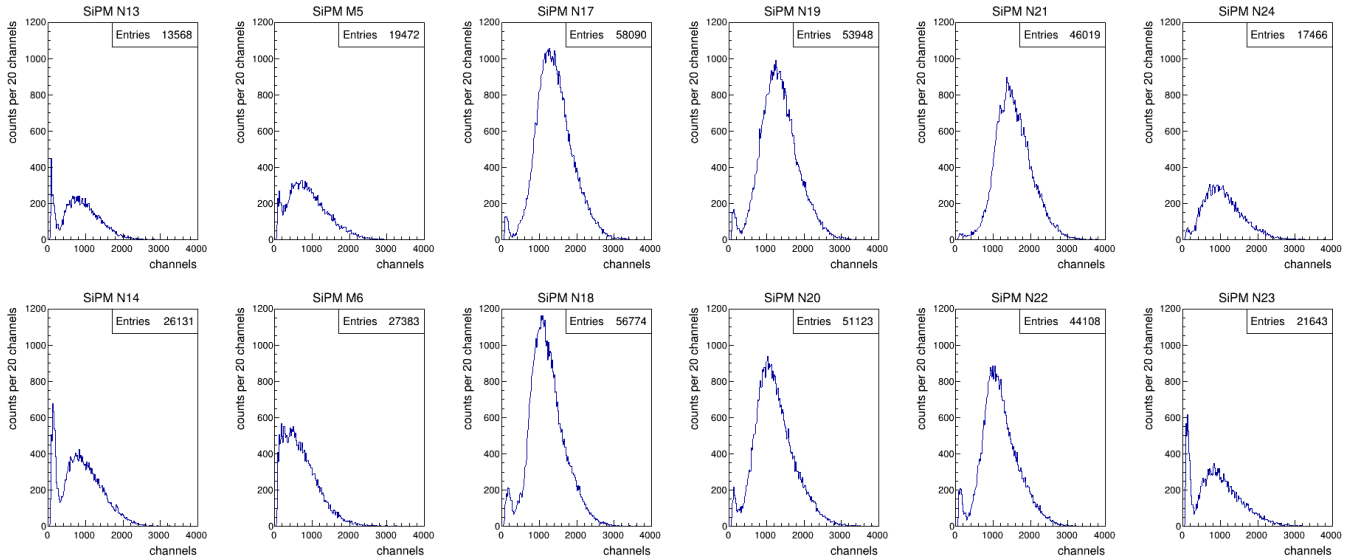

Figure 60: ToT histograms for all readouts of module 2.
The full ToT range of each histogram (≈ 4000 channels) was divided in 200 bins.
x-axis: ToT expressed in channels (100 ps = 1 channel), y-axis: corresponding counts

module 1			module 2		
SiPM name	dark current (μA)	threshold (1)	SiPM name	dark current (μA)	threshold (1)
N1	3.29	2500	N13	2.31 // 2.22	3100
N2	2.66	2500	N14	3.65 // 3.57	2900
N3	2.43	2500	M5	3.57 // 3.58	2500
N4	2.40	2500	M6	6.00 // 5.82	2500
N5	1.97	2500	N17	3.53 // 3.42	2500
N6	2.03	2500	N18	3.35 // 3.27	2500
N7	2.47	2500	N19	3.83 // 3.75	2500
N8	2.67	2500	N20	3.24 // 3.18	2500
N9	2.96	2500	N21	4.17 // 4.10	2500
N10	2.56	2500	N22	3.81 // 3.75	2500
N11	2.84	2500	N23	2.29 // 2.20	2500
N12	3.29	2500	N24	2.42 // 2.35	2500
test detector T1	8.96 // 8.22	-105.1 mV	test detector T2	8.92 // 8.02	-105.1 mV

Table 28: assignment of the SiPMs used in the test run of the respective module to their adjusted dark current and threshold.
Notice that the left value for the dark current was measured before the start of the measurement and the right value was measured after the measurement was stopped.

Notice at first that the ToT histograms in figure 59 look similar to a normal distribution.
From similar experiments conducted earlier, we know that the majority of the cosmics propagate vertically or with steep angles of incidence through the plastic scintillator detectors.
These correspond to the counts located at or close to the histogram peak.
Trajectories with flat angle of incidence do not appear as frequently and account for the counts at larger ToT values. The counts at the low ToT end are made up of smaller signals created by e.g. cosmics travelling only through the corners of the cuboid scintillator.
Such events come with a much lower rate than the vertical inciding cosmics.
Taking all these aspects into account, the histograms have an explainable shape.

Given what we know so far about digital signals and the Time-Over-Threshold, it is non-surprising that the ToT histograms depend on the total gain of the SiPMs and on the imposed thresholds.
For a comprehensible discussion of the ToT histograms, we want to start how changes of these quantities act out on these histograms in general.
An increase in gain leads to higher amplitudes and therefore to a broader ToT distribution. If we keep the number of events fixed, a broadening distribution implies that the number of counts at the peak must decrease.
By increasing the threshold, the Time-Over-Threshold becomes shorter and therefore the histogram moves to the left. If you change the threshold to a higher value, it is clear that we loose events that were previously recorded.
To represent the spectrum in a wide range, one should therefore choose a low but not too low threshold, otherwise the noise dominates and cosmic events are hardly visible.

In table 29 we depict for all readouts the number of channels corresponding to half the height of the histogram peak (abbreviated with 'cahh' ('channels at half height')). It serves us as a measure to compare the width and according to upper statements also as measure to compare the gain.

module 1		module 2	
TDC CH	cahh ± 200 (channels)	TDC CH	cahh ± 200 (channels)
N1	2600	N13	1400
N2	2700	N14	1500
N3	2500	M5	1300
N4	2550	M6	1200
N5	2400	N17	1900
N6	2250	N18	1600
N7	2500	N19	1800
N8	2500	N20	1700
N9	2800	N21	2000
N10	2550	N22	1600
N11	2300	N24	1600
N12	2250	N23	1500

Table 29: TDC measurement single module runs: we list for all readouts the number of channels corresponding to half the height of the histogram peak ('cahh').
Keep in mind that the unit 'channel' represents a time span of 100 ps.
The provided uncertainty covers reading errors made in the graphical evaluation.

When we look at the histograms of both modules, we notice that the readouts located on the edges of the module have low peaks and low total counts. It can be further observed that the peaks and the total counts become higher the closer the SiPM associated to the histogram is to the center of the module. This is due to another factor, we haven't considered so far: the relative position of the trigger detector to the module and the thereby associated geometry of the situation!

The time window defined with the help of the trigger detector obliges the recorded events of any readout to travel through the trigger detector first. Now, let's assume that the trigger detector is placed ideally on top of the module in use, i.e. the trigger detector covers the plastic scintillators all over the width, while the 10 mm plastic scintillator 'overlength' emerge evenly with 5 mm on the one side and with 5 mm on the other side.[10]
If we imagine all possible trajectories propagating towards the setup, we conclude that in the record of the outer plastic scintillator detectors many flat inciding trajectories will not be included.
The reason for this is obvious: either they do not travel through the trigger detector or they do not deposit enough energy in the outer plastic scintillators (no distance or negligible distance covered).

More generally we can say: detectors that lie closer to the module center are more likely to receive/measure trajectories that have crossed through the trigger detector with a flat angle of incidence. From this also follows that these more centered detectors measure more counts in the same time interval than less centered detectors. This statement is confirmed by figure 59 as well as figure 60.

In case of a non ideal positioning of the trigger detector, the trigger detector covers the outer detectors differently (e.g. the left most scintillator is not completely covered, but the trigger detector emerges beyond the edges of the right most scintillator). In this case, there are additional, vertically incident trajectories, that aren't detected by the readouts of the incompletely covered scintillator. Thus, we expect an asymmetry with respect to peak heights and count numbers with lower peak heights and count numbers on the incompletely covered module side.
For the module 1 test run, an imperfect positioning of the trigger detector onto the module could be the reason for the non symmetric peak heights. Concretely, it seems as if the trigger detector covered the outer detector on the right edge more than on the left edge.

A good coordination of dark currents and thresholds is a very challenging task, since finding proper values for all of them at the same time is very time consuming.

[10] recall the length, width, height of the trigger detector: 100 mm x 100 mm x 10 mm and the dimension of the plastic scintillator collective: 110 mm x 16 · 6 mm x 5 mm

If we look at the histograms and table 29, we find that the histograms have the shape described above and 'cahh'-values among module 1 are close together. Thus we can conclude that gain and threshold of module 1 are well set.

For module 2, though, we notice that SiPM N13, N14, M5, M6 as well as SiPM N23 and SiPM N24 look strange. Some of them have a second prong (SiPM N13, N14, M5, N23) near the low ToT-end or look like a part of the histogram was cut (SiPM M6) or look like if they have too few counts (SiPM N24).
From the second histogram prong, one can deduce that there are many signals with very short ToT, so either the threshold is too high or the gain is too low. The fact that the 'good' histograms also had an Arduino threshold of 2500 and give a much better spectrum supports the latter.
Additionally, the low 'cahh' values in table 29 also support a too low gain.

As a consequence, we increased the gain in the later conducted 'lattice' measurement, but the Arduino thresholds of SiPM N13 and N14 were lowered to 2500 as well.

Before the final Prototype 2 experiment, we examined for module 1 the amplitude spectrum of a Co-60 source. The main motivation for this was to get a good comparison of gain among the individual detectors.
The Co-60 source was successively placed at 5 different positions above the module via a small crane (see figures 61a, 61b) followed by a data acquisition done by a Peak sensing ADC (PADC).
The setup for this measurement is presented as schematical circuit in figure 61c:
the preamplified differential, analogue signals are converted to single-ended, analogue signals via an appropriate converter before they are transformed to Gaussian-shaped signals at the shaping amplifier. Finally those Gaussian signals are transmitted to the PADC, searching for the positive-valued maximum within a predefined time interval ('time window').[11]

Unlike as before, the 'time window' is not specified with help of a trigger detector but with the help of the Fast-Out (FOUT) signals generated from the shaping amplifier. These are non-shaped and smaller than those from the OUT ports, but with signal durations of about 100 ns they are much faster.
In figure 61c, the reader can trace the signal manipulations leading to the signal that governs the 'time window'. In a first step, the FOUT signals are sent to a discriminator where they are preselected with respect to amplitude and processed to digital signals.

We needed 12 discriminator channels, so we had to use 2 different discriminators. In our case, SiPM N1-N7 were connected to the Phillips Scientific Octal Discriminator Model 710 (Serial Number: 9411) and SiPMs N8-N12 were connected to Phillips Scientific five-channel timing discriminator Model 715 (Serial Number: 30274). At this point, it is important to mention that the chosen discriminators allowed us to set separate thresholds for the individual signals.
The allocation of SiPMs to the thresholds imposed on their signals is done via table 30.
For space reasons, the assignment of SiPM to dark current was also made in this table.

[11] although we made up the term 'time window' in the context of a TDC measurement, we want to recycle the term and want it to be understood in a similar sense: the time interval in which the PADC looks for the positive peak of the Gaussian amplitude signal. Analogously to before, it holds that no measurements are taken unless a time window has occured.

SiPM name	dark current (μA)	discriminator threshold (V)
N1	3.26	-0.480
N2	2.65	-0.403
N3	2.40	-0.512
N4	2.41	-0.402
N5	1.90	-0.317
N6	1.89	-0.329
N7	2.43	-0.305
N8	2.67	-0.660
N9	2.97	-0.356
N10	2.54	-0.508
N11	2.87	-0.491
N12	3.24	-0.388

Table 30: PADC measurement for module 1: dark currents and discriminator thresholds used for the respective SiPMs

Afterwards, all 12 digital signals are combined to one digital signal via an OR Logic. Typically it has a width of 100 ns. Next, the resulting OR signal is fed into a Gate Generator creating the 'L'-port signal ('gate') used to define the time window (in order of 10 μs.)
The preparation and the setup are completed when the gate signal was connected to the 'trigger' port of the PADC and when the settings listed in table 31 were adjusted.[12]

Settings for all SiPMs (adjusted by the Software 'Tera Term'):		
Coarse Gain: 32	Shaping Time: 3 μs	Out Polarity: Pos
Setting adjusted on the Shaping Amplifier itself:		gate width: $\approx$ 10 μs

Table 31: adjusted parameters for the PADC measurements

This finally fulfills our goal to trigger a measurement recording at all SiPMs, if at least one of them detects a particle, i.e. at least one of the amplitudes lies above a certain pre-defined threshold.

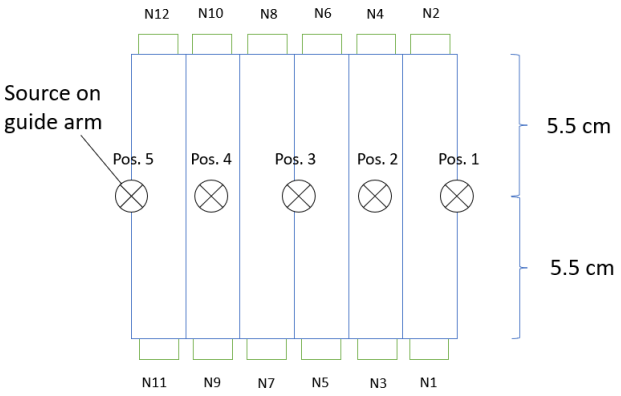

(a) view from top

[12]The meaning of the parameters Coarse Gain, Shaping Time and Out Polarity was explained in section 'shaping amplifier and ADC'.

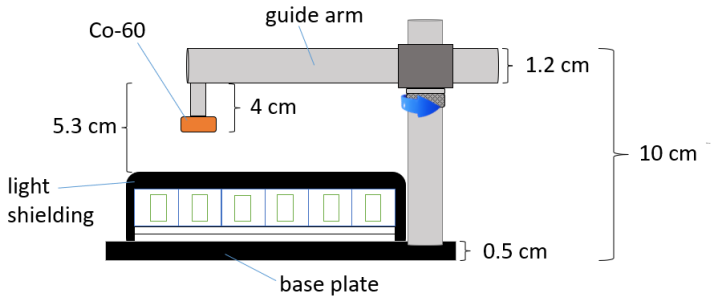

(b) side view

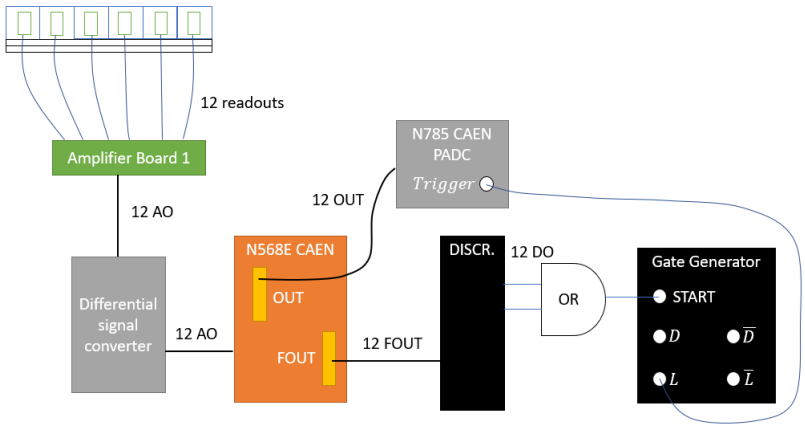

(c) scheme of the PADC measurement

Figure 61: ADC measurement with module 1 in presence of a Co-60 source.
At each run, the Co-60 source was positioned with the guide arm above one of the measuring positions 1-5.
For simplicity, the light shielding and the guide arm with source were omitted in figure 61c.

Figures 62a - 62e show the amplitude histograms obtained with module 1 in the previously defined positions 1-5.

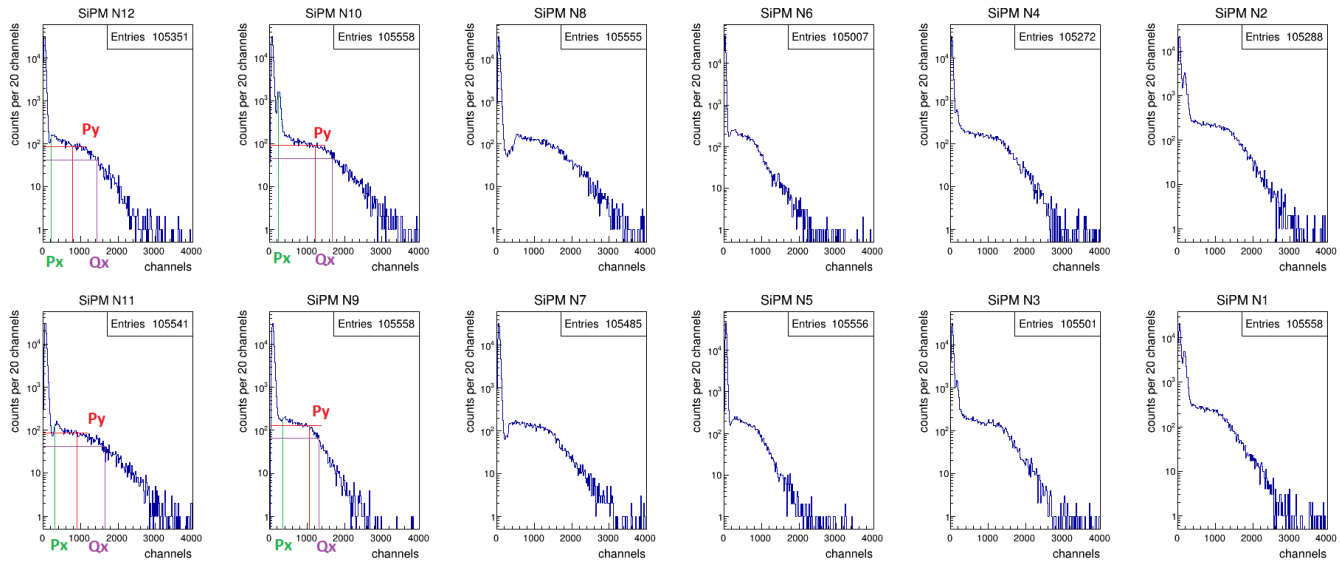

(a) position 1

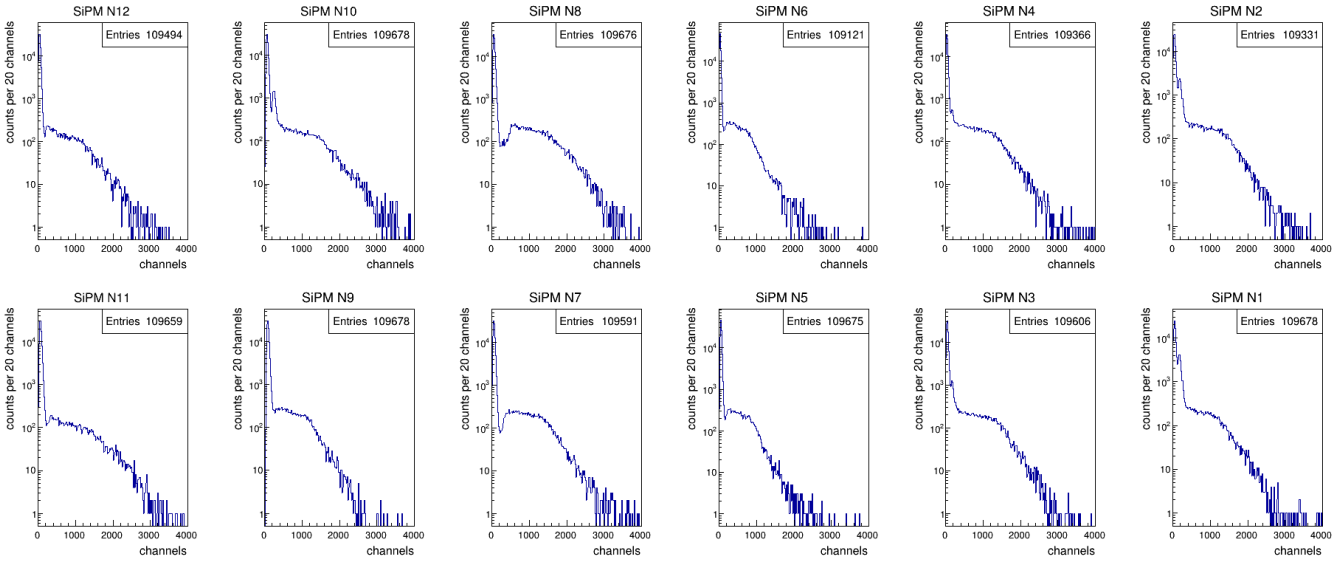

(b) position 2

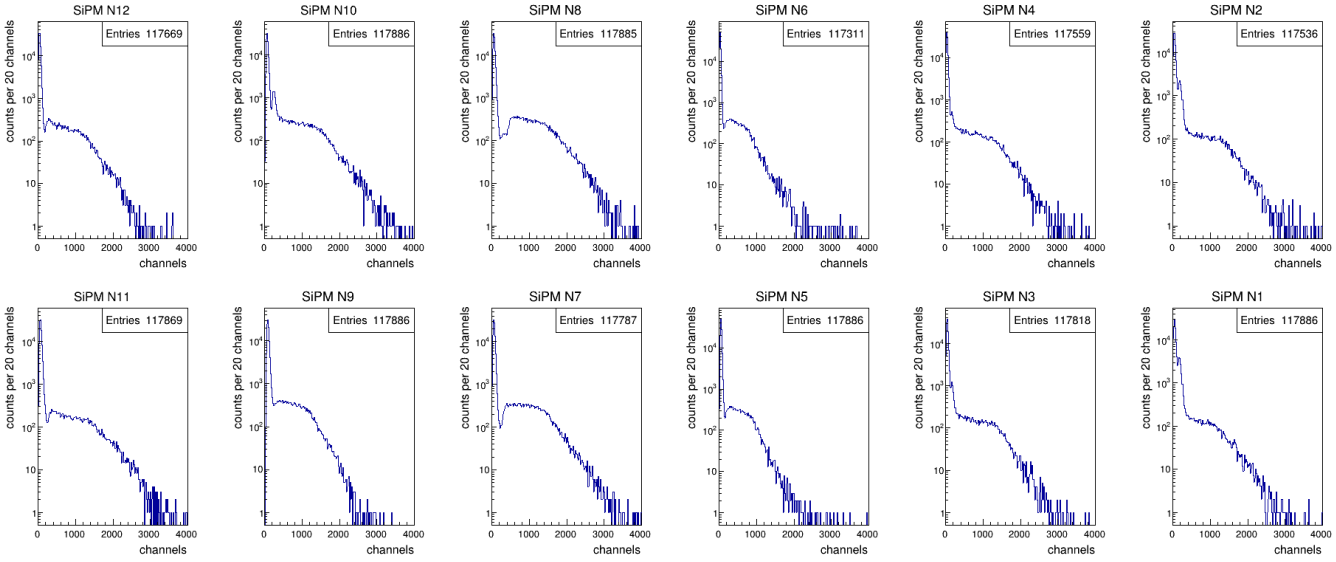

(c) position 3

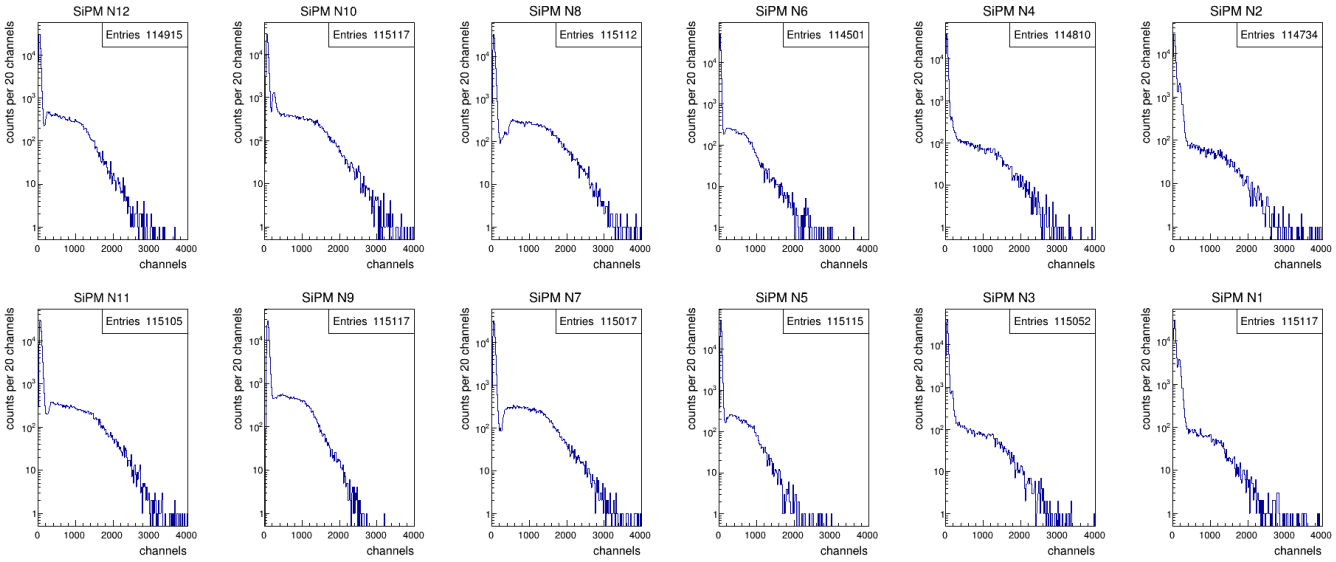

(d) position 4

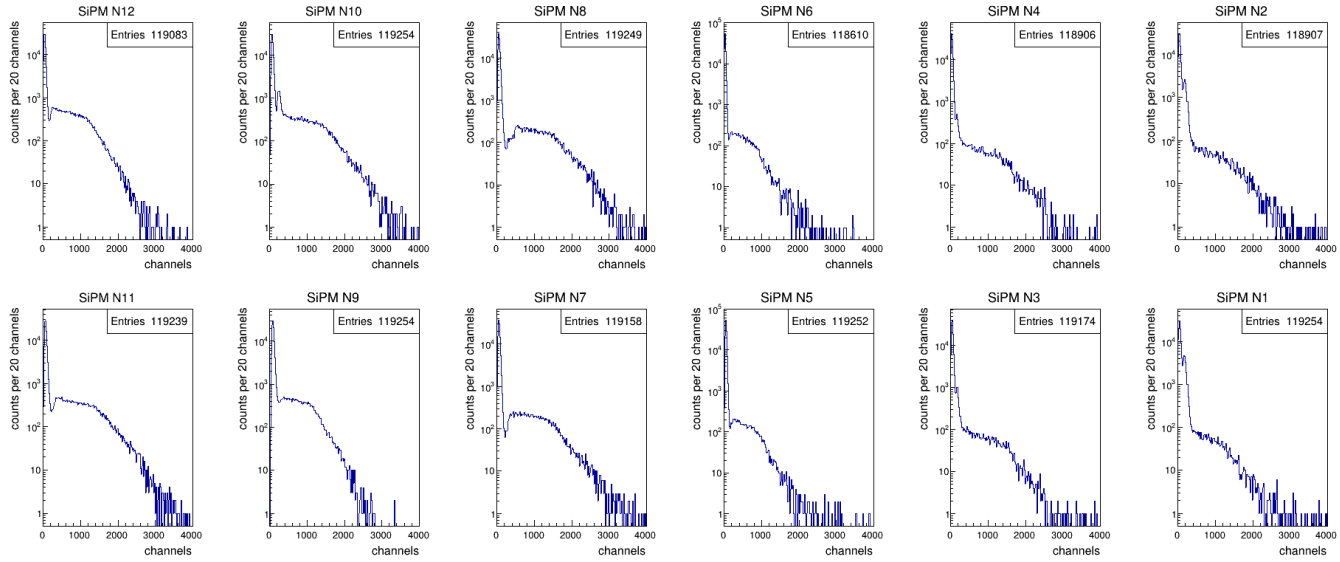

(e) position 5

Figure 62: amplitude histograms of all 5 measurement positions obtained from all 12 readouts respectively. The full voltage range of each histogram ($\approx$ 4000 channels) was divided in 200 bins. x-axis: amplitudes expressed in channel ($\frac{full\ voltage\ scale}{enabled\ channels\ by\ 12\ bit} \approx 1$ mV $= 1$ channel), y-axis: corresponding counts

To understand the full spectrum of a readout, it is helpful to imagine it as a superposition of 2 spectra: the background spectrum and the so called 'single detector spectrum', which we will both now define.

Looking at the PADC spectra of an individual readout, we notice a high, narrow peak at the lower end of the amplitude axis. It arises due to the OR's we used in the construction of the gate signal and it belongs to what we call the 'background spectrum' in the following. The counts that make it up were namely recorded because the discriminator threshold of another readout was exceeded.
Due to the absence of a particle in the considered detector, low amplitude values (background events) are then recorded, motivating the spectrums' name.
The range of this background spectrum spans from 0 mV to the discriminator threshold ('Px').

The 'single detector spectrum' corresponds to the spectrum obtained from a situation, where we only deal with one plastic scintillator detector with its 2 readouts (instead of 6 plastic scintillators and 12 readouts in total). Note that the trigger threshold of the 'single detector spectrum' is imposed on one readout only, giving a spectrum that looks roughly like the SiPM 6 spectrum in figure 33a.
From this 'single detector spectrum' only the part above the fixed discriminator threshold makes it into the resulting spectrum of this experiment, while the part of the 'single detector spectrum' below it is cut off.[13]
The contributing part thus includes all events that indicate energy deposition of cosmics in the detector and thus have lead to a record of measuring points at all readouts.

So to sum this up briefly: within the interval (Px, 0 mV], the resulting spectrum of a readout consists of the background spectrum. Above 'Px', the resulting spectrum of a readout consists of the 'single detector spectrum' belonging to this readout. From this 'single detector spectrum', however, only the part above 'Px' contributes (as we described above).

Depending on the fixed discriminator threshold and therefore the position where the 'single detector spectrum' is cut, the resulting spectrum can look like the SiPM N8 histograms (for high discriminator thresholds), like the SiPM N10 histograms (for low discriminator thresholds) or an in-between spectrum like the SiPM N9 histograms.

[13] Strictly speaking, it's the part greater than or equal to the tuned discriminator threshold, that enters in the resulting spectrum.

We denote the channel number at which these 2 spectra encounter as 'Px', which makes it a measure for the adjusted discriminator threshold (as we have already anticipated above). Since we didn't strive to adjust all of the discriminator thresholds to the precise same value, we do not expect them all to have the same 'Px'-value.

From the wide hump located to the right of the 'Px' value, other important parameters such as its height ('Py') and the number of channels at half height ('Qx') can be read off.[14]
Basically, we assume the 'Py' value of a certain readout to be higher in positions, where the distance to the source is smaller. This is based on our expectation that high-amplitude signals are measured more frequently, if the source is closer to the respective detector.
It may be difficult to read the exact height differences between the readouts in figures 62a - 62e with the eyes only, because the y-axis is logarithmically scaled. But at least one can perceive them qualitatively without problems.

The channel number at half height of the hump, 'Qx', has an analogous meaning for the ADC measurement as the quantity 'cahh' for the TDC measurements: it serves as a parameter to compare the gain among the SiPMs. Ideally, we wish all SiPMs to have equal gain, but this is clearly not the case since the count number of SiPM N5 and SiPM N6 has dropped to 0 way earlier than most of the other readouts.

For a better analysis, the SiPMs of module 1 were assigned their values for 'Px', 'Py' and 'Qx' in table 32 for all 5 measurement positions. To determine these quantities, their reading positions were first roughly located in the plot and then the exact values were extracted from the corresponding histogram table. This slightly different evaluation approach was chosen to avoid reading errors on the logarithmic scaled axis.

[14] The graphical determination of the Px, Py and Qx values is explicitly shown for 4 histograms in figure 62a to provide clarity.

SiPM name	position 1	position 2	position 3	position 4	position 5
N1	Px=170 Py=228 Qx=1390	Px=170 Py=185 Qx=1430	Px=170 Py=105 Qx=1410	Px=170 Py=67 Qx=1370	Px=170 Py=58 Qx=1370
N2	Px=190 Py=219 Qx=1570	Px=190 Py=182 Qx=1570	Px=190 Py=111 Qx=1550	Px=190 Py=64 Qx=1590	Px=190 Py=58 Qx=1590
N3	Px=170 Py=148 Qx=1550	Px=170 Py=200 Qx=1570	Px=170 Py=141 Qx=1550	Px=170 Py=86 Qx=1510	Px=170 Py=71 Qx=1570
N4	Px=170 Py=143 Qx=1530	Px=170 Py=206 Qx=1470	Px=170 Py=142 Qx=1530	Px=170 Py=76 Qx=1550	Px=170 Py=60 Qx=1530
N5	Px=210 Py=172 Qx=970	Px=210 Py=252 Qx=970	Px=230 Py=290 Qx=930	Px=250 Py=207 Qx=950	Px=250 Py=157 Qx=970
N6	Px=190 Py=179 Qx=870	Px=190 Py=253 Qx=890	Px=210 Py=280 Qx=930	Px=210 Py=204 Qx=830	Px=210 Py=148 Qx=910
N7	Px=310 Py=122 Qx=1610	Px=330 Py=188 Qx=1630	Px=350 Py=285 Qx=1590	Px=330 Py=286 Qx=1590	Px=350 Py=195 Qx=1630
N8	Px=470 Py=128 Qx=1670	Px=490 Py=184 Qx=1670	Px=490 Py=294 Qx=1670	Px=510 Py=281 Qx=1670	Px=510 Py=192 Qx=1670
N9	Px=330 Py=118 Qx=1330	Px=290 Py=185 Qx=1330	Px=330 Py=301 Qx=1290	Px=290 Py=447 Qx=1290	Px=330 Py=380 Qx=1310
N10	Px=250 Py=90 Qx=1670	Px=250 Py=171 Qx=1630	Px=230 Py=259 Qx=1610	Px=250 Py=379 Qx=1570	Px=250 Py=315 Qx=1650
N11	Px=290 Py=83 Qx=1690	Px=330 Py=104 Qx=1650	Px=350 Py=159 Qx=1610	Px=330 Py=275 Qx=1670	Px=330 Py=388 Qx=1630
N12	Px=230 Py=85 Qx=1410	Px=230 Py=115 Qx=1350	Px=270 Py=168 Qx=1430	Px=250 Py=297 Qx=1370	Px=250 Py=391 Qx=1350

Table 32: PADC measurement for module 1: values for Px, Py and Qx determined from the histogram plots and files. The values given have the following uncertainties:
ΔPx=40 channels, ΔPy=40 counts and ΔQx=60 channels.

Before we discuss the values from table 32, we point out that it is by no means free of uncertainties. Despite the use of histogram files, the choice of the number of bins for a given number of counts ('binning') can strongly influence the reliability of the read values.
For the binning, we have chosen 200 bins for 105 000-120 000 counts. This causes that we have smaller fluctuations around the wide hump ('Py') than at half the height of 'Py'.
As a result, the relative uncertainty of 'Qx' is higher than of 'Py' or 'Px'.

Table 32 shows that most of the SiPMs have a gain corresponding to a 'Qx'-value of 1500 to 1700 channels. Taking this as a referance range, SiPM N1, N9 and N12 have a 'small' gain deficit that is equivalent to 200-300 channels. Although this deviation might not be obvious at first glance, it can be observed in figures 62a - 62e as well, when we have a closer look.
In contrast, the way too small gain of SiPM N5 and N6 is immediately noticeable by their early falling slope (see figures 62a - 62e). Accordingly, the gap between the 'Qx'-values of SiPM N5 & N6 and the referance range is huge.

Theoretically, there should be a proportional connection of adjusted discriminator to the 'Px'-values: the higher the set discriminator threshold the higher the 'Px'-values. Comparing the 'Px'-values to the set discriminator thresholds from table 32, we do not always get a consistent relationship.
For example, SiPM N9 has a lower discriminator threshold than SiPM N10, but its 'Px' value is higher than the one of SiPM N10. These two SiPMs also do not fit our expectations when it comes to gain, since SiPM 9 has a larger dark current but a lower 'Qx' value.
Using cross-checks with the performed TDC-measurements, we were able to rule out possible error sources such as problems with the SiPM itself or the amplifier board.
Eventually, the error was a low gain of the shaping amplifier channel connected to SiPM N9.

Finally, we would like to mention that the total number of counts shown in each histogram (denoted as 'Entries' in the legends) should be the same when they were recorded during the same measurement run, i.e. in the same measurement position. This necessary condition arises due to the OR-logics involved in the creation of the 'time window'. It turns out that this condition is almost fulfilled and that the main reason for deviations is that we refused to show and count events with an amplitude of 0 mV.

The 'Py'-values from table 32 are largely in agreement with our predictions mentioned earlier.
An exception are the values for SiPM N5 and N6 in positions 1 and 2, where they exceed the 'Py' value of SiPM N3 and N4. This can however be explained by the way too low gain which makes the histograms narrower and thus higher (as mentioned earlier).

In terms of knowledge acquisition, the TDC measurement of one module does not differ much from the plastic scintillator measurements, we did in chapter 6. According to the detector response, we gain a rough information about the position of an incident particle at a certain point in time.
After a voltage-energy calibration, one would be also capable to tell the deposited energy in the detector due to the linearity between ToT, amplitude and deposited energy.
However the resolution of a charged particles' trajectory is low, i.e. a volume including all its possible paths is quite large and a great variety of angles of incidence are possible.

Since 2 cosmic events are mostly well separated in time, we can tremendously constrain the amount of possible trajectories, if we add additional detector layers. The reason for this is that we assume that cosmics propagate to good approximation in straight lines and with multiple position informations at later or earlier times, we can interpolate and extrapolate the covered path.

For the following experiment, module 2 was put on top of module 1, such that the scintillator bars were aligned in the same direction ('parallel run'). The aim was to measure the ToT of all 24 detectors using the coincidence signal of a test detector to govern the measurement.
In the same way as before, this signal serves as ingredient for defining a gate, i.e. as a limiter of measuring time span. The test detector from the single-module runs was placed on top of module 2, whereby we intended to center it with referance to the modules below.

The adjusted dark currents of all SiPMs involved as well as their discriminator threshold settings are listed in table 33. If we compare the settings from the single-module runs (see table 28) with those from table 33, we see that the dark currents of module 1 and all thresholds were left the same.
The dark currents of the test detectors and some module 2 detectors, however, have been reduced.

module 1			module 2		
SiPM name	dark current (μA)	threshold (1)	SiPM name	dark current (μA)	threshold (1)
N1	3.27 // 3.32	2500	N13	2.27 // 2.29	3100
N2	2.65 // 2.67	2500	N14	2.48 // 2.47	2900
N3	2.42 // 2.47	2500	N17	2.00 // 2.00	2500
N4	2.40 // 2.49	2500	N18	1.89 // 1.89	2500
N5	1.96 // 1.98	2500	M5	4.78 // 4.78	2500
N6	1.98 // 2.00	2500	M6	5.87 // 5.76	2500
N7	2.49 // 2.52	2500	N19	2.10 // 2.11	2500
N8	2.69 // 2.67	2500	N20	1.89 // 1.90	2500
N9	3.01 // 3.05	2500	N21	2.01 // 2.05	2500
N10	2.55 // 2.60	2500	N24	2.28 // 2.29	2500
N11	2.77 // 2.89	2500	N23	2.12 // 2.15	2500
N12	3.24 // 3.34	2500	N22	2.28 // 2.23	2500
test detector T1	7.42 // 7.36	-105.1 mV	test detector T2	7.42 // 7.44	-105.1 mV

Table 33: collection of all adjusted dark currents used in the parallel run
Notice that the left value for the dark current was measured before the start of the measurement and the right value was measured after the measurement was stopped.

In figure 63, we present the top module histograms of the parallel measurement and in figure 64, the histograms of the bottom module are depicted.

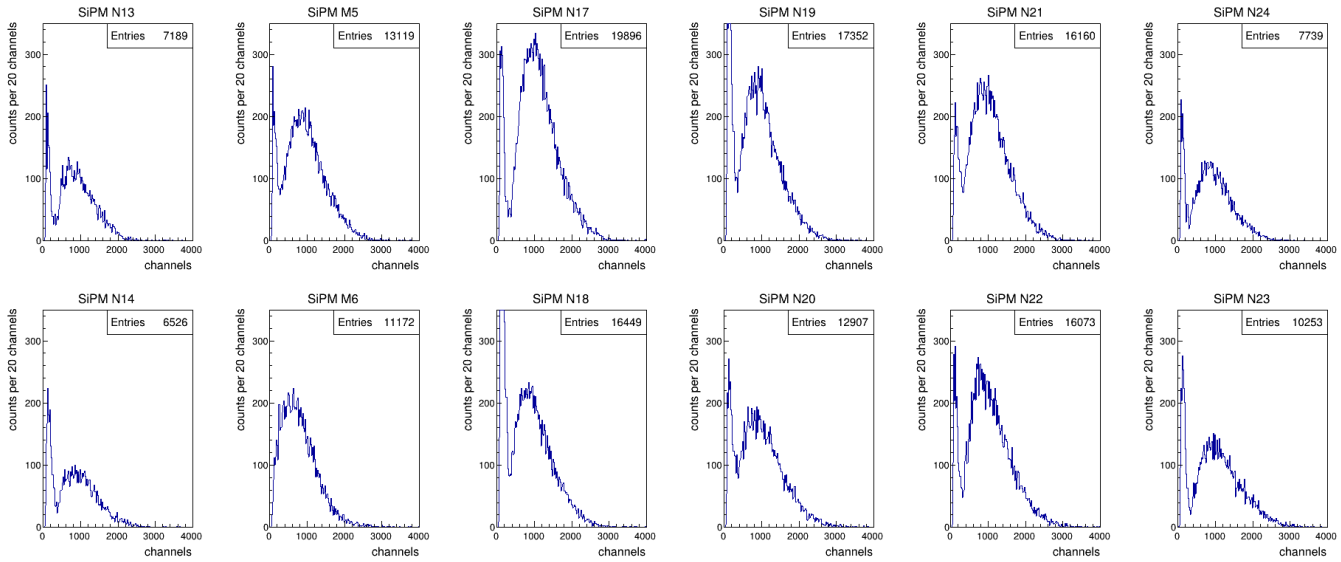

Figure 63: parallel measurement: histograms for readout signals on module 2.
The histograms are arranged in consistency to the position of the readouts on module 2.
The full ToT range of each histogram ($\approx$ 4000 channels) was divided in 200 bins.
x-axis: ToT expressed in channels (100 ps = 1 channel), y-axis: corresponding counts

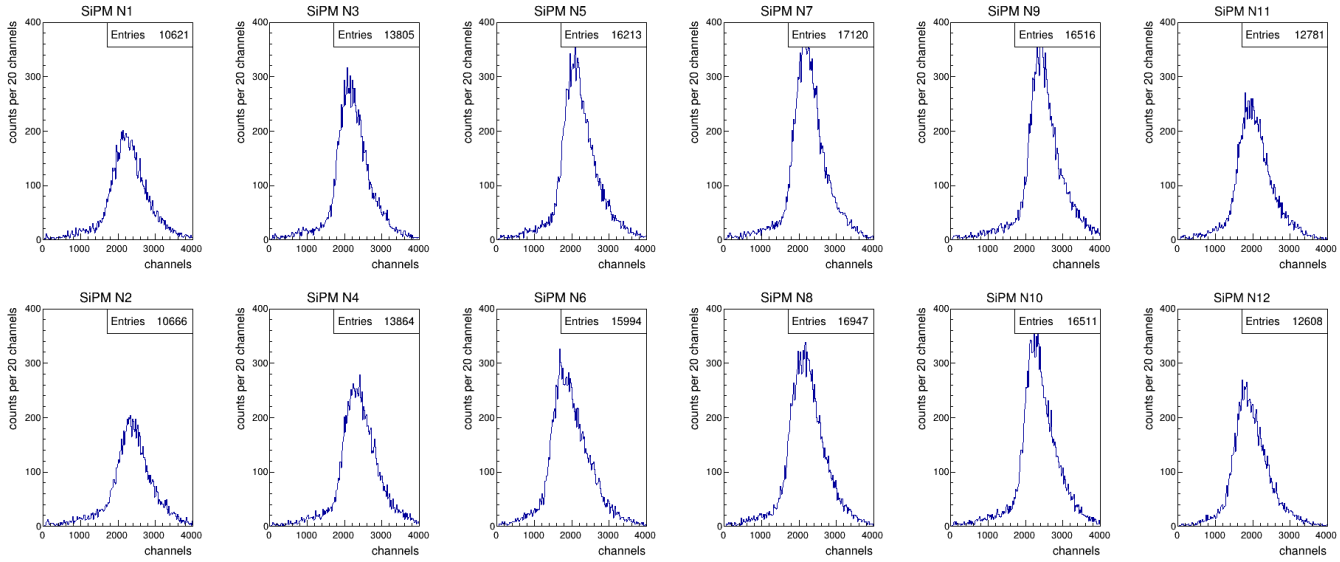

Figure 64: parallel measurement: histograms for readout signals on module 1.
The histograms are arranged in consistency to the position of the readouts on module 1.
The full ToT range of each histogram ($\approx$ 4000 channels) was divided in 200 bins.
x-axis: ToT expressed in channels (100 ps = 1 channel), y-axis: corresponding counts

Analogous to the TDC measurements with single modules, the 'cahh' values of all readouts were determined graphically from figures 63, 64 and subsequently listed in a table (see table 34).

module 1		module 2	
SiPM name	cahh ± 300 (channels)	SiPM name	cahh ± 300 (channels)
N1	2700	N13	1300
N2	2800	N14	1450
N3	2600	M5	1400
N4	2750	M6	1250
N5	2500	N17	1550
N6	2300	N18	1450
N7	2550	N19	1400
N8	2550	N20	1500
N9	2750	N21	1550
N10	2650	N22	1500
N11	2400	N24	1400
N12	2400	N23	1550

Table 34: TDC measurement parallel runs: we list for all readouts the number of channels corresponding to half the height of the histogram peak ('cahh').
Keep in mind that the unit 'channel' represents a time span of 100 ps.
The provided uncertainty covers reading errors made in the graphical evaluation and the error due to the chosen binning.

When we compare the 'cahh' values of module 2 obtained from the single-module run and the parallel runs (see table 29 and 34), we observe changes that are consistent with our anticipations.
For example, a decrease in dark current results in a drop of the 'cahh' value, as we mentioned in the discussion of the single-module runs. Furthermore, for SiPMs with approximately unaltered dark current, the 'cahh' value changed as predicted little to not at all.[15]
Also for SiPM M5, whose dark current was the only one increased, a consistent result was obtained with a 'slight' increase of the 'cahh' value.

[15] in the range of our uncertainty

Concerning the gain of module 1, we note that the 'cahh' values have remained the same within the range of uncertainty (see table 29 and 34). This has been expected, since there is little difference in the dark currents of the SiPMs from module 1.

For correct predictions of this type of experiment, it is important to consider 2 things: the kinetic energy of our particles (i.e. cosmic muons) and the detector size. In our case, the used detector is small enough and the cosmics high-energetic enough, that they do not come to halt in the detector.
Even more: despite loosing energy throughout the penetration, the cosmics are still in an energy range, where $\frac{dE}{dx} = 2.0$ MeV/cm $=$ const. holds.
Consequently, we expect that the energy deposition in a detector again depends only on the distance traveled. If we would use particles with lower energy instead such as electrons from Co-60 decay channels, the results would look different, because the most of them wouldn't make it even in the bottom module.

Reducing the dark currents at module 2 while keeping the same thresholds leads to the formation of a second sharp histogram peak for each of its readouts (except SiPM M6).
This peak at the lower ToT end includes beside background events also 'real' events with low amplitudes and therefore short ToTs.
This complicates a separation of background events and real events, which is unfavorable.
So we can conclude for module 2 that this choice of dark current is generally too low, but it's especially low for SiPM M5 and M6.
For SiPM M5, this shows in form of a high 2nd peak and a low 'cahh' value according to table 34.[16]
Even more severe consequences of a low gain can be observed at SiPM M6, where it appears as if a considerable part of the 'real' events was ruled out, since their signals didn't cross the threshold at all. This extreme case is also clearly visible from the corresponding 'cahh' value in table 34.

Opposed to that the histograms of module 1 still look gaussian. Looking at the histograms of module 1, we recognize that the channel count associated with the histogram peak is for each readout at least roughly the same as in the single-module run.
Deviations might be explained when we consider trajectories passing through module 1 in the current setup. In contrast to the single-module run, the trigger detector and module 1 are now kept at a distance by module 2, which is placed in between them.
As a consequence, the range of angles of incidence that lead to an event record has changed for each detector. But from earlier discussions, we know that this comes with changes in the energy deposited.

Due to the different measurement times, significantly more counts were recorded in the single-module run, but comparing the counts at the histogram peak for the same SiPMs shows that they are about proportional. The latter two observations suggest that the trigger detector lies similarly above module 1 as before, meaning that the horizontal alignment of them is similar as before.

Subsequently to the parallel run, we rotated module 2 and the test detector 90° clockwise around an axis perpendicular to module 1 and restarted the measurement. For later referance and comparison to the parallel run, we will denote this run as 'lattice run'. The motivation for this name comes from the pattern formed by the scintillators of both modules resembling of a lattice.
The lattice pattern will not only give the run its name, but will enable to address some events a unique lattice element ('pixel').

This setup already allows to exclude many trajectories that were imaginable in the single layer runs and thus the resolution grows.
Although we wish to interpret the pixel as a trustworthy measure to indicate the trajectory of the associated particle, one must not overestimate the accuracy of this quantity if only 2 module layers are used. For example, if we find a unique pixel to an incident particle, we mustn't fall the temptation to assume that this particle must have traveled through the intersection area of the two scintillators.

[16] although SiPM N13 and N14 have similar 'cahh' values, we must take into account that there is a higher threshold set for them!

In fact, in the case of only 2 detector layers and fixed pixel, the geometry allows numerous trajectories to pass by the intersection surface obliquely but without crossing it.
However, when using 3 or more detector layers, these oblique trajectories can be significantly reduced and the informative value of a pixel increases.

For the lattice run, the dark currents and thresholds of the readouts were collected in table 35.
In response to the too low gain of the module 2 readouts in the previous measurement, we increased their dark currents considerably.
In addition, the thresholds of SiPM N13 and N14 were lowered from 3100 respectively 2900 to 2500.
Opposed to that the thresholds and dark currents of the module 1 readouts were left essentially as in the previous measurements.

module 1			module 2		
SiPM name	dark current (μA)	threshold (1)	SiPM name	dark current (μA)	threshold (1)
N1	3.29	2500	N13	6.17	2500
N2	2.67	2500	N14	6.62	2500
N3	2.46	2500	N17	3.54	2500
N4	2.42	2500	N18	3.34	2500
N5	1.98	2500	M5	10.98	2500
N6	2.04	2500	M6	12.24	2500
N7	2.52	2500	N19	3.83	2500
N8	2.67	2500	N20	3.23	2500
N9	2.99	2500	N21	4.19	2500
N10	2.59	2500	N24	4.14	2500
N11	2.83	2500	N23	4.90	2500
N12	3.25	2500	N22	3.80	2500
test detector T1	8.62	-105.1 mV	test detector T2	8.38	-105.1 mV

Table 35: collection of all adjusted dark currents and thresholds used in the lattice run

The histograms of this measurement for the upper module are shown in figure 65 and those of the bottom module are presented in figure 66.

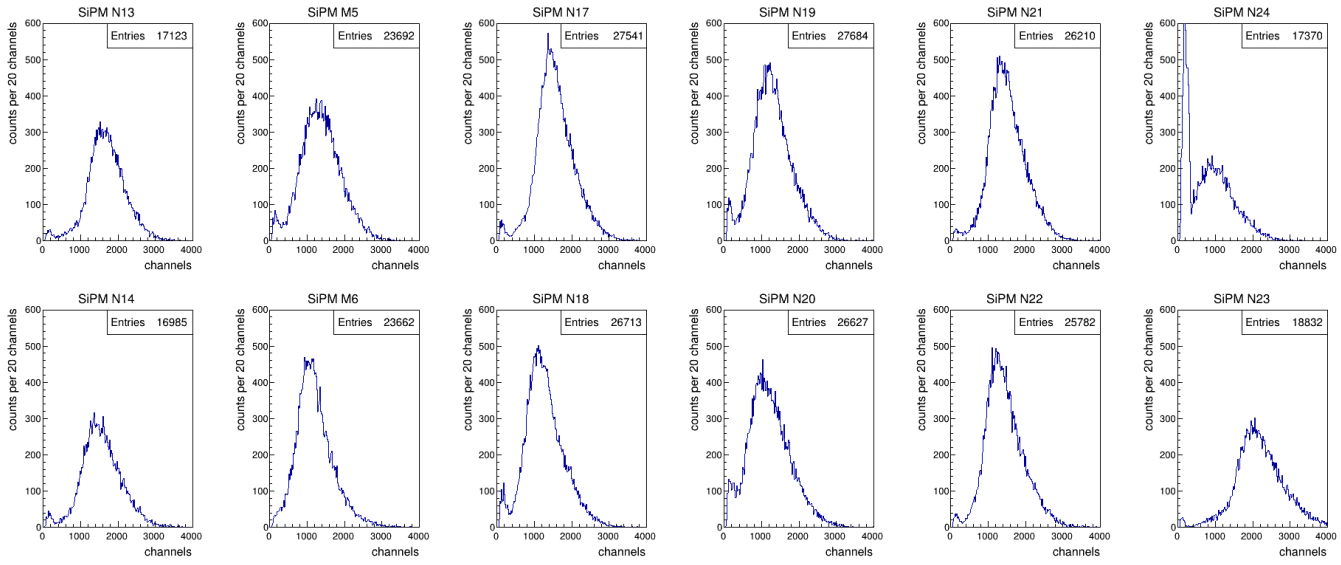

Figure 65: lattice measurement: histograms for readout signals on module 2.
The histograms are arranged in consistency to the position of the readouts on module 2.
The full ToT range of each histogram ($\approx$ 4000 channels) was divided in 200 bins.
x-axis: ToT expressed in channels (100 ps = 1 channel), y-axis: corresponding counts

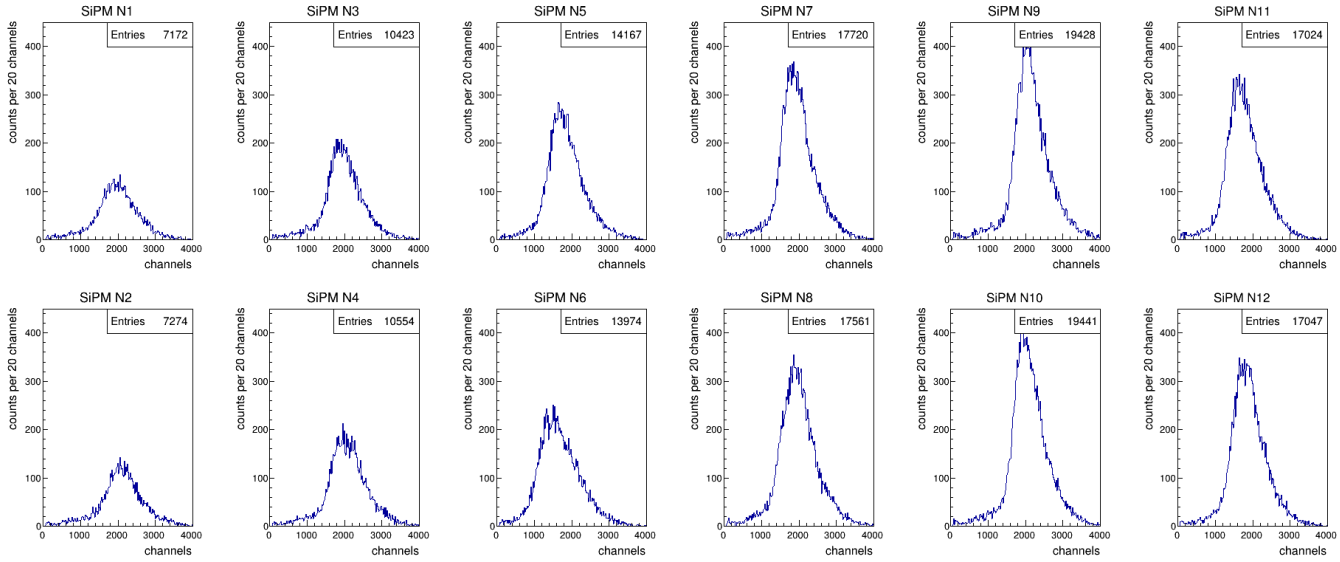

Figure 66: lattice measurement: histograms for readouts on module 1.
The histograms are arranged in consistency to the position of the readouts on module 1.
The full ToT range of each histogram ($\approx$ 4000 channels) was divided in 200 bins.
x-axis: ToT expressed in channels (100 ps = 1 channel), y-axis: corresponding counts

In table 36, all cahh values of module 1 and 2 taken in the lattice measurement are included.

module 1		module 2	
SiPM name	cahh ± 300 (channels)	SiPM name	cahh ± 300 (channels)
N1	2500	N13	2100
N2	2600	N14	2050
N3	2450	M5	1950
N4	2600	M6	1550
N5	2250	N17	1900
N6	2050	N18	1700
N7	2250	N19	1700
N8	2350	N20	1600
N9	2550	N21	1950
N10	2450	N22	1950
N11	2200	N24	1450
N12	2350	N23	2750

Table 36: TDC measurement lattice run: we list for all readouts the number of channels corresponding to half the height of the histogram peak ('cahh').
Keep in mind that the unit 'channel' represents a time span of 100 ps.
The provided uncertainty covers reading errors made in the graphical evaluation and the error due to the chosen binning.

The combination of a small data set (i.e. $<$ 50 000 counts) and same total bin number as in the solo module runs, causes rough steps and irregularities at the falling edge of the histograms.
We take this into account in the same way as we did in the parallel module run: by adding additional 100 channels to the uncertainty, we used in the solo module runs.
The 'cahh' values of module 1 are expected to be the same as in the previous measurements, since the same dark current and threshold settings are used as before.
Comparing the tables 29, 34 and 36, we find that this prediction holds within our range of uncertainty.

On the other hand, we find that the 'cahh' values of module 2 have strongly increased compared to the previous measurement. This, however, comes with no surprise, because as mentioned earlier this is how an increase of dark current acts out on the 'cahh' value.

Comparing the tables of the module 2 solo run with table 36, the changes in 'cahh' values are in line with our expectations: SiPMs whose dark current has been increased (SiPMs N13, N14, M5, M6, N23, N24) now have a higher 'cahh' value.
At the same time, SiPMs whose dark current has been left almost unchanged (SiPMs N17, N18, N19, N20, N21, N22), have a 'cahh' value that has remained the same within the uncertainty.

However, there are 2 deviations that should be noted: firstly SiPM N22 differs by 350 channels despite having nearly the same dark currents.
Second, the 'cahh' value of SiPM N24 has decreased by 150 channels, although the dark current of SiPM N24 has been increased compared to the single-module run.
After several tests, it was found that the reason for this was the weak amplification of board channel 10 on amplifier board 2.1. This makes perfect sense considering that board channel 10 amplified SiPM N22 in the single module run and SiPM N24 in the lattice run.
At this point, it should also be noted that in the single module run, the amplifying board channels of SiPM N17 and M5 were interchanged as well as those of SiPM N18 and M6.

Apart from the small 'cahh' value, the weak amplification of board channel 10 is directly observable in form of a second peak in the SiPM N24 histogram.
For any other SiPM of module 2, the increase of dark current has lead to a tremendous decrease of the second peak at the lower ToT end (compare with figure 63).
From this we conclude: the signals have become larger and have moved to the right in the histogram. For the events from the peak at the lower ToT end, this means that they have moved into the real event peak.
With the choice of dark current and threshold according to table 35, we have finally achieved a satisfactory separation of real events and noise for both modules. Only for SiPM N20, the dark current could be increased slightly, because it seems as if a small part of the signals is cut away.

In figure 66, we see that both, the total counts as well as the histogram maximum of SiPM N9 and N10 are larger than of the detectors in the module center (SiPM N7 and SiPM N8).
However, according to the explanations from the single-module run, we expect that the maximum from the near-center SiPMs should be larger and their total counts as well.
Instead their values are roughly as high as of the detectors on the right edge.

The analysis at the end of the experiment showed that there were deviations in the alignment of the trigger detector and module 1. The light shielding of the modules and of the trigger detector, created by wrapping them in black cloth and black tape, obscured the exact position of the detector edges and significantly affected accurate alignment with each other.
It was found that the trigger detector and module 2 were not exactly above module 1, but that they extended beyond the right side of module 1.

In this configuration, SiPM N9 and N10 are now centered below the test detector and SiPM N7 and N8 are more decentralized. As a consequence, the previously described situation of measurable trajectories[17] shifts to the right with corresponding consequences for all SiPMs of module 1.
SiPM N9 and N10 should thus have both, the most counts and the highest histogram peak. As you now move away from SiPM N9 and N10, the total number of counts and histogram peaks should decrease. This fits very well with our measurement and also explains why SiPM N7 and N8 have similar histograms as SiPM N11 and N12.

After all these successful Prototype 2 experiments, it was planned to continue with more advanced investigations on the setup used in the lattice-run. For example, it was intended to aim with a focussed particle beam on certain pixels of the Prototype 2 detector and test the resolution in x- and y- direction. Unfortunately, we didn't have access to such a test beam within the time available for this thesis. Therefore we couldn't perform these tests such that they have been postponed to future papers.

[17] trajectories fulfilling the trigger condition according to the previous TDC experiment

9 Conclusion and final remarks

The main goals of this thesis were the construction of the Prototype 1 & 2 detectors and tests on their functionality and accuracy.
A very important success of the Prototype 1 experiments is the experimental proof that particles can be reliably detected using liquid scintillator EJ-309 and WLSFs.
An even more valuable insight is that the WLSFs in combination with the liquid scintillator enabled to readout a quite large volume ($506 \times 40.1 \times 60.1\ mm^3$) with only 2 SiPMs. It was clear per design that the amount of photons generated in the liquid scintillator and collected by the WLSFs would be less than for the plastic scintillator. This was indeed observed in the tests conducted.
Nevertheless, the collected light is according to our tests more than enough to detect MIPs with almost 100% efficiency. Thus the use of liquid scintillator and WLSFs may serve as a reasonable alternative in large detectors or detectors with elaborate geometries where plastic scintillators might not fill out the whole detector volume.

Unfortunately, the timing of the Prototype 1 detector turned out to be not as good as we had hoped.[18]
We tried to figure out the reason for the bad timing by illuminating a Wavelength Shifting Fibre in the center with a blue LED, while reading out with 2 SiPMs at the WLSF ends.
The quantities of main interest were the amplitudes and the delays of the triggering signal (the pulse generator signal supplying the LED) to the respective signals of the 2 SiPMs.
Although, the measurement was repeated and optimized several times, the delays didn't give explainable values and moreover they were non-reproducible. From this we draw the conclusion that scattering within one WLSF fibre can take on a great variety of angles and thus also of pathlengths.
Furthermore it seems as if the behaviour of one WLSF only is volatile, but the behaviour of a collection of WLSF (16 in our case) is reproducible. Thus future attempts to predict the timing behaviour may be better conducted with more than 1 WLSFs.

As a major success, we could also show that our Prototype 1 detector detects with a high efficiency of greater or equal to 98%, which is comparable with a plastic scintillator detector.

Moreover, we were able to apply a fast and simple method for an (at least rough) energy calibration of a plastic scintillator detector and verify the results with a well-known Compton edge. This method might serve in the future as an alternative to a time-consuming Monte Carlo simulation, when a rough relation between energy and amplitude satisfies or a short check of such a simulation is needed.

For the purpose of Prototype 2 measurements, we have established a data acquisition system using a CAEN PADC as well as TDC that was implemented in appropriate circuits. Together with the ROOT system used for data storage and processing, standard investigations (binwidth settings, statistics, fits,...) as well as deeper analyses are possible.
Among the latter, we want to mention explicitly the possibility to show all events, that obey certain restrictions. Such restrictions can be e.g. being above a chooseable threshold or fulfilling a certain AND condition (like show all events of SiPM N1, where SiPM N1 & N2 have both non-zero entries).
Similar analyses have been performed for the lattice measurement for example and yielded consistent results, but they were omitted since this would go beyond the scope of this thesis.

Finally we succeeded in finding the form and relevant parameters to describe the ADC and TDC histograms. We set the parameters in context to gain, threshold etc. and proved our correct understanding of them.

[18] With 'timing', we mean the difference between dt@lv(signal created at the detector center, SiPM 7) and dt@lv(signal created at the detector center, SiPM 6). Ideally it would be 0 ns, but instead it amounts to approximately 2 ns. This is a large deviation considering that light travels 40 cm within this time.

References

[1] 2020. URL: https://easyelectronicsproject.com/testing-components/capacitor-code/.

[2] URL: https://www.apogeeinstruments.com/differential-vs-single-ended-measurements/.

[3] URL: https://de.wikipedia.org/wiki/Avalanche-Photodiode.

[4] URL: https://teledynelecroy.com/doc/tutorial-special-trigger-modes.

[5] URL: https://de.wikipedia.org/wiki/Datei:Cobalt-60_Decay_Scheme.svg.

[6] URL: https://www.nature.com/articles/s41598-020-75310-3/figures/6.

[7] URL: https://wanda.fiu.edu/boeglinw/courses/Modern_lab_manual3/beta_spectroscopy.html.

[8] URL: https://de.wikipedia.org/wiki/Compton-Effekt.

[9] Claude Amsler. "Nucleon-antinucleon annihilation at LEAR". In: *arXiv preprint arXiv:1908.08455* (2019).

[10] CAEN. *N568E 16 Channel Spectroscopy Amplifier*. 2018. URL: https://de.scribd.com/document/401297944/N568E-rev9.

[11] *CAEN Educational Handbook - Nuclear and Particle Physics Experiments*. 2018. URL: https://www.caen.it/educational-handbook-2018/.

[12] C Curceanu et al. "Fundamental physics at the strangeness frontier at DAΦNE. Outline of a proposal for future measurements". In: *arXiv preprint arXiv:2104.06076* (2021).

[13] Lukas Gruber. "Studies of SiPM photosensors for time-of-flight detectors within PANDA at FAIR". PhD thesis. 2014.

[14] William R Leo. *Techniques for nuclear and particle physics experiments: a how-to approach*. Springer Science & Business Media, 2012.

[15] M.Cargnelli. *Private communication*.